Quantitative Study of Membrane Nano-organization by Single Nanoparticle Imaging

Chao Yu

NNT :2019SACLX054

Quantitative Study of Membrane Nano-organization by Single Nanoparticle Imaging

Thèse de doctorat de l'Université Paris-Saclay
préparée à l'École polytechnique

École doctorale n°573 interfaces : approches interdisciplinaires, fondements, applications et innovation (Interfaces)

Spécialité de doctorat: Biologie

Thèse présentée et soutenue à Palaiseau, le 24 Juillet 2019, par

Chao YU

Composition du Jury :

M. François TREUSSART Professeur, Paris VI	Président
M. Benoît LADOUX Professeur, Institut Jacques-Monod	Rapporteur
Mme Cecile SYKES Directrice de recherche, Institut Curie	Rapportrice
M. François TREUSSART Professeur, Paris VI	Examinateur
M. Daniel GILLET Directeur de recherche, CEA	Examinateur
M. Cédric BOUZIGUES Maître de conférences, Ecole polytechnique	Directeur de thèse
Mme Antigoni ALEXANDROU Directeur de recherche, CNRS	Co-Directrice de thèse

Thèse de doctorat

Université Paris-Saclay
Espace Technologique / Immeuble Discovery
Route de l'Orme aux Merisiers RD 128 / 91190 Saint-Aubin, France

LABORATOIRE D'OPTIQUE ET BIOSCIENCES
Ecole Polytechnique, CNRS UMR7645, INSERM U1182

Quantitative Study of Membrane Nano-organization by Single Nanoparticle Imaging

Thèse de doctorat

Chao YU

Thèse devant être soutenue à Palaiseau le 24 juillet 2019

Membres du jury

Benoît LADOUX……Rapporteur
Cécile SYKES……Rapportrice
François TREUSSART……...Examinateur
Daniel GILLET……Examinateur
Antigoni ALEXANDROU……..Co-directrice de thèse
Cédric BOUZIGUES……...…Directeur de thèse

Acknowledgments

I am grateful to the reviewers Cécile Sykes and Benoît Ladoux, the president François Treussart, and Daniel Gillet, members of the Jury, for their work, evaluation and helpful feedback on my work. I was generously funded by the Ecole Doctorale de l'Ecole Polytechnique (EDX), Triangle de la physique and INSERM.

Foremost, I wish to express my gratitude to my two supervisors who brought me into the Laboratoire d'Optique et Biosciences and guided my professional journey. I have felt fully supported while working with them:

I would like to thank my supervisor Cédric Bouzigues for his invaluable guidance, for his outstanding and exceptional knowledge and patience during my research, for his brilliant ideas and sense of humor in discussion; for his helpful and high-efficiency feedbacks on my publications, presentations, and manuscripts; also, for all his motivation and encouragement. I am honored to have had such a chance to be his student for my Ph.D. degree. Thank you, Cédric.

I would like to thank my co-supervisor Antigoni Alexandrou. My gratitude to her is beyond words. I appreciate all the constant support during the last years. Thanks for picking me up at CDG on my first day in France; for her academic advice and positive attitude in my research; for all her help with the administration; for her great deal of encouragement during my difficult period; moreover, for her easy-going personality and laughs. I cannot thank her enough for all her help in my research and my life. Thank you, Antigoni. I hope I can repay all your kindness and be a good researcher like you one day.

I would also like to thank Max Richly, whose work I continued, who did experiments with me and guided me to do data analysis at the beginning of my research. I also thank Rivo Ramodiharilafy, Thi Thuy Huang for their help for my experiments.

I am grateful to our collaborator Daniel Gillet and Thierry Gacoin that made the project possible. My gratitude also goes to the people in my research group, Rachid Rezgui, Mouna Abdesselem, Pascal Preira, Hélène Lazareth, Nicolas Pétri, Marlen Kruse, Laurène Jaubert, and Fanny Mousseau who were always there to help and motivate.

I want to thank Laure Lachapelle and Christelle Francais, thank you for all the administration work, Jean-Marc Sintes, Xavier Solinas, Simon Dadoun and Ernan Roitman for their technical support.

I am thankful to the people who used to share my office at Aile 3, Mouna, Marianne, Floriane, Kamel, Vincent and who shared my office at Bât. 84, Margaux, Minh Son, Clothilde, Yoann, and Anastasia. I am very glad to have shared a wonderful adventure with all of you.

I would like to thank the entire LOB laboratory for providing a friendly and international environment and all the LOB members for their warm smiles.

Also, thanks to my family and all my friends.

2019/09/12, à Palaiseau

Table of Contents

Introduction

Cell membrane nano-organization is essential for regulating some cell functions, notably through signaling processes involving membrane investigating, biomolecule interactions in the cell membrane, the biophysical properties and the dynamics of membrane nanodomains in living cells can thus provide crucial information to understand the membrane organization role in many cell activities.

Complex patterns of lateral organization can be understood by a set of organizing principles involving lipid-lipid, lipid-protein, and protein-protein interactions. However, most of the organization mechanisms are not yet fully understood. Among the known membrane nanodomain structures, we can notably cite raft domains, enriched in cholesterol and saturated sphingolipids “picket-and-fence” domains due to actin filaments (fences) and to proteins transiently anchored to them (pickets), confinement due to anchoring to the actin cytoskeleton, protein clusters, tetraspanin-enriched nanodomains, and caveolae and clathrin-coated pits. We focused on the two most widely studied ones, lipid rafts and picket-and-fence nanodomains and used novel biophysical tools to shed new light into their properties.

The goal of this thesis entitled “Quantitative study of membrane nano-organization by single nanoparticle imaging” is to study receptor/membrane nanodomain/ cytoskeleton interactions and to provide a comprehensive picture of the confined motions of different membrane receptors based on labeling, imaging and hydrodynamic force generation by luminescent $Y_{0.6}\,Eu_{0.4}\,VO_4$ nanoparticles.

This work was performed in the Laboratoire d’Optique et Bisosciences, Ecole polytechnique, CNRS, INSERM, in the “Nanoimaging and Quantitative Biology” team and is a continuation of two previous theses in our research team, that demonstrated the efficiency of single receptor tracking through lanthanide-based nanoparticle imaging. In this thesis, we built upon the previous work to provide a more global understanding of membrane nano-organization. For this purpose, we chose three types of membrane receptors, which were assumed to undergo

different types of confined motion in the cell membrane, with a special focus on the EGF receptor, which is furthermore particularly important because of its involvement in various pathologies, such as some cancers [1] [2].

1) EGF receptor, which is expected to be confined in membrane raft domains [3], [4] and is capable of direct interaction with the actin cytoskeleton [5];
2) Transferrin receptors (TfRs), which are not expected to be associated with rafts [6];
3) CPεT receptor, which has been reported to be confined in membrane raft domains [7].

Different orginal techniques were used in this work both experimentally and for the quantitative data analysis:

i) Nanoparticle-based single-molecule long-term tracking with highly bright and photostable luminescent nanoparticles, $Y_{0.6}\,Eu_{0.4}\,VO_4$;
ii) Local force generation through nanoparticle-amplified hydrodynamic flow in microfluidic systems and
iii) Bayesian inference;
iv) Statistical physics approaches for the classification of membrane receptor motions.

Applying single particle labeling and long-term tracking on EGF receptors, we directly investigated their diffusion and confinement in the cell membrane, while using an epi fluorescence microscope. The trajectories were then analyzed using Bayesian inference to extract, in addition to the diffusion coefficient, the energy landscape experienced by the receptors. Additionally, two classification approaches, a decision- tree information criteria and a clustering approach, were used on EGF, CPεT and Tf receptor trajectories, to classify the different confinement potentials (Chapter 1 and 3).

We then developed system designed to apply controlled forces through flows to nanoparticles on labeled biomolecules. We first demonstrated the efficiency of this approach, by studying biomolecule dissociation between membrane receptors and their pharmaceutical ligands. We notably investigated binding and dissociation kinetics in high affinity receptor-ligand pairs where

dissociation is particularly slow and therefore not measurable with existing techniques (Chapter 2).

We then used this method in living cells, to gain further insight about the organization of the membrane. We thus generated a nanoparticle-amplified external hydrodynamic force on both raft-associated receptors, EGFR and CPεT receptor, and a non-raft receptor, the transferrin receptor, and notably revealed sets of interactions between membrane proteins with an actin-binding domain like EGFR, membrane nanodomains, and the underlying actin cytoskeleton. (Chapter 4).

This work thus both present a quantitative insight in membrane receptor, notably EGFR, organization mechanisms at the nanoscale, and establish an methodological framework with which different type of membrane properties could be investigated.

Chapter 1
Single Nanoparticle Imaging with Force Application

Single-molecule observations are particularly important in biology because molecular behaviors may show large inter-molecular variability, dual or multiple subpopulations with different behaviors, and transitions from one behavior mode to another. All this type of information is lost in ensemble measurements. Single-molecule observations offer the possibility to build the full distribution of behaviors and moreover give access to molecular dynamics as each single molecule is observed as a function of time.

Single-molecule tracking (SMT) refers to a class of techniques that involve direct spatial observation of individual molecules or particles as a function of time. With both high temporal and spatial resolution, it has been used extensively to advance our understanding of the plasma membrane and the mechanisms controlling the movement of cell surface proteins and to provide fundamental insights into membrane organization and complex cellular processes.

1.1 Single Nanoparticle Imaging and Tracking

There are several approaches that have been applied for tracking individual molecules in the plasma membrane of living cells : approaches using non-fluorescent particles like large latex or polystyrene beads, or metal particles which are large enough to be detected by optical microscopy through the reflected, the absorbed or scattered light, and approaches using luminescent labels such as fluorescent organic dyes or proteins [1,2], and inorganic particles like quantum dots (QDs) [3,4], rare-earth-doped oxide nanoparticles [12], [13], and nanodiamonds [14].

In this work, we used 30-50 nm rare-earth-doped oxide nanoparticles $Y_{0.6}Eu_{0.4}VO_4$ as luminescent labels of membrane receptors. Compared to organic fluorophores, these nanopaticles show very high photostability without photobleaching and without blinking, unlike quantum dots. In our laboratory, we coupled a controlled number of α-prototoxin, ε-prototoxin and streptavidin molecules to these nanoparticles after appropriate functionalization, which allows us to do long-term tracking single receptors specifically on the cell membrane (see Chapter 3.2).

$Y_{0.6}Eu_{0.4}VO_4$-ligands are used as labels of membrane receptors, which have been activated by specific ligands. To localize single labels on the cell membrane with high precision, the concentration of labeled receptors in the microscope field is controlled as 10-20 per cell. Also, controlled numbers of ligands coupled on the $Y_{0.6}Eu_{0.4}VO_4$ ensured that trajectories of a single particle present the behaviors of the single receptor. Indeed, if the number of ligands is too large, one nanoparticle may bind to multiple receptors (see Chapter 3 for more details).

In general, the diffraction of light limits the resolution of optical microscopes. A point source of light at the focal point of the microscope gives rise to an image with a light distribution of a certain width. This is the impulse response of the optical system called point spread function (PSF) and can be experimentally determined by imaging a point source of light. The finite width of the PSF implies that two point sources that are close enough to each other cannot be distinguished from each other and will be seen as a single emitter. Abbe calculated in 1873 the full-width at half-maximum (FWHM) of the PSF to be given by $d = \frac{\lambda}{2NA}$, where λ is the wavelength of light and NA is the numerical aperture of the imaging optics. Rayleigh postulated empirically that two point sources can be distinguished from each other if their distance is larger than the FWHM of the PSF which is known as the Rayleigh criterion and defines what is known as the microscope resolution [15]. For wavelengths in the visible spectrum and for large numerical apertures of 1.4, the diffraction limit is around 200-300 nm.

However, SMT technique can be achieved because it is possible to determine the localization of a single emitter, such as a 30-nm nanoparticle, with a precision much higher that the FWHM of the PSF [16].

To describe the shape of PSF, the Richards-Wolf model [17] and the Gibson-Lanni model [18] are highly accurate methods, but with complex evaluating integrals, and the Airy disk PSF, which describes the intensity at the point (**x**, **y**) of the paraxial, is simpler and sufficient in many investigations. Furthermore, in most cases the Airy disk PSF (Fig. 1.1) can be well fitted with the approximate Gaussian PSF model [19] which leads to faster fitting and gives useful and reasonably accurate results. Indeed, in the usual SMT signal-to-noise conditions the side peaks of the Airy PSF are not distinguishable. We thus used fitting with a 2D Gaussian to determine the localization of our emitters in our receptor tracking analysis, as shown in equation 1.1, where σ_{xy} refers to the Gaussian standard deviation. The localization of the emitter is then the center ($\mathbf{x_0}$, $\mathbf{y_0}$) of the Gaussian fit.

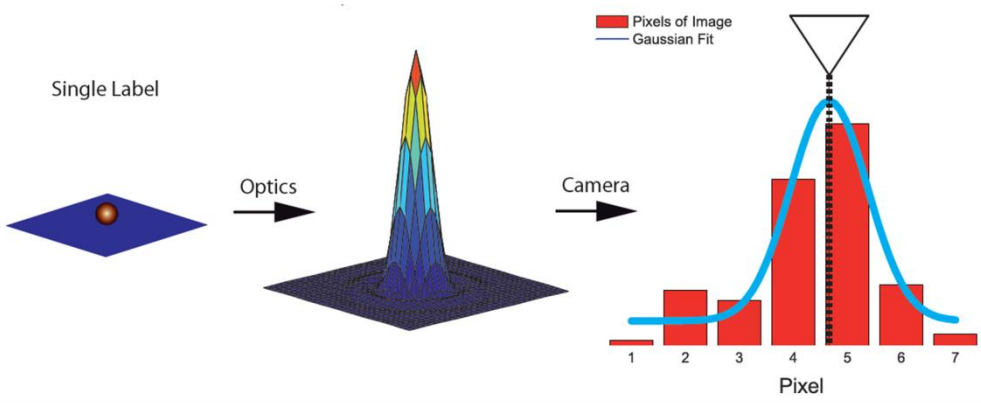

Figure 1.1 Schematic of the Gaussian fitting process to obtain precise localization: a pixilated image of the Airy diffraction pattern is first acquired by the camera, and then fitted with a Gaussian to obtain a precise localization from the function's maximum. Figure reproduced from [12].

$$PSF_{Gaussian} = A\ exp\left(-\frac{(\boldsymbol{x}-\boldsymbol{x_0})^2+(\boldsymbol{y}-\boldsymbol{y_0})^2}{2\sigma_{xy}^2}\right) \quad (1.1)$$

The localization accuracy is then determined by the error bar of the fitting process on the localization of the peak of the Gaussian. This accuracy can be improved by collecting more photons. Webb et al. gave an estimate of the localization accuracy Δx considering that N detected photons with a standard deviation s of the PSF is equivalent to N measurements of the emitter localization with error s for each photon and using the standard error on the mean [20], [21]:

$$\Delta x = s/\sqrt{N} \tag{1.2}$$

This estimate is exact in the case were recording is performed with low technical noise, allowing an acquisition in a shot noise regime. Although more photons are collected by increasing the acquisition time, the time resolution is obviously decreased. If the emitter moves significantly during the acquisition time, i.e. over distances much larger than the localization accuracy, then the acquired images will appear blurred and broader than the width determined by the PSF. In our tracking experiments, for diffusion coefficients on the order of 0.1 $\mu m^2/s$, which is typical of the diffusion coefficients of membrane proteins investigated in this work, the observed emission spots start to be blurred at acquisition times above 50 ms. We therefore limit our acquisition times to no more than 50 ms, in order to achieve a typical localization accuracy of 10-20 nm.

Single-molecule tracking requires low-density labeling. Extension of single-molecule tracking to high-density labeling has given rise to one branch of super-resolution techniques, PALM/STROM. Indeed these techniques, which will be discussed in Chapter 3, rely on the ability to determine the location of a single molecule with a precision that is higher than the microscope resolution. Tracking at high-labeling conditions has been called sptPALM [22]. However, in the latter case, the trajectories are very short, with a typical total duration $\tau \sim 750$ ms. Therefore, single-molecule tracking at low density still has significant advantages and a high potential of contribution to new knowledge in biology, notably in order to reveal membrane nano-organization in cells, which requires the recording of long single trajectories, as detailed below.

1.2 Force Measurements at the Single Molecule Level

Molecule-scale forces play a fundamental role in biological interactions and in all cell processes like cell motility, cellular signaling, and transport. Measuring and understanding the forces that govern specific interactions is a challenging task in biology at the molecular level, since it requires probing nanoscale events, with typical pN sensitivity. In the last 30 years, the ability to measure forces at the single-molecule level has however been improved in a spectacular manner by the development of various single-molecule manipulation techniques, including atomic force microscopy (AFM) [1,2,3], optical tweezers [25], magnetic tweezers [26], and flow-induced stretching.

1.2.1 Atomic Force Microscopy

Atomic force microscopy (AFM) was developed in 1986 by Binnig et al. [27]. It is a modified version of the scanning tunneling microscopy combining the apparatus with a profilometer which enables mapping of the surface characteristics at high spatial resolution. It was initially implemented for the analysis of metals and semiconductors or insulating surfaces [1]. In AFM, a tip connected to a cantilever passes over the surface of a sample and changes of the sample topography induce movement of the cantilever. A laser beam is reflected by the cantilever and the motion of the cantilever is translated into a deflection of the reflected laser beam which is detected by a four-quadrant photodetector [23]. This topographic information is obviously precious for biological samples and has been extended to molecules and living cells in water [28]. Thus, AFM is a tool for biological applications with simple and rapid sample preparation [2, 4].

To measure inter-and intra-molecular interaction forces with pN resolution, most AFM studies on living cells apply chemical or biological functionalization of the AFM tip which interacts specifically with cell surface receptors [30]. Depending on the force measurement mechanism, there are several AFM modalities including single-molecule force spectroscopy (SMFS), chemical

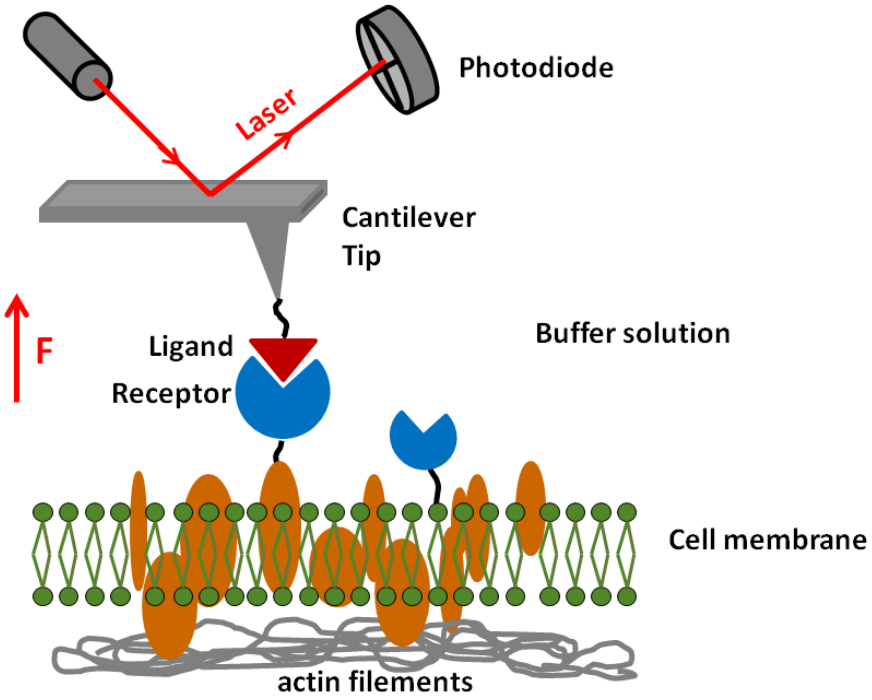

Figure 1.2: AFM applied for force measurements between ligand and receptor on the membrane of a living cell.

force microscopy (CFM), single cell force spectroscopy (SCFS), and molecular recognition mapping (MRM). An example of single-molecule force measurement is shown in figure 1.2. The AFM consists of a cantilever with a tip functionalized with a ligand specifically interacting with its receptor on the cell membrane. Deflection of the cantilever is measured by recording the positions of a low power laser beam reflected off the cantilever on a four-quadrant photodetector. The deflection-displacement curves are recorded both during tip-sample

approaching and ligand-receptor separating by pulling continuously the sample stage along the force direction as shown in Fig. 1.2, and are then transformed into single-molecule force-distance curves. The force-distance curves during ligand-receptor approach give information on height, surface forces, and mechanical deformations of the sample. The adhesion force can be extracted from the force-distance curves during the separation period. A modern technology of single-molecule force spectroscopy records thousands of force-displacement curves at different sample locations to obtain sample "force" imaging, which provides a powerful tool to quantify mechanical and force properties of complex biological systems [31]–[34]. However, the limitation of AFM is that it requires highly stable equipment which is quite difficult to implement.

1.2.2 Optical Tweezers

Optical tweezers is a powerful single-molecule manipulation technique initiated by Ashkin et al. in the 1970s [25]. It relies on focusing a laser beam to a diffraction-limited spot in the specimen plane with a high numerical aperture microscope objective. This single-beam force gradient trap provides an attractive force by the electromagnetic field on the order of pN to hold and move small particles such as polystyrene, silicon beads, and microorganisms without physical contact [25], [35]. These optical traps can be used both for the manipulation of objects in the size range of 5 nm up to several microns as well as for measuring interaction forces in the pN range [22]–[24].

Optical tweezers involve the balance of two types of optical forces: scattering forces (or radiation pressure forces) which push objects along the direction of propagation of the light and gradient forces which pull objects along the spatial gradient of light intensity. When gradient optical forces exceed those due to scattering, an object is attracted to the point of highest intensity formed by focused light and can be stably trapped at this position in all three dimensions [39]. This optical trap can be well approximated as a linear spring; the spring constant depends on the steepness of the optical gradient. Since the 1990s, optical tweezers have been applied to the biological sciences, starting by trapping an individual tobacco mosaic virus and *E. coli* by Ashkin et al. [40].

Thanks to the capabilities of holding and moving trapped objects, optical tweezers have been proven to be versatile tools in quantitative biophysics to observe the forces due to biological molecule interactions, including interactions between cells and bacteria [41].

For measuring forces, the experimental system is based upon optical tweezers combined with a sensitive position detection system. A trapped particle in the focus of the high numerical aperture microscope objective behaves like a mechanical spring in response to an external force. The displacement of the particle from the equilibrium position is thus a direct measure of the exerted force. A weak probe laser beam, focused directly below the trapping focus, is used for position detection of the trapped particle. The microscope condenser focuses the probe light scattered by the particle to a distinct spot in the far field, monitored by a position-sensitive detector (typically a four-quadrant photodiode) to determine the exerted force. This system has been used, for example, to measure the binding forces between *Escherichia coli* bacterial adhesins and galactose-functionalized beads [41] and the interaction forces between human bone cells and implant surfaces [42].

Even though holographic techniques have been used to generate multiple traps with the same laser beam [43], optical tweezers, like AFM, is a technique that is difficult to parallelize.

1.2.3 Hydrodynamic Forces in Microfluidic Channels

The techniques described above, both AFM and optical tweezers, are very efficient in generating and measuring forces in a very precise manner. But they both need quite sophisticated equipment and optimization and are difficult to parallelize. In my thesis work, we have implemented a simpler and inherently parallelized way for generating and measuring forces by applying a hydrodynamic flow in microfluidic channels. Moreover, this force generation takes place in water, in the native environment of cells. We then can calculate the flow forces acting on the particles by the following equation (more details are presented in section 2.2.3.):

$$\boldsymbol{F}_d = 6\pi\eta r\boldsymbol{v}_{flow} \tag{1.3}$$

Where η is the liquid viscosity which, far from solid surfaces (for details see Chapter 2), can be assumed equal to the water viscosity that is $\eta=\eta_{water}=0.001$ Pa·s, r is the nanoparticle (NP) hydrodynamic radius which can be estimated from the emitted photon number with 10% precision, as explained in Ref. [44] and in Chapter 2, and $\boldsymbol{v}_{flow}$ is the velocity of the liquid which can be determined theoretically by using the Poiseuille equation or experimentally using particle imaging velocimetry (PIV) at the precise location of interest in the microfluidic channel.

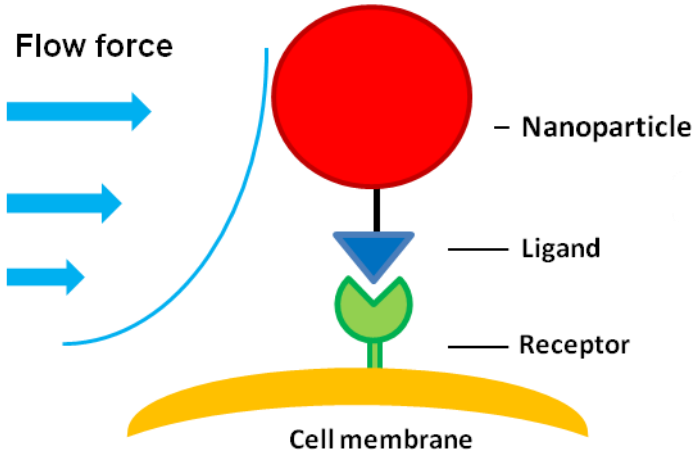

Figure 1.3: Schematic of a receptor-bound nanoparticle inside a microchannel in a constant flow rate.

We can bind a biomolecule, e.g. a membrane receptor, at the inner glass surface of a microchannel and then let it specifically interact with a ligand which is bound to a particle (Fig. 1.3). The liquid flow we add on the particle can be transformed into force applied to the conjugate between ligand and receptor. The force can be tuned easily by tuning the flow rate, which can be potentially large enough to detach the ligand from the receptor. This technique can also be applied to cells, with a molecule A on the cell surface and a molecule B bound to the particle, to measure the interaction forces between the two molecules. More details are presented in chapter 2. In this work, we used luminescent nanoparticles, so that we can measure the displacement of the particle by detecting the positions under a fluorescent microscope, and obtain the receptor displacement.

Two main advantages of this force application and measurement technique are that it doesn't require sophisticated material nor sophisticated calibrations, like in the case of optical tweezers, and that it is inherently multiplexed because the same hydrodynamic force is applied everywhere in the microchannel on multiple particles at the same time, which is much more difficult to do with the other techniques. Indeed, the standard AFM technique has to scan the whole sample and the optical tweezers technique has to create multiple focal points of the laser beam with enough excitation intensity to investigate multiple sample locations [43]. In addition, the measurements can be performed in the native environments of cells.

Moreover, our approach based on amplifying the flow force by the presence of the nanoparticle can apply a relatively high force on the molecules of interest, while applying a flow rate that is small enough to avoid cell perturbation.

In our technique, the difficulty is to determine precisely the relation between the flow rate and the force. Indeed, the presence of cells may perturb the flow speed as a function of height in the microchannel away from the predictions for Poiseuille flow. In addition, it is not clear where the zero-flow speed plane is in the presence of cells. It is therefore preferable to measure the flow speed at the height z using particle velocimetry. This point will be discussed in chapter 4.

We can point out that, as discussed below in section 1.3.2, single-molecule tracking combined with Bayesian inference analysis based on the Langevin equation of motion describing diffusion in a potential is also capable of extracting the forces acting on the single molecule.

1.3 Approaches for Single Nanoparticle Trajectory Analysis

Obviously, it is important to record single molecule trajectories in the appropriate experimental conditions (see section 1.1), notably to ensure a maximal localization accuracy. Afterwards, the important issue is to use the appropriate technique to analyze the trajectories in order to extract the largest and most relevant amount of information possible from the recorded data and obtain quantitative information on cellular parameters.

1.3.1 The Mean Square Displacement (MSD)

Once the data processing of single-particle tracking is performed and the trajectories are obtained, the final step involves analyzing the trajectory, testing particle dynamics, describing them in terms of the type of motion and quantifying the diffusion parameters.

The most common approach for analyzing single molecule trajectories consists in the calculation of the mean square displacement (MSD), which describes the average extent of space explored by a particle as a function of time lag t.

Calculations for the 2D case are shown as follows [45]:

$$\langle r^2 \rangle = 4Dt \qquad normal\ free\ Brownian\ diffusion \quad (1.4)$$

$$\langle r^2 \rangle = 4Dt^{\alpha} \quad a < 1 \qquad anomalous\ diffusion \quad (1.5)$$

$$\langle r^2 \rangle = 4Dt + (Vt)^2 \qquad directed\ motion\ with\ \ diffusion \quad (1.6)$$

$$\langle r^2 \rangle \cong \langle r_C^2 \rangle [1 - A_1 \exp(-4A_2 Dt / \langle r_C^2 \rangle)] \qquad corralled\ \ diffusion \quad (1.7)$$

The dependence of the MSD with t is related to the type of motion performed by the particle. For Brownian diffusion, the MSD can be calculated as the variance of the solution of the diffusion equation and it can be shown to scale linearly with t, as shown in equation 1.4, where D is the diffusion coefficient (see Fig. 1.3). However, in many biological systems, it has been observed that particles often display anomalous diffusion [46], described by a power law scaling as shown in equation 1.5, where α is the anomalous exponent, in which $\alpha<1$, and is usually referred to as sub-diffusion, whereas $\alpha>1$ is called super-diffusion (see Fig. 1.3). Another important type of motion observed in biological systems is the directed motion, as shown in equation 1.6, characterized by a ballistic movement or active transport with speed V, and is observed for the motion of molecular motors and active transport along microtubules [47].

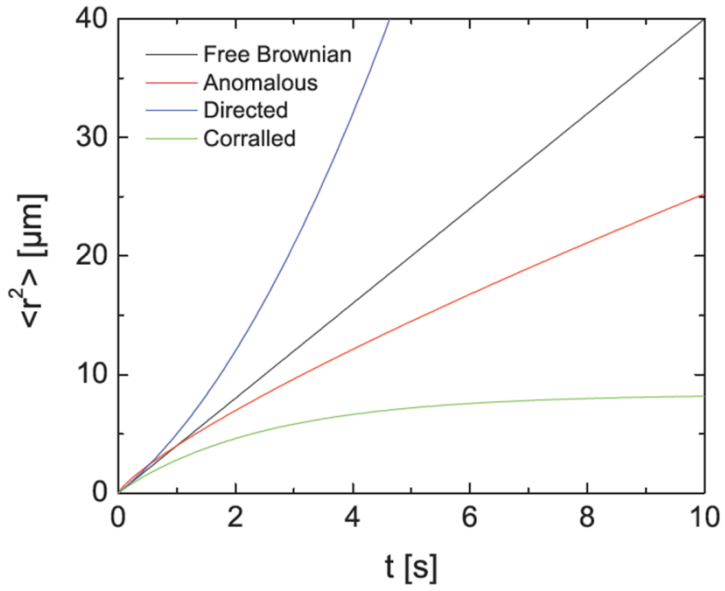

Figure 1.4: MSD plots of the different motion models. 2D free Brownian motion with a diffusion coefficient of 1 µm^2/s (black line), directed motion with a speed of 1 µm/s in addition to Brownian diffusion (blue line), confined (or corralled) diffusion with a $r_c = 5\ \mu m$ size of the confinement domain (green line), and anomalous diffusion with α of 0.8 (red line). Figure extracted from [12]**.**

A confined type of diffusion, due to the presence of compartments constraining particle diffusion within finite regions of space has also been observed and described in Ref. [48]. Although in this case the exact dependence of the MSD on lag time t depends on the shape of the confining region and on the dimensionality of the space, the general effect of this confinement is to produce a plateau in the MSD curve at large lag times and a useful formula approximating this behavior is given by equation 1.7 where r_C is the corral size, and A_1 and A_2 are constants determined by the corral geometry [48], [49]. Note that this equation assumes a flat potential inside the confinement domain and infinite barriers at the border.

1.3.2 Bayesian Inference Analysis

In the previous paragraph, we indicated that the MSD approach discards a lot of information when calculating the average square displacement. Indeed, it does not exploit the individual $(x_1, y_1, t_1) \rightarrow (x_2, y_2, t_2)$ trajectory steps which contain information on the force acting on the diffusing molecule. In addition, it discards information on transient or local effects. To better exploit the available information, recently, a new technique has been proposed by Jean-Baptiste Masson [50], [51] that is very adequate to describe confined motion where a large amount of trajectory points explore the same area. This technique is based on statistical physics analysis, in particular on Bayesian inference. In the case of our trajectories, we can use Bayesian inference to extract the parameters of the unknown potential leading to confinement. In the framework of the inference technique, we assume that motions of membrane receptors are following the Langevin equation, which is the general equation describing the motion of a particle diffusing in a potential:

$$\frac{d\boldsymbol{r}}{dt} = \boldsymbol{v} \qquad m\frac{d\boldsymbol{v}}{dt} = -\gamma\boldsymbol{v} - \boldsymbol{\nabla}V(\boldsymbol{r}) + \sqrt{2D\gamma^2}\xi \tag{1.8}$$

Where γv accounts for friction and the friction coefficient γ is constant, $-\boldsymbol{\nabla}V(\boldsymbol{r})$ is the force created by an arbitrary potential $V(\boldsymbol{r})$ responsible for the confinement, and $\sqrt{2D\gamma^2}\xi$ is the noise term describing the Brownian motion. Here, we are making the assumption of the most simple model possible, i.e. that the receptors undergo Brownian motion in the presence of an unknown potential that we will infer from the trajectory.

Inside the cell membrane, we assume that steady state conditions are reached very fast (the equilibration time being $\tau = m/\gamma \approx [10^{-18} - 10^{-10}]$s). Therefore, $\frac{d\boldsymbol{v}}{dt} = 0$ and equation 1.8 yields for the velocity:

$$\frac{d\boldsymbol{r}(t)}{dt} = -\frac{\boldsymbol{\nabla}V(\boldsymbol{r}(t))}{\gamma} + \sqrt{2D}\xi \tag{1.9}$$

The Fokker–Planck equation [52] associated to equation 1.9, which controls the evolution over time of the transition probability $P(\boldsymbol{r}_2, t_2|\boldsymbol{r}_1, t_1)$ for the moving molecule to go from one space-time coordinate $(\boldsymbol{r}_1, t_1)$ to the next $(\boldsymbol{r}_2, t_2)$, is given below, where $\boldsymbol{F} = -\boldsymbol{\nabla}V$:

$$\partial_t P = -\frac{1}{\gamma}\boldsymbol{\nabla} V \cdot (\boldsymbol{F}P) + D\Delta P \tag{1.10}$$

If **F** and D are constant, the Fokker–Planck equation can be solved analytically to yield:

$$P(\boldsymbol{r}_2, t_2|\boldsymbol{r}_1, t_1) = \frac{exp\,(-\frac{(\boldsymbol{r}_2 - \boldsymbol{r}_1 - \boldsymbol{F}(t_2 - t_1)/\gamma)^2}{4D(t_2 - t_1)})}{4\pi D(t_2 - t_1)} \tag{1.11}$$

By segmenting the confinement domain in $i \times j$ subdomains where F and D are constant, any potential shape can be analyzed based on equation 1.11 which will apply in each subdomain. Because the process is Markovian, we can then obtain the overall probability of a trajectory **T** with N space-time coordinates $(\boldsymbol{r}_n, t_n)$ given $\boldsymbol{F}$ and D, i.e. the likelihood function, $P(T|D, F)$, as follows:

$$P(\boldsymbol{T}|D, \boldsymbol{F}) = \prod_{all\ transitions} P(\boldsymbol{r}_{n+1}, t_{n+1}|\boldsymbol{r}_n, t_n) \tag{1.12}$$

Taking into account the subdivision of the trajectory, **T**, in square subdomains determined by the column number **i** and row number **j**, equation 1.12 reads:

$$P(T|D, \boldsymbol{F}) = \prod_{\boldsymbol{i},\boldsymbol{j}=1}^{\boldsymbol{i_{max}},\boldsymbol{j_{max}}} P\left(T\middle|D_{ij}, \boldsymbol{F}_{ij}\right) \tag{1.13}$$

Here, we can use Bayes' theorem to obtain the probability of each parameter Q for a given trajectory T, i.e. the posterior probability$P(Q|T)$:

$$P(Q|T) = \frac{P(T|Q)P_0(Q)}{P_0(T)} \tag{1.14}$$

where $P_0(Q)$ represents the prior knowledge about *D* or *F*, known before the realization of the trajectory T. $P_0(Q)$ is constant for a reasonable range of parameter values and 0 elsewhere. $P_0(T)$ is a normalization constant which is set to 1.

As in Refs. [50], [51], [53], we performed an optimization with Broyden-Fletcher-Goldfarb-Shanno algorithm [54] to find the parameter values maximizing the posteriori probability $P(Q|T)$ to yield a value for the inferred parameter. A Monte Carlo exploration of the

posteriori $P(Q|T)$, through the generation of synthetic trajectories with parameters around the maximal values, yields the width of the posteriori distribution, which determines the uncertainty of the inferred value.

In order to satisfy the criterion of a constant force, we have to split the trajectories (Fig. 1.5A) into ($i \times j$) subdomains. For the inference of the confinement forces, there are two different approaches. We can either infer forces, optimized independently, in each subdomain ($\boldsymbol{F}_x, \boldsymbol{F}_y$) to extract the force maps, or alternatively consider that the confining potential is a polynom, of degree 2, 3 or 4, and directly infer the parameters of this polynomial potential (see Fig. 1.5 B), which is identical for all subdomains. The second approach was used in this work. As will be discussed in Chapter 3, the potential dictating some receptor motions is well described by 2nd-order potential, where the potential is: $\mathbf{V}(\mathrm{x},\mathrm{y}) = \mathrm{C_{xx}x^2} + \mathrm{C_{yy}y^2} + \mathrm{C_{xy}xy} + \mathrm{C_x x} + \mathrm{C_y y}$. If the linear terms are negligible, the potential matrix can be diagonalized to yield: $\mathbf{V}(\mathrm{x},\mathrm{y}) = \frac{1}{2}\mathrm{k_X x^2} + \frac{1}{2}\mathrm{k_Y y^2}$, with $\mathrm{k_r} = \sqrt{\mathrm{k_X}^2 + \mathrm{k_Y}^2}$, $\mathrm{k_r}$ giving the stiffness of the potential spring constant. For receptors outside lipid-enriched raft nanodomains, a 4th-order potential was found to be more appropriate, as will be discussed below.

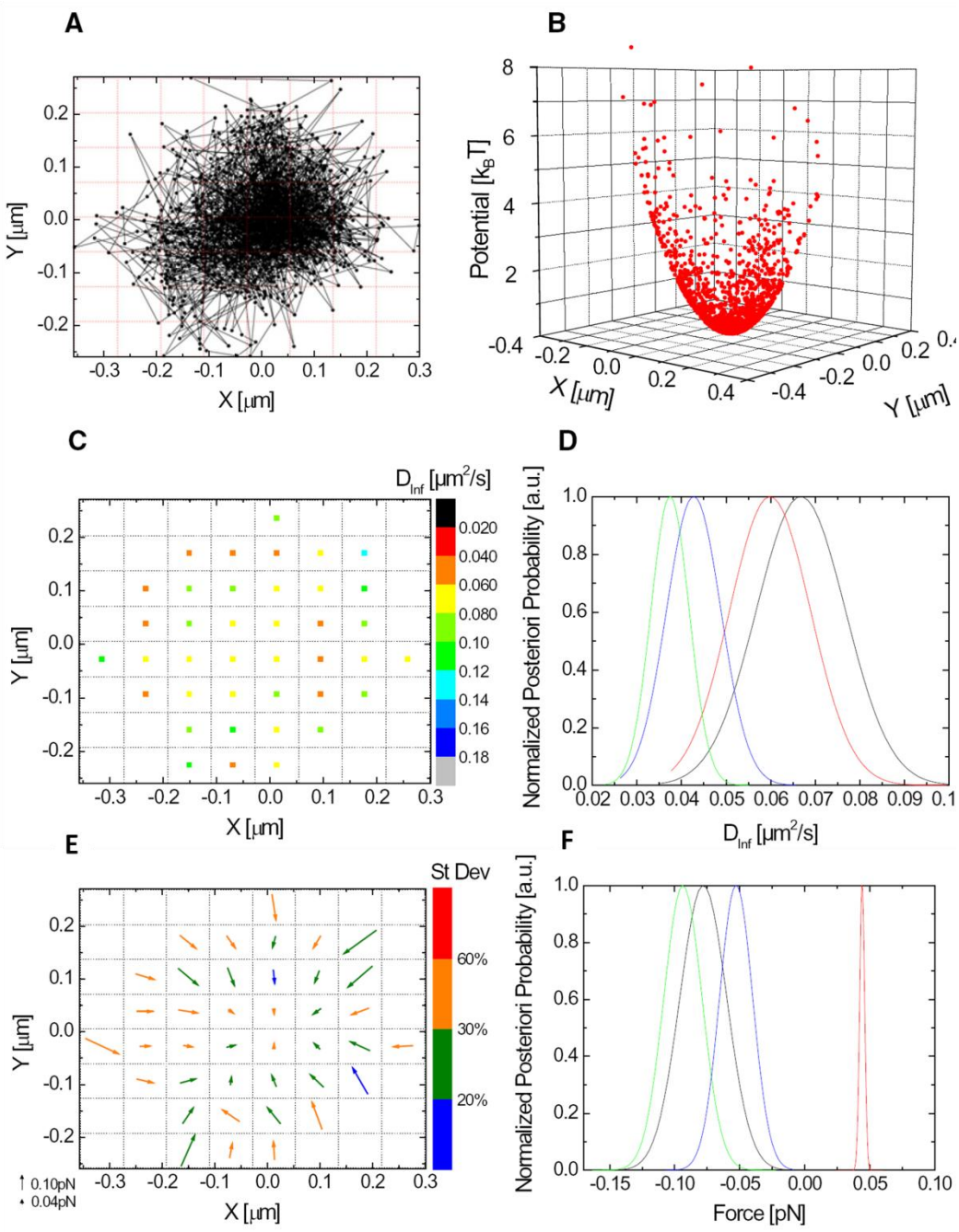

Figure 1.5: Bayesian Inference analysis of a 1500-frames trajectory (A) of a single CPεT receptor on the cell membrane (acquisition time: 51.3 ms), (B) the inferred confining potential, (C) the inferred diffusivity map (average inferred diffusion coefficient $D_{inf} = 0.08 \pm 0.003\ \mu m^2/s$) and (E) the inferred force map (the strength of the

inferred forces is proportional to the arrow length and arrow color coding is based on the standard deviation). (D) Posterior probability distribution of four diffusion coefficients in the diffusivity map in (C). (F) Posterior probability distribution of four forces in the force map in (E). Figure are extracted from Ref. [53]**.**

The inferred parameters Q are, in the case of a 2nd-order potential, the diffusivity D and the confinement potential coefficients $\mathrm{C_{xx}}, \mathrm{C_{yy}}, \mathrm{C_{xy}}, \mathrm{C_x}$ and $\mathrm{C_y}$. This yields 5+1 independent parameters to infer and 15+1 in the case of a 4rth-order potential. In the confining domain of the cell membrane, the diffusion coefficient D_{inf} is assumed to be constant and is evaluated globally for the trajectory. In Ref. [53], the diffusion coefficients were inferred separately for each subdomain, which lead to $\mathrm{i} \times \mathrm{j}$ D_{ij} inferred parameters. Small variations between the different D_{ij} values showed that a constant D_{inf} parameter is a good approximation [53] (Fig. 1.5C). The experimental confinement potential is at first assumed to be a polynomial of high order, e.g. 4th-order. The order is then reduced to 2nd-order and we check if there is a significant difference between the two potentials using a Kolmogorov-Smirnov (KS) analysis (see Fig. 3.9). As explained in Chapter 3, it turns out that a 2nd-order polynomial is good enough to describe the confining potential of our experimental trajectories in the case of receptors confined in cholesterol- and sphingolipid-rich raft nanodomains but a 4th-order potential is necessary for transferrin receptors undergoing hop diffusion outside rafts.

Two important points have to be kept in mind when choosing the size of the subdomains. First, the choice of the subdomain size is a compromise between a big enough and a small enough size. There must be enough data points, at least 10 [50], in each subdomain to be able to extract the motion parameters (in practice the algorithm optimizes the force values (F_x, F_y) in each subdomain). Therefore, the subdomain should be big enough to encompass enough trajectory points. However, if the subdomain is too big we will not have enough spatial resolution for the potential. Another issue concerns the trajectory points in each subdomain entering or going out from the subdomain to another subdomain. By definition, for each subdomain we take into account all steps that have their starting point inside the subdomain. This means that the

number of trajectory steps entering or exiting a subdomain has to be negligible with respect to the total number of trajectory steps taking place inside the subdomain.

Bayesian inference analysis assuming Langevin equation describing diffusion inside a potential is thus capable of extracting both the diffusion coefficient *D* and the energy landscape experienced by a receptor inside its membrane confinement domain (Fig. 1.5B). In comparison to the previously discussed force-displacement measurement techniques, it is noteworthy that this approach is capable of measuring the force map (Fig. 1.5 E) acting on membrane receptors inside a confinement domain in the absence of any externally applied force or displacement, simply by recording the molecule trajectory (Fig. 1.5 A).

1.4 Decision Tree and Clustering for Trajectory Classification

Biomolecules in the cell membrane are known to undergo a variety of different types of motion, and even to switch from one type of motion to another. This makes it difficult to classify their motion. Commonly, a large set of membrane receptors are confined in microdomains. Previous work [32] has indicated that the confinement in cholesterol-enriched microdomains is due to a 2nd order confinement potential. As discussed in more detail in Chapter 3, we expect, in contrast, the situation to be different for membrane receptors outside rafts experiencing steric hindrance in their diffusion due to underlying actin filaments. In this case, we expect the potential landscape to be flat away from the actin filaments providing steric hindrance and to increase abruptly in the vicinity of the filaments. This potential shape can be better described by a fourth-order potential or by a composite potential that is flat in the center and exponential at the domain border than by a second-order confinement potential.

In this context, we want to be able to distinguish between different types of motion and, in particular, between 2^{nd}-and 4^{th}-order confinement potentials in a more rigorous manner. We therefore applied in this thesis a Bayesian inference decision tree (BIDT) approach [55], [56] and

a data clustering classification scheme [56] to analyze the mode of motion of membrane receptors.

1.4.1 Bayesian Decision Tree

The Bayesian inference decision tree (BIDT) approach is based on a set of information criteria to distinguish between different types of motion. This method was proposed by Türkcan and Masson [55]. It is based on Bayesian inference to calculate the posterior probability of an observed trajectory for all the possible models and then uses information criteria to find out which motion model minimizes the value of the information criteria. The information criteria considered were the Bayesian information criterion (BIC), the Akaike information criterion (AIC), and modified AIC (AICc) [57] [58]. The common basis of these criteria is the parcimony principle which states that the most acceptable explanation of a phenomenon is the simplest one, in our case the one involving the least number of free parameters. This means that there is a trade-off between fitting accuracy and the number of free parameters. As discussed below, all these criteria penalize a larger number of parameters.

To determine which of the 3 different motion modes (Brownian motion, confined motion in a 2^{nd}- order and confined motion in a 4^{th}-order potential) best describes the trajectories of the membrane receptors, firstly, the characteristic parameters are inferred by applying Bayesian inference. For each motion mode, the posterior probability (for details see section 1.3.2) $P(Q|T)$ is calculated and its maximum is found. This maximum of the *a posteriori* distribution is defined as the MAP (Maximum a Posteriori) estimator. Using this MAP estimator, the relevant criteria (BIC, AIC and AICc) are calculated by the equations below and a decision is made based on which model minimizes the value of each criterion.

The BIC was developed by Gideon E. Schwarz. It is defined in Equation 1.15 and the model with the lowest BIC value is the preferred model [57]:

$$BIC = -2 \cdot \ln(L) + k \cdot \ln(N) \tag{1.15}$$

where L is the MAP estimator in this case, N is the number of data points, and k represents the number of degrees of freedom in the model.

The AIC is an estimator of the relative quality of statistical models for a given set of data [58]. We can then choose the candidate model that minimizes the information loss and yields the minimum AIC value. The formula for AIC is as follows:

$$AIC = -2 \cdot \ln(L) + 2k. \tag{1.16}$$

If the sample size is small, then some correction is often necessary to address potential overfitting. The AICc criterion is the same as the AIC criterion with a correction for small sample sizes N and is given by:

$$AICc = AIC + \frac{2k(k+1)}{N-k-1}. \tag{1.17}$$

Note that all these three criteria include a positive term that penalizes large numbers of degrees of freedom k.

In the work of Türkcan and Masson, they used simulated trajectories to determine which of these three information criteria works best to choose the preferred model among Brownian motion confined motion in a 2nd-order, and confined motion in a 4th-order potential [55]. For each mode of motion, they simulated 300 trajectories. For each trajectory, they studied the dependence on trajectory length (N), diffusion coefficient (D), acquisition time (t_{acq}), and potential spring constant (k_r) specifically for a 2nd-order confinement potential and potential strength (α), specifically for a 4th-order potential, where α is defined as $\alpha = \sqrt{\alpha_X^2 + \alpha_Y^2}$ for a 4th-order potential $V(x, y) = \alpha_X x^4 + \alpha_Y y^4$. The range of parameters they explored matches most of the biological media properties.

The percentage of correct decisions for each criterion is shown in Fig. 1.6 for these different conditions. For all parameters examined (number of data points (Fig. 1.6 A), diffusion coefficient (Fig. 1.6 B), and acquisition time (Fig. 1.6 C), BIC performs better then AIC and AICc both in range and accuracy. For conditions close to the experimental ones, typically $D = 0.1\ \mu m^2/s$, t_{acq}=50 ms, and N ~1000 points, BIC reliably attributed the correct model to 100% of the trajectories.

This percentage is significantly higher than for the AIC and AICc criteria, which correctly classify only around 50% of the trajectories [56]. Also, 20 data points are sufficient for the BIC to correctly identify the type of motion (Fig. 1.3 A). These results confirm that the BIC is the best criterion for distinguishing free Brownian motion.

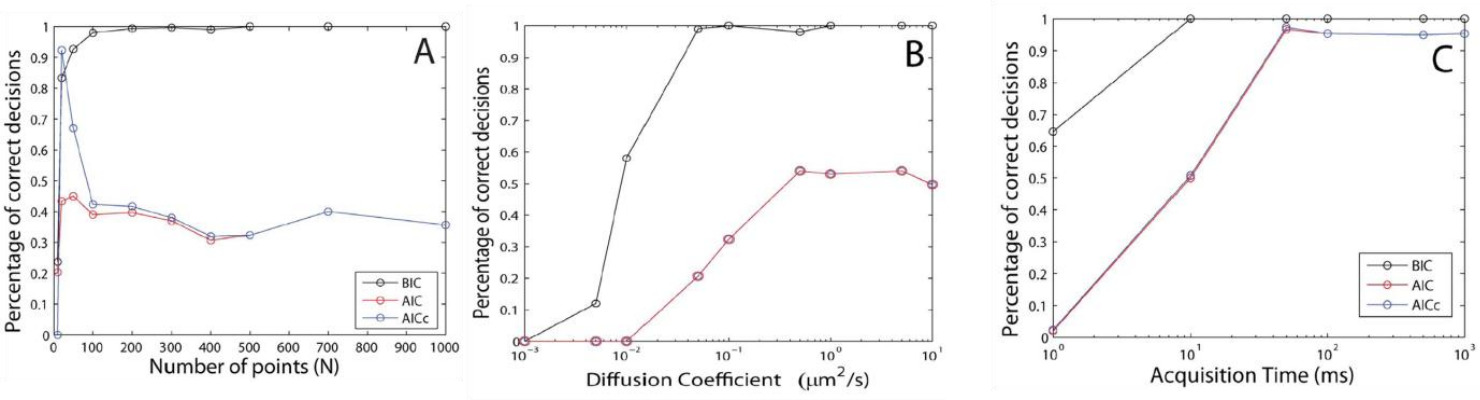

Figure 1.6: For 300 simulated free Brownian motion trajectories for each set of conditions, percentage of correct decisions for each information criterion BIC (black), AIC (blue) and AICc (red) versus the length of the trajectory (A), the input diffusion coefficient (B), and the acquisition time (C).

(Simulation parameters: D_{input}=0.1 μm²/s, t_{acq}=50 ms, N=500 points. The simulations also include a localization noise B_r of 30 nm close to the experimental one.) Figure extracted from [55].

In the same way, sets of 300 trajectories of Brownian motion inside a 2nd-order potential $V(x,y) = \frac{1}{2}k_X x^2 + \frac{1}{2}k_Y y^2$, with $k_r = \sqrt{{k_X}^2 + {k_Y}^2}$, where k_r is spring constant were calculated for various conditions.

The percentages of correct decisions for each criterion under these conditions are shown in Fig. 1.7. For trajectory lengths of around 1000 points (Fig. 1.7A), D =0.1 μm2/s (Fig. 1.7B), and t_{acq}=50 ms (Fig.1.7C), BIC performs slightly better than AIC and AICc. When the spring constant is varied (Fig.1.7D), BIC performs better except when k is smaller than 0.5 pN/μm.

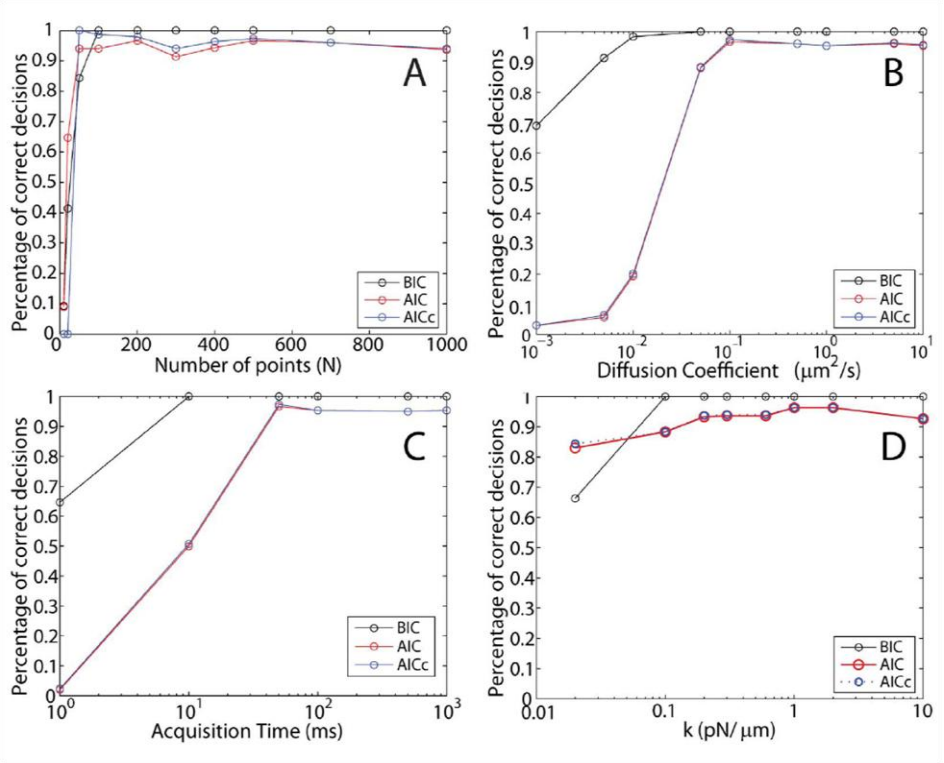

Figure 1.7: For simulated trajectories of Brownian motion in a 2nd-order confinement potential, percentage of correct decisions for each information criterion versus the length of the trajectory (A), the input diffusion coefficient (B), the acquisition time (C), and the input spring constant (D).

BIC (black), AIC (blue) and AICc (red). Simulated parameters: D_{input}=0:1 μm²/s, t_{acq}=50 ms, N=500 points, B_r=30 nm, k=0.3 pN/μm). Figure extracted from [55].

On the other hand, for motion inside a 4th-order potential $V(x,y) = \alpha_X x^4 + \alpha_Y y^4$, with potential strength $\alpha = \sqrt{\alpha_X x^2 + \alpha_Y y^2}$, as shown in Fig. 1.8, for a trajectory length (Fig. 1.8A) around 1000, D=0.1 μm²/s (Fig. 1.5 B), t_{acq}=50 ms (Fig. 1.8 C), AIC and AICc exhibit success rates between 70% and 100%. When the potential strength is varied (Fig. 1.8D), AIC and AICc perform equally well. In contrast, the BIC criterion performs badly and systematically classifies all confined trajectories as due to a second-order potential.

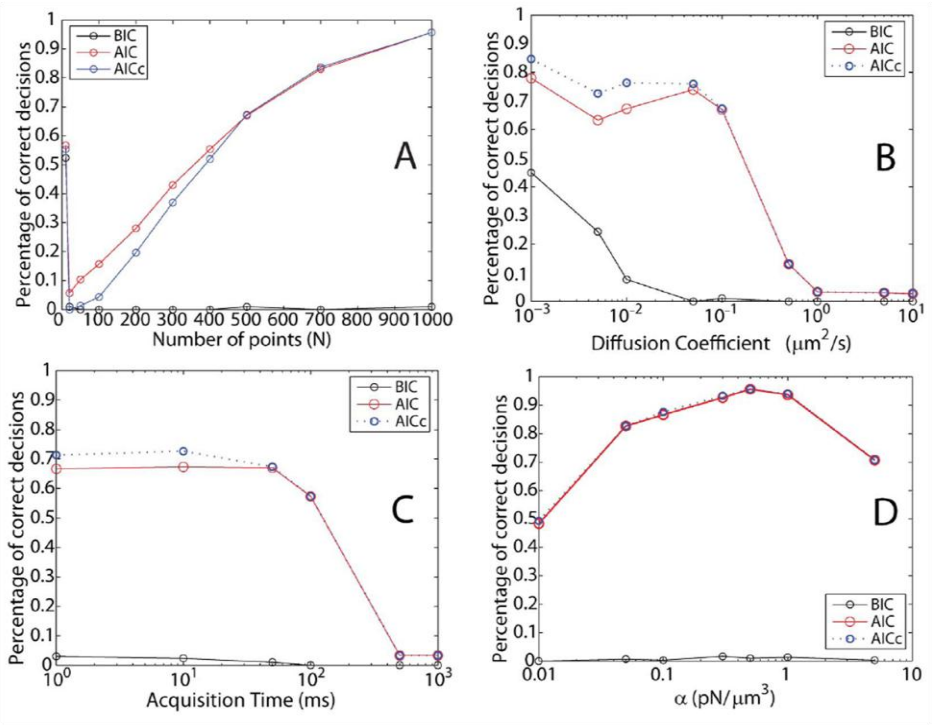

Figure 1.8: For simulated trajectories of Brownian motion in a 4th-order confinement potential, percentage of correct decisions for each information criterion versus the length of the trajectory (A), the input diffusion coefficient (B), the acquisition time (C), and the input potential strength α (D).

BIC (black), AIC (blue) and AICc (red). (Simulated parameters: D_{input}=0.1 μm^2/s, t_{acq}=50 ms, N=500 points, B_r=30 nm, α=0.5 pN/μm^3). Figure extracted from [55]**.**

Based on the results above, Türkcan and Masson concluded that BIC can distinguish between free Brownian motion and confined motion, but fails to distinguish between trajectories inside a 2nd-and 4th-order confinement potential. AIC and AICc can distinguish between 2nd-and 4th-order potential in a wide parameter range. Based on this conclusion, a decision tree was built for

trajectory classification as shown in Fig. 1.9. BIC is only used in the first step to distinguish free Brownian motion and confined motion, while AIC and AICc are used in the second step to distinguish between the two different types of confined motion (2^{nd}- and 4^{th}-order confinement potential).

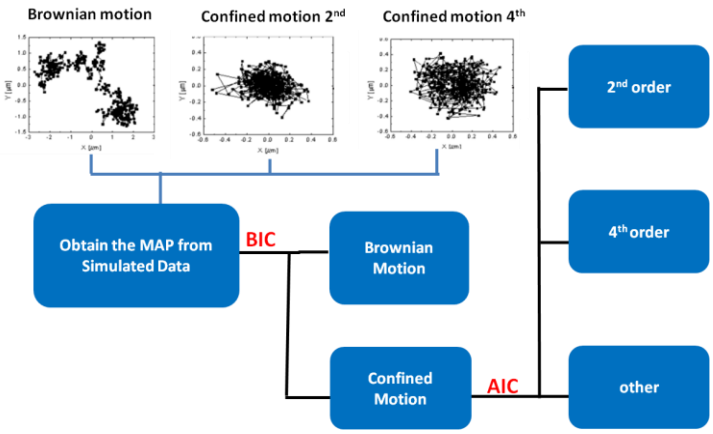

Figure 1.9: Decision tree schematic. Figure extracted from [55]**.**

1.4.2 Data clustering analysis

Data clustering analysis is a statistical classification technique for discovering the natural grouping of a set of patterns, points or objects [59]. It can reduce a high dimensional data set down to two dimensions and divide data in different groups (clusters) by applying specific clustering algorithms. Depending on the individual data set and the intended use of the results and due to the difficulty of definition of the notion of cluster, clustering analysis may include many different clustering algorithms [60]. As a typical example of clustering algorithms, the k-means algorithm can be used to partition data from a data set into a given number of clusters in which each data point belongs to the cluster with the centroid nearest to the data point in question [61].

In reference [35], for classifying the motion modes of membrane receptors, Richly, Alexandrou, and Masson applied a clustering algorithm to compare both confinement potentials and diffusion coefficients of simulated and experimental trajectories. This clustering algorithm is described below.

Trajectory segmentation

In section 1.3.2, we discussed splitting the trajectories into equal-sized square subdomains where F and D are considered constant. An optimized way to determine subdomains of different sizes was used in [35] presenting the advantage that each subdomain is chosen in such a way that all subdomains contain a similar number of trajectory points. Firstly, the trajectories were also analyzed by the k-means clustering algorithm which minimizes the expression:

$$\sum_{i}^{k} \sum_{x \in S_i} \|x - \mu_i\|^2 \tag{1.18}$$

where x are the data points, μ_i is the centroid of cluster S_i and k the number of clusters. The algorithm is an optimization loop which attributes each data point in a receptor trajectory to the nearest cluster (by minimizing the distance to the different cluster centroids) and obtains 75 to 100 clusters. These cluster centroids are then shown by a Voronoi diagram (blue lines in Fig. 1.7A):

$$R_k = \left\{ x \in X \middle| D(x, P_k) \leq D\left(x, P_j\right) \qquad for\ all\ j \neq k \right\} \tag{1.19}$$

where X is a metric space with distance function D and R_k is a Voronoi cell with centroid P_k. Each Voronoi cell R_k consists of a group of data whose distance to P_k is smaller or equal to its distance to any other cluster centroid P_j.

Bayesian inference analysis

Then, a Bayesian inference algorithm (see section 1.3.2) is applied to infer the confinement potential and diffusion coefficient values for a given trajectory in each Voronoi tessellation cell (here, each Voronoi cell has a independent D value). The confinement potential and diffusion

coefficient values are normalized and are projected to a 41×41 rectangular mesh which partitions the Voronoi tessellation. Each cell of the 41×41 rectangular mesh adopts the potential or diffusion coefficient values of the corresponding overlapping Voronoi cell, as shown in Fig. 1.10A and B for the confinement potential (in color-code). An in-house MATLAB algorithm is used for this step. The aim of this step is to project all the confinement potential and diffusion coefficient values obtained for the various trajectories to a mesh with identical number of cells so that the data can subsequently be compared to each other. Note that the mesh size is chosen to be approximately half of the smallest size of the Voronoi tessellation of the potential which ensures that the size is small enough to preserve the heterogeneity of the data, yet not too small to oversample the potential.

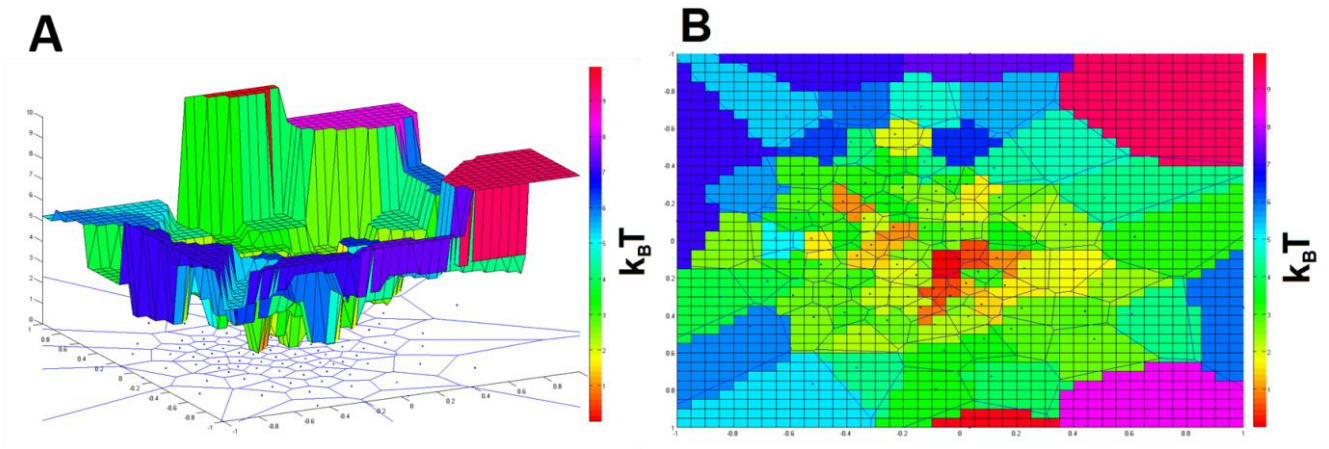

Figure 1.10: The inferred confinement potential energy (in color-code) obtained using Voronoi tessellation (see blue lines in A and B) is projected onto a 2D 1681 (41x41)-dimensional data set of potential energy values (B). The 41x41 mesh units adopt the corresponding potential energy values of each overlapping Voronoi cell and are shown in the same color as the corresponding Voronoi cell (B). Figure extracted from [56]**.**

Thirdly, the 2D 41×41 meshes of values shown in Fig. 1.10B are transformed into a single array by concatenating each line of mesh values side by side. For each trajectory, we thus obtain a 1D 1681-dimension data set for the confinement potential and 1681-dimension data set for the diffusion coefficient.

Clustering

Lastly, the 1681-dimensional data sets obtained for the different trajectories are reduced to 15-dimensional data sets by using a preliminary principal component analysis (PCA) [62]. By running a t-distributed stochastic neighbor embedding (t-SNE) algorithm [63] on simulated and experimental data, as shown in Fig. 1.11A , the confinement potential data were projected on a 2-dimensional graph while retaining the maximum possible heterogeneity. The distance between a point and all the other points on this 2D graph reflects the similarities between this point and the others (quantified by a Student's t-distribution) [35].

Simulated trajectories

This was done both for experimental trajectories and for simulated trajectories obtained using two types of potential: a 2nd-order potential and a potential that is flat in the center and increases exponentially close to the border of the confinement domain. This potential will be called "*exponential*" in the following and is described by:

$$V(r) = \begin{cases} \dfrac{A_{exp}}{e-1}\left(e^{\frac{r-f\cdot r_0}{r_0-f\cdot r_0}}-1\right), & if\ r \geq f\cdot r_0 \\ 0, & if\ r < f\cdot r_0 \end{cases} \qquad (1.20)$$

where A_{exp} represents the height of the potential at $r = r_0$ and is set to 4 $k_B T$ and f is the fraction of r_0 at which the potential changes from flat to exponential and was set to 1/3.

A clear separation in two groups was observed between points calculated from simulated trajectories with 2nd-order confinement potential and those calculated with an 'exponential' confinement potential. Indeed 89% and 91% of the simulated trajectory data points are found in the first group and in the second group, respectively. This shows that the clustering algorithm can efficiently separate 2nd- and "*exponential*" confinement potential data.

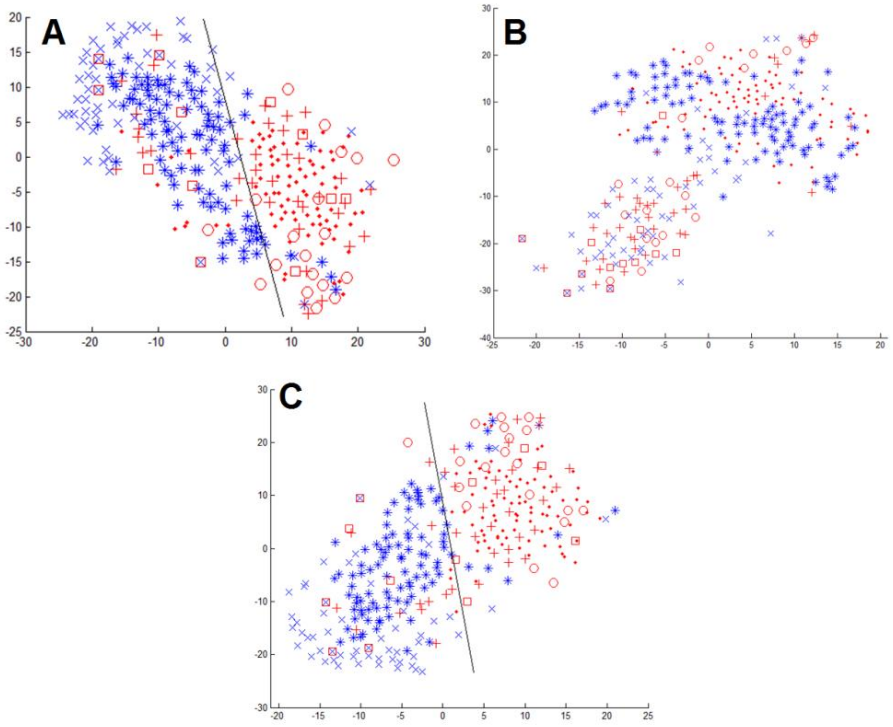

Figure 1.11: Cluster plot of simulated and experimental data. Simulated 2nd order (. , N=83), CPεTR (+, N=40), CSαTR(o, N=40),hopping CPεTR(□, N=12), Simulated 2nd order (* , N=100), TfR (× , N=65). Cluster plot of the confinement potential data (A), of the diffusion coefficient data (B), and of the combination of confinement potential and diffusion coefficient data (C). Figure extracted from [56]**.**

Results

In this work, three cell membrane receptors were observed: the receptor of the pore-forming ε-toxin produced by *Clostridium perfingens* (CPεTR), the receptor of the pore forming α-toxin (CSαTR) produced by *Clostridium speticum* types B and D, and transferrin receptor (see chapter 3). Note that even though the precise membrane receptor of CPεT has not been identified, previous studies suggest that accumulation of CPεTR in membrane raft domain [7], [64], [65]. Its ligand, CPεT, can induce pore formation after binding on the membrane of host cell. With high lethal toxicity, this toxin causes several of disease including braxy and neurological alterations[65], which further attracted research attention.

Experimental data which are expected to show confinement in a 2^{nd}-order potential based on the results of Ref. [7] were found to be localized in the first group together with the simulated 2^{nd}-order potential data (see Fig. 1.11A; 70% of CPεTR points, 90% of CSαTR points, and 42% of CPεTR points showing hopping – note that CPεTR are seen to rarely hop from one confining domain to an adjacent one [56]; the CPεTR trajectories showing hopping were analyzed separately by splitting them in portions confined in a single domain), whereas 94% of the TfR points were found in the second group colocalized with the 'exponential' potential simulated data. A straight line can then be drawn simply by eye. Fig. 1.11B presents the cluster plots for the diffusion coefficient, which show no separation in two data groups. A combination of confinement potential and diffusion coefficient data (*i.e.* clustering analysis of 3362-dimensional data sets) for all trajectories is plotted in Fig. 1.11C, which again shows a clear separation between a 2^{nd}-order confinement potential group (96% of the simulated 2^{nd}-order data, 70% of the experimental CPεTR data, 95% of the experimental CSαTR data, and 50% of the CPεTR data showing hopping were found in this group) and exponential confinement potential group (91% of the simulated 'exponential' confinement potential data and 92% of the TfR data were localized in this group). These results are only slightly different from those obtained with clustering of the confinement potential data only. This means that the receptor trajectories mainly differ in the confinement potential they experience and not in their diffusion coefficient.

In terms of similarity, the receptor trajectories confined by membrane raft microdomains (CPεT, CSαT receptors) are grouped together with simulated data obtained for Brownian motion in a 2^{nd}- order potential, whereas receptor trajectories located outside rafts and sterically confined by the actin cytoskeleton, as postulated by the picket-and-fence model (transferrin receptor) are grouped together with simulated data for motion in a 'exponential' confinement potential. These results are in agreement with the conclusions obtained based on the Bayesian inference decision tree (BIDT) approach [55] (see section 3.2.3). A description of these clustering methods is presented below.

These clustering algorithm results confirm that the confinement potentials can be used to classify the receptor motions as evolving in 2^{nd}-order or 'exponential' confinement potentials. Furthermore, this clustering algorithm may provide a way to distinguish between receptor

motions of more than two kinds by grouping them based on their similarities. It is thus a powerful tool to provide a universal classification of receptors based on the type of their confinement.

1.5 Summary

In this chapter, we introduced single-molecule imaging and tracking techniques on the cell membrane by labeling with luminescent nanoparticles $Y_{0.6}Eu_{0.4}VO_4$. For each single label, pixelated images of the Airy diffraction pattern are first acquired by the camera and then fitted with a Gaussian to obtain the precise molecule localization from the function's maximum. Once the data processing of single particles is performed and the trajectories are obtained from the successive label positions in the series of images, analysis approaches can then be applied to obtain quantitative information on cellular parameters.

The most commonly used analysis method is based on the Mean Square Displacement (MSD) as a function of time, which describes the extent of space explored by a molecule as a function of time lag t, but throws away a lot of information when calculating the average square displacement. For confined motion, using a recent technique based on Bayesian inference, the parameters of the unknown potential leading to confinement can be extracted.

Moreover, the shape of the confinement potential provides ways to classify the different motion types of single receptors on the cell membrane as shown in section 1.4. For trajectory classification, the Bayesian inference decision-tree approach is based on a set of information criteria to distinguish between different types of motion. In a first step, the criterion BIC is used to distinguish between free Brownian motion and confined motion, while AIC and AICc criteria are used in a second step to distinguish between two different types of confined motion in a 2^{nd}- or in a 4^{th}-order polynomial confinement potential. Another trajectory classification method, data clustering, is based on a clustering algorithm to classify both confinement potentials and diffusion coefficient maps of simulated and experimental trajectories into two separated groups. The clustering approach is quite powerful because it can provide indications that two receptors types are confined in the same type of nanodomain without requiring any additional experiments with pharmacological treatments like raft-disrupting or cytoskeleton-depolymerizing molecules.

On the single molecule level, $Y_{0.6}Eu_{0.4}VO_4$-nanoparticle labeling not only provides a luminescent signal to track receptor motion in the cell membrane, but can also be exploited to amplify the force exerted on a molecule through a liquid flow. This feature can be used to understand specific interactions between molecules, as will be discussed in Chapter 2, and the mechanisms governing membrane-cytoskeleton interactions, as will be shown in Chapter 4.

Chapter 2
Measuring Dissociation Rate Constant by Applying a Flow Force on a Single Nanoparticle

2.1 Dissociation Constant of Biomolecules

In biochemistry, dissociation is a general process in which a biomolecular complex separates into its constituent molecules usually in a reversible manner. The equilibrium dissociation constant (K_D) is a characteristic parameter of dissociation, which measures the dissociation propensity of the complex. In this section, we will introduce the definition of the dissociation constant and techniques for measuring the dissociation constant of biomolecular complexes.

2.1.1 Definition of the Dissociation Constant between two Biomolecules

Biological effects result from a series of specific interactions between biomolecules, such as enzyme-substrate, antigen-antibody and ligand-receptor, which are involved in most of cell functions and metabolism. In all these cases, as well as in drug targeting, selective binding is the basis for specificity. The equilibrium dissociation constant (K_D) is a primary parameter to evaluate the binding properties. It is particularly important for the characterization of the activity of therapeutic molecules. Indeed, the smaller the K_D, the higher the drug activity, the smaller the doses that have to be injected, and the smaller the expected side effects.

A simple one-step mechanism for the formation of a biomolecular complex AB reads:

$$A + B \underset{k_{off}}{\overset{k_{on}}{\rightleftharpoons}} AB \tag{2.1}$$

The corresponding dissociation constant can be defined as:

$$K_D = \frac{[A] \cdot [B]}{[AB]} = \frac{k_{off}}{k_{on}} \tag{2.2}$$

where [A], [B]and [AB] represent molar concentrations of the biomolecules A, B, and complex AB at equilibrium. For a given receptor, the equilibrium constant K_D can also be calculated from the ratio of the dissociation off-rate (k_{off}) and association on-rate (k_{on}).

2.1.2 Approaches for Dissociation Constant Determination

To fully determine the interaction between two molecules, we need techniques that can measure both k_{on} and k_{off} from which K_D can be calculated. However, most of the available techniques only yield K_D. Various analytical techniques have been employed for measuring the K_D value of biomolecular interactions e.g. including isothermal titration calorimetry (ITC), fluorescence anisotropy, and surface plasmon resonance (SPR). The latter has the additional advantage of yielding also the dissociation off-rate (k_{off}) and association on-rate (k_{on}). In the following, a brief introduction of each analytical method for determining the dissociation constant K_D and/or k_{on} and k_{off} is presented.

Isothermal titration calorimetry (ITC) is a widely used label-free measurement of binding affinity and thermodynamics of bimolecular interactions in the last 30 years [66], [67]. It is based on the direct measurement of the amount of heat change associated with a bimolecular binding or dissociation event. This technique is capable of determining the dissociation constant K_D but not the on- and off-rates k_{on} and k_{off}. In addition to K_D, measuring heat transfer during binding is capable of determing reaction stoichiometry (n), enthalpy (ΔH), and entropy (ΔS) contributions, which provide a standard tool for characterizing the mechanisms underlying molecular interactions.

Fluorescence anisotropy measurement is based on the principle that, upon polarized excitation, the light emitted by a fluorescent probe has unequal intensities along different polarization axes [3],[4]. This anisotropy depends on how fast the fluorescent probe rotates. The application of fluorescence anisotropy is based on the fact that a molecule rotates faster than its larger complexes. The larger complexes tumble slower and retain higher emission polarization

anisotropy, while the smaller molecules depolarize the emission more effectively. This approach can be used to measure the kinetics of biomolecular interactions by detecting changes in the rotational time of the molecules.

The principle of this measurement is illustrated in Fig. 2.1. When the fluorescent sample is excited by a polarized light in a vertical orientation, the emission of excited fluorescent probes will be those oriented with a particular range of angles to the applied polarization. The emission passes through a two-orientation-analyzer and the intensities parallel to the direction of the polarized excitation, $I_{\parallel}$, and perpendicular to the excitation, $I_{\perp}$, are measured by a detection system. Then, the obtained intensity values can be used to calculate the anisotropy defined as [69]:

$$r = \frac{I_{\parallel} - I_{\perp}}{I_{\parallel} + 2I_{\perp}} \tag{2.3}$$

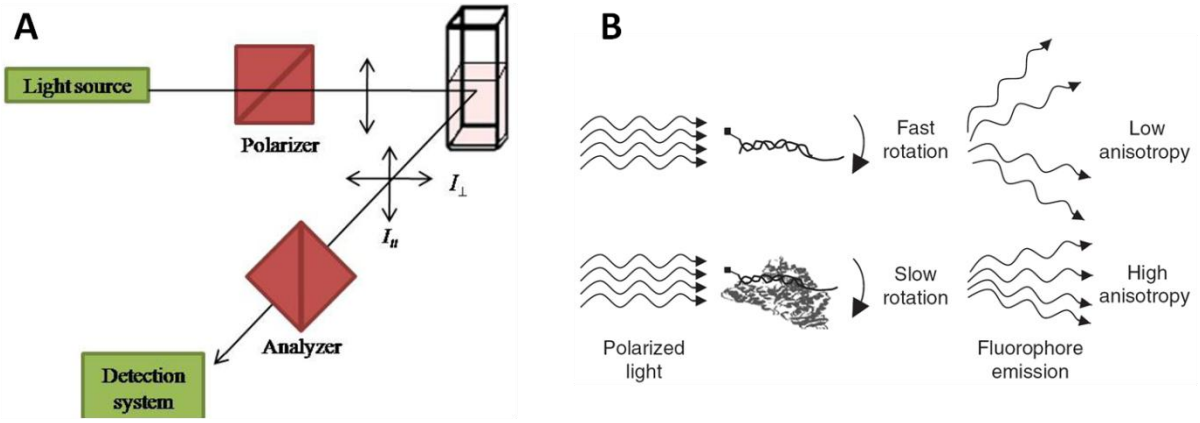

Figure 2.2 : **A schematic diagram for measurement of fluorescence anisotropy (A) (Figure extracted from ref.** [70]**), and (B) A scheme of the effect of rotational diffusion rate on the anisotropy of emitted light from fluorescently labeled DNA and DNA-protein complex (Figure extracted from ref.** [71]**).**

An example of this technique is presented in the following: A rotation comparison between free DNA and DNA-protein complex is shown in Fig. 2.1B [71]. The DNA-binding proteins titrate into a solution of fluorescently labeled DNA. The complex of DNA-fluorescent probes and the protein

will lead to a large relative change in rotational diffusion and hence anisotropy. Then, a K_D value can be extracted from a plot of anisotropy versus protein concentration.

As a solution-based real-time technique, fluorescence anisotropy has been widely used to explore biomolecular structure and interactions. However, since one of the two interacting molecules must be fluorescent, it thus has to be modified by the addition of a fluorophore which may modify the interaction conditions. Moreover, unless pulsed excitation is used, this technique can measure the dissociation constant K_D but not the on- and off-rates k_{on} and k_{off}.

Surface plasmon resonance (SPR)

Surface plasmon resonance (SPR) is a specific technique for the investigation of biomolecular interactions, which has been applied for biomolecular specificity and binding kinetics in recent years. Its advantage compared to other techniques, such as isothermal titration calorimetry is that it can measure independently $\mathrm{k_{on}}$ and $\mathrm{k_{off}}$. SPR technology is an optical method based on the fact that light incident at a specific angle can resonate with the delocalized surface electron oscillations of gold or silver surfaces, called surface plasmons, thus reducing the reflected light intensity (see Fig. 2.2) [72], [73]. The ligand is bound to a thin metallic surface and the analyte flows by. Upon analyte binding, the refractive index of the medium in contact with the metallic surface changes and this leads to a change of the surface plasmon resonance value and to a change in the reflectivity characteristics.

The most common optical configuration is shown in Fig. 2.2 A [74]. An incoming polarized light propagates in the glass prism (with a higher refractive index medium than the water solution) and meets the interface with a water solution (with a lower refractive index medium). At a critical incidence angle, the light beam can be maximally reflected at the interface and leaks an evanescent field into the solution, this phenomenon being called total internal reflection (TIR). This evanescent wave has the same wavelength as the incident light, and its amplitude decays exponentially as a function of the distance from the prism-solution interface and its energy is dissipated by heat. When the prism-solution interface is coated by a suitable conducting gold layer with a certain thickness (usually 50-100 nm), the evanescent wave can pass though the gold film, transfer the energy to the free electrons in the gold layer, and finally be converted

into surface plasmons. At a certain incident wavelength and angle, where the momentum of plasmons is equal to momentum of the incident light, a resonance occurs.

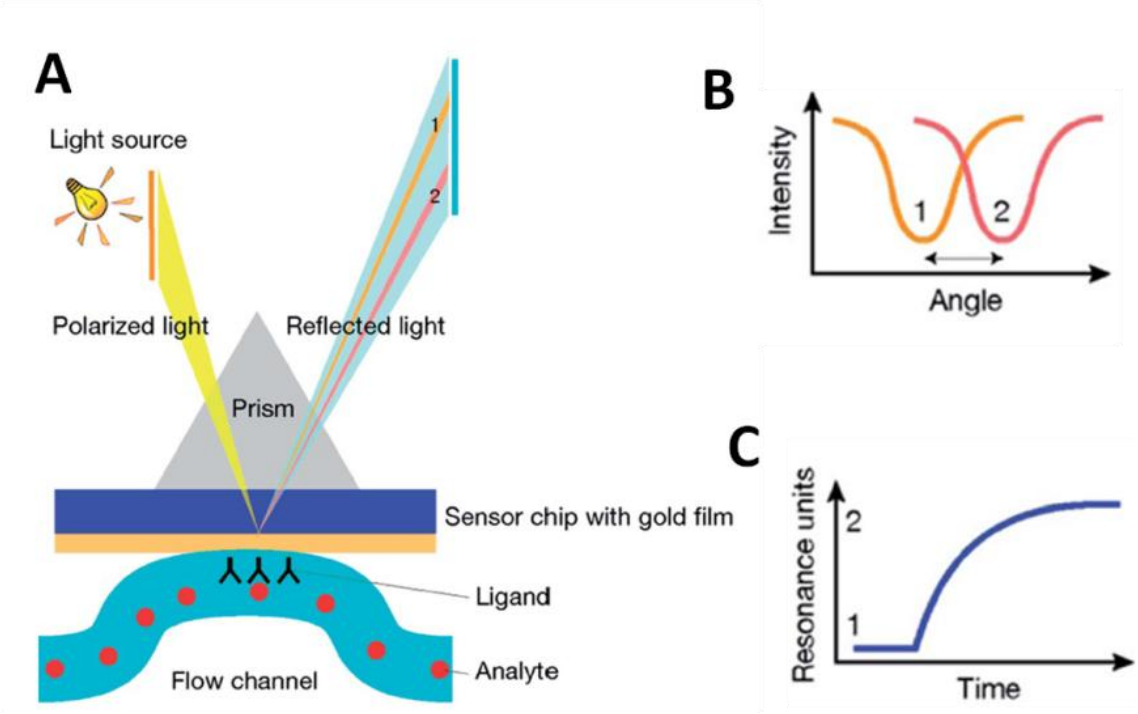

Figure 2.2**: Scheme of the surface plasmon resonance technique. (A) The Kretschmann geometry method for detecting binding events. (B) The resonance in the reflected intensity curve as a function of incident angle changes before and after the binding events. (C) The angle changes are recorded in resonance units (RU) as a function of time. This figure is extracted from Ref.** [74]**.**

The gold layer is coated with ligand molecules and a flow chamber is used to bring analyte molecules in interaction with the surface-coated ligand molecules (Fig. 2.2). When a binding or a dissociation event occurs at the metal surface, the momentum of the plasmons is changed. Indeed, the plasmon momentum depends on the refractive index of the solution. Therefore, the resonance angle changes (Fig. 2.2B) in a manner proportional to the number of ligand-analyte complexes formed [75]. At last, the reflected light intensity as a function of angle shows a resonance that shifts as a function of time as association or dissociation occurs and can be read out by a detector for further analysis (Fig.2.2C) [2],[5].

Figure 2.3 shows a kinetic curve scheme in four phases.

1) The ligands are immobilized in an array format on the sensor surface in a flow chamber.
2) When the analyte solution enters the flow chamber, ligand-analyte interaction occurs. This reaction can be assumed to follow a pseudo first-order kinetics [77], and the concentration changes of the ligand-analyte complexes can be described by the following equation:

$$\frac{d[AB]}{dt} = k_{on}[A][B] - k_{off}[AB] \tag{2.4}$$

where $[A]$, $[B]$ and $[AB]$ represent molar concentrations of the analyte A, ligand B and complex AB at equilibrium. k_{on} is the association rate and k_{off} is the dissociation rate. Since the change of SPR resonance angle R is proportional to the concentration change, we have $R = p[AB]$, where p is the proportionality constant.

Since the analyte A is constantly replenished by the flow and thus is maintained constant, its concentration $[A]$ can be assumed to be equal to a constant c. Then,

$$\frac{dR}{dt} = p \cdot k_{on} \cdot c \cdot [B] - p \cdot k_{off}[AB] \tag{2.5}$$

When a free analyte is captured by a ligand, a complex AB is produced. The maximum SPR angle change R_{max} is proportional to the total ligand concentration consisting of free and bound B molecules: $R_{max} = p([B] + [AB])$. We then can consider that: $R_{max} - R = p[B]$

$$\frac{dR}{dt} = (R_{max} - R) \cdot k_{on} \cdot c - R \cdot k_{off} \tag{2.6}$$

We then consider $R_{max} \cdot k_{on} \cdot c$ as a constant A_o, and $k_{on} \cdot c + k_{off}$ as a constant k_s.

The above equation can then be solved to yield:

$$R(t) = \frac{A_o}{k_s}(1 - e^{-k_s t}) \tag{2.7}$$

We can find k_s by fitting the experimental data to an exponential, and then k_{on} value can be found from the slope of the straight line obtained by plotting k_s against [A] [78].

3) When the flow containing analytes continues for a certain time, the bound complexes reach an equilibrium state. The amount of complexes forming is equal to the amount of analytes detaching. The binding rate and the SPR angle change dR/dt is zero.
4) When the flow containing analytes is replaced by flow of a pure solution, the complexes will start to dissociate. Since [A] is now equal to zero, the ligand-analyte complex dissociation can be described as follows:

$$\frac{dR}{dt} = -k_{off} \cdot R \tag{2.8}$$

At an arbitrary starting time of the dissociation, the corresponding SPR angle change is R_o, and the solution of the above equation reads:

$$R(t) = R_o \cdot e^{-k_{off}(t-t_o)} \tag{2.9}$$

By fitting the experimental data to this equation, we can extract the k_{off} value. Then, the dissociation constant K_D can be calculated as $K_D = \frac{k_{off}}{k_{on}}$ [6].

As a label-free, real-time and highly sensitive investigation tool, SPR has been widely used to study the interaction between membrane proteins and ligands and define the association and dissociation kinetics with both high- and low-affinity. However, one must keep in mind that, since one of the two molecules is immobilized on the surface, this might change the interaction process. Moreover, many drug-target complexes show very high affinities and the dissociation rate is very slow; it therefore takes a long time before the analyte spontaneously detaches from the ligand.

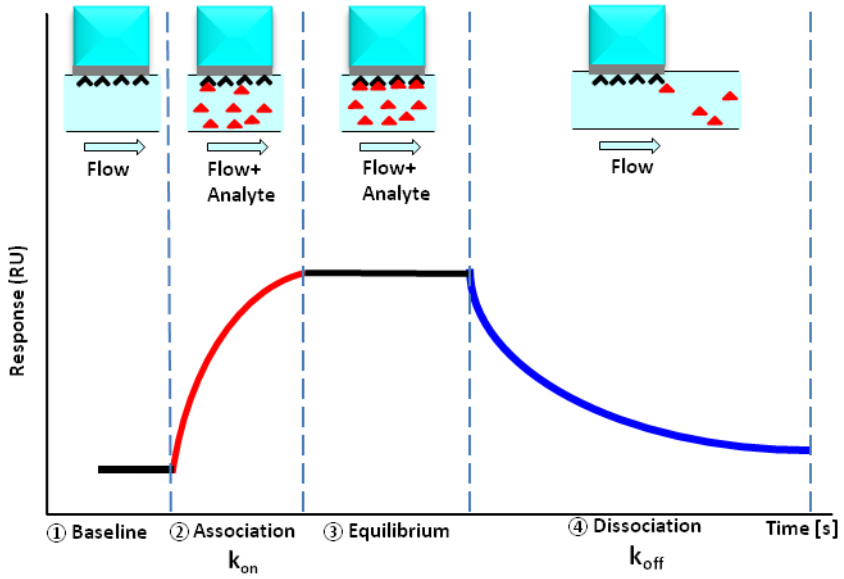

Figure 2.3: Scheme of analyte-ligand association and dissociation generated by the SPR system.

2.1.3 Single-Molecule Approach

An alternative approach to the above ensemble approaches for the observation of stochastic association and dissociation kinetics is to detect binding and dissociation at the single molecule level: one of the two molecules is immobilized at a glass surface with a fluorescent label and the second fluorescently labeled molecule is added to the solution. By using a total internal reflection configuration, only the fluorescent molecules binding to the glass surface can be detected. The unbound fluorescent molecules are not excited by the evanescent electric field.

Previous work in our group showed that the single-molecule approach can be applied as a convenient tool to determine independently k_{on} and k_{off} values[79]. As explained below, k_{on} can be obtained from the total number of detected binding events as a function of time and k_{off} can be determined from the statistics of fluorophore disappearance due to dissociation events, after the contribution of photobleaching is corrected for. As shown in Fig. 2.4a, a single-stranded DNA (ssDNA) is immobilized on a glass surface by using a biotin-streptavidin linker,

then two partially complementary ssDNA strands, one of them labeled with a fluorescent dye Alexa-488, are injected into the solution and specifically bind to the immobilized DNA stranded forming a double strand dsDNA with a so-called flap (see Fig. 2.4a). The positions of the dsDNA molecules can be determined by exciting Alexa-488. After recording the molecule positions, this fluorescent labeling is photobleached. Then, the protein-binding endonuclease NucS labeled with Alexa-488 is added to the solution. In these experimental conditions, single NucS and dsDNA fragments can then be localized with a typical 3 nm accuracy, as explained in Chapter 1. The binding events between flap-containing dsDNA and NucS can thus be determined when the fluorophore-labeled NucS are colocalized, *i.e.* are closer than a few nanometers, with dsDNA, whereas fluorescent molecules appearing away from locations of dsDNA are due to non-specific binding events. A typical set of recorded images is shown in Fig. 2.4b.

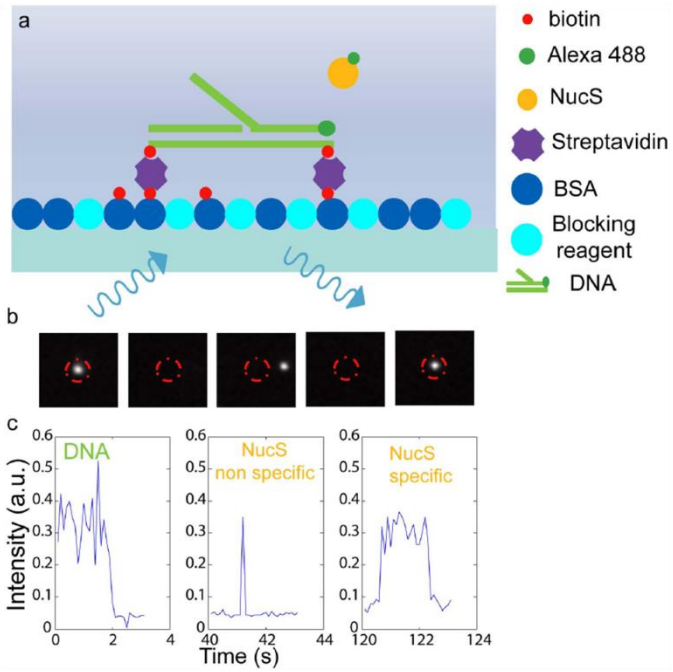

Figure 2.4: Single-molecule approach for measuring association rate k_{on} of NucS with DNA. a) Scheme of surface treatment and binding events. b) A set of experimental images (from left to right): dsDNA detection (1), photobleaching of the dsDNA fluorophore (2), addition of NucS, non-specific binding (3), no binding (4), and specific binding of NucS to dsDNA (5). c) Signal obtained during the experimental acquisition (from left to right):

dsDNA immobilization on the surface and subsequent photobleaching of its fluorophore (1), non-specific binding (2), and specific binding of NucS to dsDNA. [79]

The reaction above can be described as:

$$NucS + DNA \xrightarrow{k_{on}} NucS - DNA \tag{2.10}$$

The association rate constant k_{on} can be determined by:

$$\frac{d[NucS - DNA]}{dt} = k_{on}[NucS][DNA] \tag{2.11}$$

Because of the relatively low number of $NucS - DNA$ complexes forming compared to the total molecule numbers of $NucS$ and DNA, the concentration of unbound molecules, $[NucS]$ and $[DNA]$, can be considered constant. After multiplying each side by the total solution volume, we obtain:

$$\frac{dN_{NucS-DNA}}{dt} = k_{on}[NucS] \cdot N_{DNA} = v_a \tag{2.12}$$

where $N_{NucS-DNA}$ represents the number of $NucS - DNA$ complexe, $N_{DNA}$is the number of immobilized dsDNA on the glass surface, and v_a is the speed of complex formation. v_a can be extracted from the slope of the total number of detected binding events as a function of time as shown in Fig. 2.5, where the binding events can be recorded and counted one by one. The fact that the total number of binding events as a function of time is linear confirms this analysis. We can thus determine the v_a value from the slope of the curve in Fig. 2.5 and, since $[NucS]$ and N_{DNA} are known, k_{on} can be extracted.

By observing the evolution of the number of interaction events with time, this single molecule approach can directly detect the k_{on} value. Compared to the other commonly used methods of association kinetics determination, like SPR, it does not require varying the concentration of one of the two molecules to extract k_{on}. A variant of this experimental process may employ a two-color labeling, one color for each molecule, instead of labeling both molecules with the same

fluorophore (Alexa-488 is this case), which avoids the photobleaching step of the first fluorophore but requires two-color imaging.

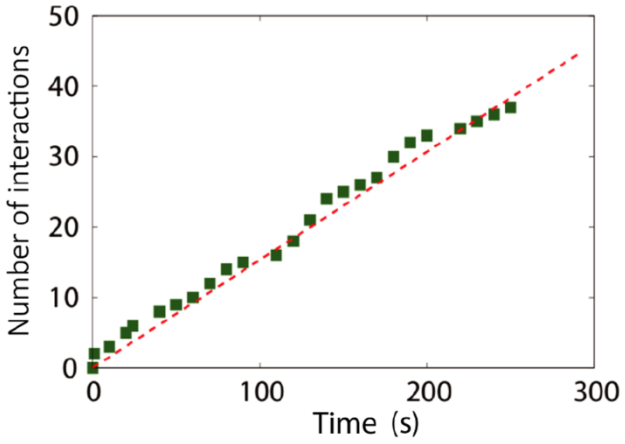

Figure 2.5: Numbers of detected binding events as a function of time. v_a can be extracted from the slope. Figure extracted from [79].

This approach can also determine the dissociation rate constant k_{off} from the exponential fit of the dissociation probability distribution as a function of time (for details see ref. [79]). However, one may have to correct for the photobleaching of the fluorophores which may otherwise lead to an overestimation of the dissociation rate.

2.1.4 Ultra-low dissociation rate determination using an external force

The techniques above and many other approaches not discussed here [80] provide efficient ways to investigate biomolecular interaction by detecting the dissociation constant K_D. Furthermore, the surface plasmon resonance (SPR) technique (section 2.1.2) and the single-molecule approach (section 2.1.3) can also measure separately the association rate k_{on} and dissociation rate k_{off}, which is important for understanding complex features of both binding and detaching in a reversible reaction. For many interactions, the k_{on} value ranges from 10^6 to 10^7 $M^{-1}s^{-1}$ and the corresponding k_{off} value ranges from 1 s^{-1} (low affinity reaction with $K_D = 1\ \mu M$, if we consider that $k_{on} = 10^6$ $M^{-1}s^{-1}$) to 0.001 s^{-1} (high affinity reaction with $K_D = 1\ nM$,

if $k_{on} = 10^6$ $M^{-1}s^{-1}$), which means that k_{off} is the most variable rate and justifies why the k_{off} value is considered as an affinity determination parameter [81]. However, for many biomolecular complexes with a very high affinity (e.g. 10 pM-10 nM), the dissociation rate may be too small to be measured in SPR or single-molecule experiments. Indeed, very low dissociation rates (<10^{-3} s^{-1}) would require observation times that are too long to be practicable. For example, in drug design, the higher the affinity between the drug and its in-vivo target, the higher it can be efficient which can avoid harmful side effects.

For this latter case of low dissociation rates, we have developed an alternative technique. The basic idea is to apply an external force on one of the two molecules of the bound molecular complex to decrease the energy barrier that must be overcome for dissociation to take place. We developed a setup that uses a microfluidic system with a hydrodynamic force to achieve this (see section 2.2.2). To increase the impact of the force to separate the bimolecular complex, we attach a nanoparticle with a radius R to the binding molecule as a kind of kite (see section 1.2.1). Then the hydrodynamic force is proportional to the radius of the nanoparticle and not to the one of the molecule (see section 2.2.3). We can thus generate significantly higher forces.

We consider a simple dissociation process of a molecular complex AB:

$$AB \underset{k_{on}}{\overset{k_{off}}{\rightleftharpoons}} A + B \tag{2.13}$$

This reaction is associated with a potential energy surface (PES) along the reaction coordinate and can be described as a typical double-well potential curve as shown in Fig. 2.6. The potential varies with the distance between the two molecules. To escape from the complex state AB (left well) to the free state $A + B$, the molecule AB must acquire enough energy to cross the energy barrier. The dissociation rate constant k_{off} depends exponentially on the barrier height according to Kramers theory [82]:

$$k_{off} = \frac{1}{\tau_{off}} = C \cdot e^{-\Delta E / k_B T} \tag{2.14}$$

This is the Kramers result of unimolecular reaction (such as protein folding or dissociation of a protein-ligand complex) for the dissociation rate from the complex AB to the transition state A-B. Here, τ_{off} is the characteristic escape time , C represents the pre-exponential factor which depends on the curvature of the potential energy surface at the bottom of the left well and at the transition state A-B, ΔE denotes the change in energy between the transition state A-B and the complex AB at rest, k_B is the Boltzmann's constant, and T is the temperature [83].

We then apply a hydrodynamic drag force F on complex AB through a luminescent nanoparticle. To achieve this, molecule A is fixed on the glass surface of a microchannel, molecule B is coupled with a nanoparticle and then injected into the microchannel to form a complex AB by specifically binding with molecule A. The external drag force is then applied and significantly increases the probability of dissociation of molecule A and its coupled nanoparticle from the molecule B. Indeed, the energy barrier between the two wells becomes $\Delta E - F \cdot a$, as shown in Fig. 2.6B. The dissociation rate under a hydrodynamic force application, $k_{off}(F)$, can then be determined based on Kramers theory[82], [84], which is commonly used in the analysis of external-force dependent chemical reactions:

$$k_{off}(F) = k_{off}(0) \cdot e^{F \cdot a / k_B T} \tag{2.15}$$

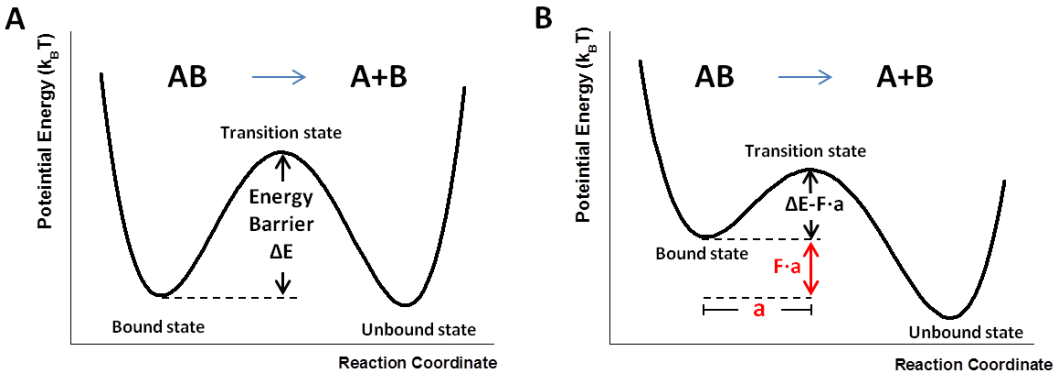

Figure 2.6: Reaction coordinate diagram for the separation of the molecular complex AB in the absence of external force (left) and in the presence of an external force F (right). a is the characteristic distance of the bimolecular bond.

where F is the applied force, a is the characteristic distance interpreted as the distance along the reaction coordinate AB to the transition state A-B (Fig. 2.6B), $k_{off}(0)$ is the dissociation rate of the reaction in the absence of external force. This equation can also be written as:

$$\tau_{off}(F) = \tau_{off}(0) \cdot e^{-F \cdot a / k_B T} \tag{2.16}$$

where $\tau_{off}(F) = \frac{1}{k_{off}(F)}$ the characteristic time of dissociation under force F.

The attached luminescent nanoparticle (NP) also signals the dissociation and departure of molecule B when the glass surface of the microscope is imaged with a fluorescence microscope capable of visualizing single particles. By plotting the number of remaining attached nanoparticles N as a function of time and doing an exponential fit as will be discussed in section 2.3.2:

$$N = N_0 \cdot e^{-t/\tau_{off}(F)} + N_b \tag{2.17}$$

we can extract $\tau_{off}(F)$. Here, N_0 is the total number of B-NP conjugates bound to A.

Based on Eq. (2.16) and by fitting the experimental $\tau_{off}(F)$ for different experimental force values, we can extrapolate the characteristic time at zero flow force $\tau_{off}(0)$, as shown in Fig. 2.7.

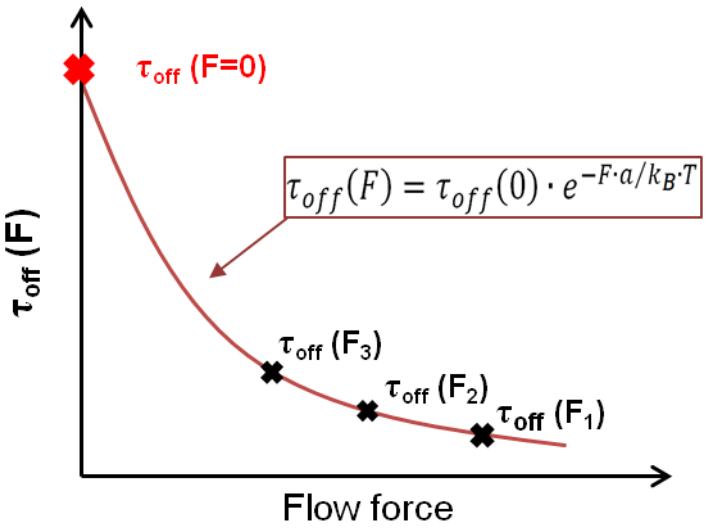

Figure 2.7: By applying equation 2.17 and multiple experiment results $\tau_{off}(F)$ for different flow force values, the dissociation rate $\tau_{off}(0)$ is determined at zero flow force.

2.2 Experiment Set-up and Samples preparation

2.2.1 HB-EGF and DTR8

Heparin-binding epidermal growth factor-like growth factor (HB-EGF) is a 208 amino acids protein [85], which belongs to the epidermal growth factor (EGF) family. It was first identified from human macrophage-like cells in 1991 [86]. It contains an EGF-like domain that mediates binding to the EGF receptor [87].

The HB-EGF is expressed in a wide range of wild-type cells and in different organs (*e.g.* skin, liver, intestine, brain, etc.) and plays a critical role in cellular proliferation, migration, adhesion, differentiation, and tissue regeneration throughout the body [88]. Increasing evidence has shown that the overexpression of HB-EGF is significantly elevated in multiple types of cancer [89]–[91]. HB-EGF is moreover known to be involved in the pathological mechanism of rapidly progressive glomerulonephritis, a life-threatening disease in kidney [92] and has therefore attracted significant interest as a pharmaceutical target.

The HB-EGF gene is initially expressed as a transmembrane precursor form named pro-HB-EGF [93]. The ectodomain of pro-HB-EGF is then shed by a variety of proteases, such as disintegrins, metalloproteinases (ADAM), and matrix metalloproteinases (MMP) to release soluble, mature HB-EGF from the cell membrane [94], as shown in Fig. 2.8. As one of the ligands of EGFR, a mature HB-EGF molecule, can bind epidermal growth factor receptor (EGFR), ErbB-1 and ErbB-4 (also called HER-1 and HER-4), induce the formation of homo- or heterodimeric complexes of the receptors and activation of their intrinsic, intracellular kinase site. This activation results in the phosphorylation of specific tyrosine residues of EGFR and leads to activation of intracellular signaling pathways which may be diverted in cases of tumor formation [95].

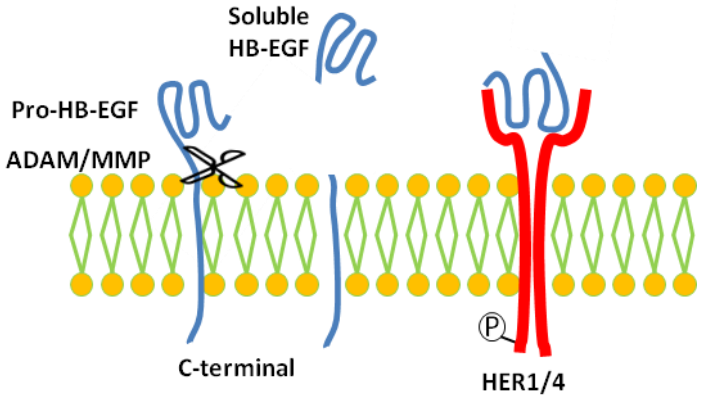

Figure 2.8: The ectodomain of pro-HB-EGF is shedded by proteases (ADAM and MMP) to release a soluble HB-EGF from the cell membrane. Then, soluble HB-EGF can bind to EGFR and lead to EGFR activation.

Pro-HB-EGF also happens to be targeted by the diphtheria toxin [96]. Based on this observation, a nontoxic mutant of diphtheria toxin that preserves the binding properties of the native molecule called cross reacting material 197 (CRM 197) has been commonly used as anticancer agent in clinical trials. As a natural ligand of HB-EGF, it is capable of targeting HB-EGF and prevent its mitogenic activity through blocking its binding to EGFR [96]. Based on the same HB-EGF targeting mechanism, another nontoxic mutant of diphtheria toxin, named DTR8, was discovered by Daniel Gillet *et al.* as described in patent [97]. Compared with CMR 197, DTR8 has a smaller size (CMR197 is 58 kDa and DTR8 is 17.5 kDa), a higher affinity for HB-EGF (60,300 times higher than CMR 179) and a lower toxicity [97]. As an anti-cancer agent, DTR8 considerably reduces the risks of side effects.

Moreover, HB-EGF and activation of EGFR by HB-EGF has been shown to be implicated in an invalidating kidney disease, rapidly progressive glomerulonephritis [98]. In this case also, diphtheria toxin mutants are highly promising as potential drugs inhibiting HB-EGF binding to EGFR.

In this chapter, by applying a hydrodynamic force, we measured and determined the affinity of these two specific proteins, HB-EGF and DTR8. We chose this molecular pair of molecules

because the measured K_D is very small and the corresponding k_{off} could not be measured with the SPR technique because the dissociation times were too long.

2.2.2 Microfluidic System and Sample Preparation

Microfluidic channel preparation

To generate a stable laminar flow force on the molecular complex, a one-line microchannel was developed as shown in figure 2.9 (A). The microchannel material, polydimethylsiloxane (PDMS), was molded as described in Ref. [99]. Briefly, the microchannel molds were prepared by using the dry film photoresist soft lithography technique [99]. A glass slide as a bedplate of the mold was thoroughly cleaned by using ethanol and compressed air. We then peeled off the inner protective plastic cover of a piece of UV-sensitive dry film (ORDYL AM120DI) with a thickness of 30 µm, tightly pressed the UV-sensitive material on the glass slide to avoid bubbles and then fixed the dry film to the glass slide by heating and pressing it in the laminator at 90-100°C for 2 min. The protective plastic cover in the other side of UV-sensitive material was then taken off, and a dark mask with the shape of the microchannel mold appearing in transparency (one-line channel with a width of 200 µm in this experiment) was placed on the UV-sensitive material. To fix the UV-light induced solid mold on the glass slide, a UV-KUB machine (Cloé, France) was programmed to insolate the film on the glass slide through the mask for 30 s to 60 s with UV light. The exposed film area is transformed into a solid mold fixed on the glass surface. To remove the spare unfixed UV-sensitive material, the slide was sunk into 1% (10 mg in 1 mL) potassium carbonate solution for 10 to 15 min with stirring. When the spare material was completely removed, the microchannel mold was then dried off and placed in a Petri dish. Since the material is light sensitive, the molds have to be prepared away from light.

Once the microchannel mold was prepared, the microchannel material, polydimethylsiloxane (PDMS), can be poured into the Petri dish with a height of around 1 cm. The PDMS is prepared by mixing silicon elastomer with a curing agent at the ratio of 10 to 1 and then removing the bubles by centrifugation at 2000 rcf for 2 min. After incubation in the oven at 75°C for four hours or overnight, the PDMS was totally hardened. The microchannel can be cut from the mold, cleaned together with a glass coverslip in the plasma cleaner and then sealed by depositing the

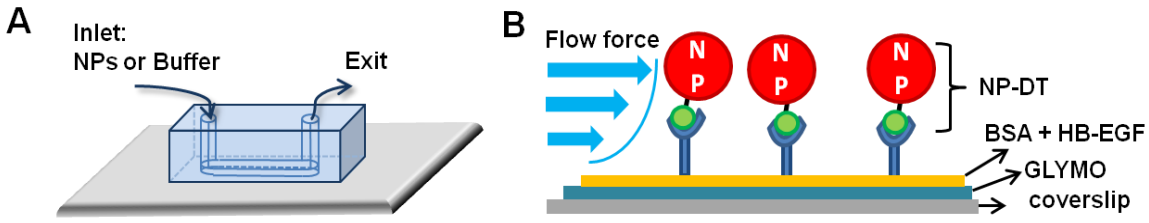

Figure 2.9: (A) Illustration of the microfluidic channel geometry. (B) Conceptual graphic of the system.

PDMS channel on the glass coverslip to form the microchip. The plasma cleaner leaves free radicals on the surface being cleaned and ensures that they stick together with a weak mechanical pressure. These microchips possess a channel with a width of 200 µm and a height of 30 µm and have an inlet for fluid flow or reactant addition, and an exit (Fig. 2.9A).

Surface treatment

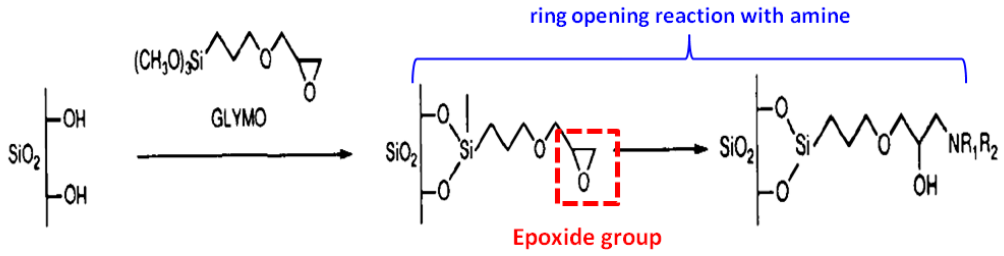

Figure 2.10: Amine immobilization on a glass surface (SiO_2) with GLYMO. Figure extracted from Ref. [100]**.**

To immobilize HB-EGF molecules in the resulting microchannel described above, we must cover the inner glass surface of microchannel firstly with 3-Glycidyloxypropyl trimethoxysilane (GLYMO). As a coating agent, GLYMO deposited on the glass, forms stable Si-O-Si bonds with the silica surface and exposes an epoxide group which allows the facile reaction with a variety of amines, such as bovine serum albumin (BSA), by a ring opening reaction as shown in Fig. 2.10 [100].

After injection (described below) and incubation with HCl solution containing 4.5 g/mL GLYMO at room temperature for 60 min, the microchannel were rinsed lightly with 250 µL 5% BSA solution (50 mM, pH7.4 Tris-HCl buffer containing 5% (50 mg/mL) BSA) to remove the free GLYMO.

In the meantime of incubation, the two sample groups (test and control) were prepared. For test groups, we injected 25 µL 0.5 µM HB-EGF (dissolved in 5% BSA). For control experiments, we injected 25 µL 5% BSA without HB-EGF molecules. Note that, the 5% BSA here is for blocking the nonspecific binding sites of GLYMO. The samples were then incubated at room temperature for 60 min. During the incubation, the nanopaticle-labeled diphtheria toxin R-domain derivative (NP-DTR8) was prepared.

NP preparation

The luminescent nanoparticles, $Y_{0.6}Eu_{0.4}VO_4$, used in this work were synthesized and functionalized as described in Refs. [12], [101]–[104]. Briefly, nanoparticles were prepared by a precipitation reaction of sodium orthovanadate aqueous solution with dropwise addition of yttrium and europium nitrate precursor solutions. After dialysis against water to remove the remaining counter-ions, nanoparticles were covered with a silicate layer through depositing silicate ions from an aqueous solution of tetramethylammonium silicate and then functionalized with a silicon alkoxysilane (3-aminopropyltriethoxysilane, APTES). Lastly, to achieve coupling with proteins, such as DTR8, the APTES-functionalized nanoparticles interacted with an amine-reactive cross-linker bis (sulfosuccinimidyl) substrate (BS_3) in a first step and then reacted with DTR8 in a second step [103], [104]. After purification with centrifugation, the NP-DTR8 conjugates with a DTR8: NP coupling ratio of 54:1 was stored at -80°C. Even though this coupling

ratio is very high and may lead to binding to multiple HB-EGF molecules on the surface, we will show below that this can be avoided by lowering the HB-EGF concentration on the surface..

Experimental conditions

Before injection, 10 µL NP-DTR8 was first diluted in 200 µL 50 mM HEPES buffer (4-(2-hydroxyethyl)-1-piperazineethanesulfonic acid). The nanoparticles were then resuspended by sonication at 70% power for 5 sec (sonicator, power: 130w, Bioblock Scientific NO. 75185) and the oversized or aggregated particles were removed by centrifugation at 2000 rcf for 5 min. We then took the NP-DTR8 suspensions and sonicated again at 70% output for 5 sec to dissolve any remaining aggregates, to finalize the preparation.

After incubation with the BSA/HB-EGF solution, the microchannels were rinsed lightly with 250 µL 5% BSA solution to remove the free BSA and HB-EGF. Then, a syringe containing the NP-DTR8 conjugates was inserted into the microchannel inlet and the injection was performed at the low flow rate of 3µL/min for 5 min. The channels containing the NP-DTR8 conjugate solution were then incubated for 60 min at 37°C. The last step involved rinsing with observation medium 50 mM HEPES buffer at a low flow rate 100 µL/min to remove unbound nanoparticles.

For injecting solutions into the microchannels above, two syringe pumps were used. A first syringe pump (Harvard Apparatus) with the 10 mL syringe (SGE Analytical Science Syringe) was applied to inject liquid with a series of tightly controlled flow rates which can lead changes of characteristic dissociation time τ_{off} as a function of flow force (described in section 2.1.4), in this experiment, flow force values were controlled by the following flow rates: 1, 1.5, 2, 2.5 and 3 mL/min. The 2nd syringe pump (KD Scientific) with 0.5 mL syringe was used to inject reactants, such as GLYMO, HB-EGF, BSA and NP-DTR8 in this experiment. Tubing (Adtech) with 1.07 mm outer diameter and 0.56 mm inner diameter was used to connect the syringe on the pumps to the sample channel. Additional tubing was used at the exit of microchannel to collect the used solution.

2.2.3 Hydrodynamic Force Application

As described in section 2.1.4, external hydrodynamic force applied on nanoparticle bound complex AB can significantly increase the probability of dissociation of molecule A and its connected nanoparticle from the molecule B, which provide a tool to measure very low dissociation rates. To generate a stable laminar hydrodynamic force on the molecular complex, a simple one-line microchannel was used (Fig. 2.9A).

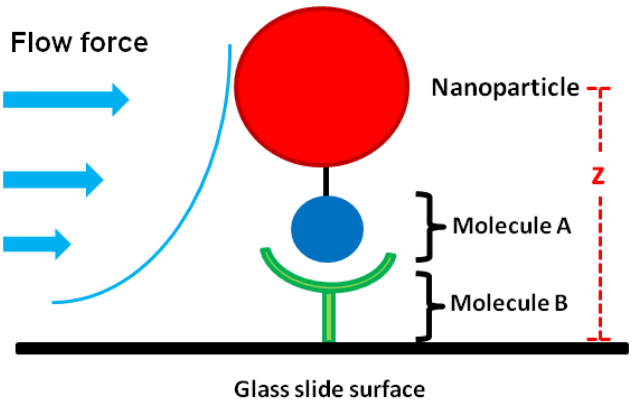

Figure 2.11: Scheme of the approach used to measure low dissociation rates. A flow force pulls on the bond between molecule A and molecule B by pushing the nanoparticle attached to molecule A. As a result the dissociation energy barrier is lowered and the dissociation rate increases. In the experiments described in this chapter, molecule A is DTR8 and molecule B is HB-EGF .

After immobilization of molecule B at the glass surface of microchannel and incubation with the nanoparticle-labeled molecule A resulting in binding of molecule A to molecule B, a controlled flow can be applied using a syringe that injects liquid at a constant flow rate (section 2.2.2). The flow acts on the nanoparticle in solution which experiences a drag force. This drag force will act on the bond between molecule A and molecule B by pushing the nanoparticle (Fig. 2.11). In our experiment, as explained in section 2.2.2, multiple flow rates are applied to reduce the energy barrier between the two biomolecules, accelerate the dissociation rate constant $k_{off}(F)$ (section 2.1.4), and thus allow its determination. We can then determine the dissociation rate $k_{off}(0)$ in the absence of force using the Kramers equation.

We assumed a laminar flow applied in this experiment, and the drag force on the nanoparticle can be described by the Stokes equation:

$$\boldsymbol{F}_d = 6\pi\eta_{eff} r_{NP} \boldsymbol{v}_{flow} \tag{2.18}$$

where $\boldsymbol{v}_{\mathrm{flow}}$ is the velocity of the liquid which can be determined by using the Poiseuille equation or particle velocimetry at the precise distance of the attached NP from the glass, and $\mathrm{r_{NP}}$ is the NP hydrodynamic radius which can be estimated as described in Ref. [44]. Briefly, the size (diameter) of the Eu-doped nanoparticles $\mathrm{Y_{0.6}Eu_{0.4}VO_4}$ is determined from the emitted photon numbers based on the fact that nanoparticle luminosity is proportional to the number of Eu dopants and ranges from 20-40 nm. Note that, from the photon number, we estimated the physical (real) nanoparticle radius, but the hydrodynamic radius is a bit larger than the nanoparticle radius due to the functionalization layer [104] and the solvation layer around the nanoparticle. Taking these layers into account, we took an average value of the NP radius of 25 nm. Note that this approximation only has a small influence on the results, since these layers are expected to be thinner than a few nm. Furthermore, as discussed below, a common correction factor applied to all force values has a negligible effect on the extracted $\tau_{off}(0)$.

In our case, the distance to the glass surface is comparable to $\mathrm{r_{NP}}$, therefore hydrodynamic flow modifications around the nanoparticle modify this drag force. Here, the introduced effective viscosity η_{eff} can no longer be considered as the viscosity of the bulk liquid viscosity η_0. We take for this effective viscosity value η_{eff} the Faxén's law [105].

$$\eta_{\mathrm{eff}} = \frac{\eta_0}{1 - \left(\frac{9r_{NP}}{19z}\right) + \left(\frac{r_{NP}^3}{8z^3}\right) - \left(\frac{45r_{NP}^4}{256z^4}\right) - \left(\frac{r_{NP}^5}{16z^5}\right) + \cdots} \tag{2.19}$$

Here, for our buffer solution, HEPES, η_0 can be taken to be equal to the water viscosity $\eta_{\mathrm{water}} = 0.001\ \mathrm{Pa \cdot s}$, and z represents the vertical position indicating the distance from the zero-flow plane to the center of the nanoparticle. Since the surface of microchannel is hydrophilic (the zero-flow plane may lie outside the channel dimensions only if the surface is highly hydrophobic [106]), we can assume a zero-flow plane on the glass surface. The distance z can then assumed

to be equal to the radius of the NP (r_{NP}) plus the size of the diameters of molecule A (d_A) and molecule B (d_B) coupled with the NP as shown in Fig. 2.11. Here, z value can be determined as:

$$z = r_{NP} + d_A + d_B \tag{2.20}$$

Table 2.1 **Flow rate (mL/min) to flow force (pN) conversion**: The flow force estimated using the Poiseuille equation and the Stokes law, and a protein size of 4 nm, for different flow rates.

Flow rate (mL/min)	Flow force (pN)
1	13.8
1.5	20.7
2	27.6
2.5	34.5
3	41.4

For the molecular pair HB-EGF and DTR8 (section 2.2.2), we estimated protein diameters from the molecular weight ($W_{HB-EGF} = 9.7\ kDa$ and $W_{DTR8} = 1.75\ kDa$) and the mean density of proteins $\rho = 1.43 \pm 0.03 g/cm^3$[107], and found $d_{HB-EGF} = 2.8\ nm$ and $d_{DTR8} = 1.6\ nm$. The distance z therefore is determined to be 29.4 nm and the efficient viscosity $\eta_{\text{eff}} = 0.0018\ \text{Pa} \cdot \text{s}$

By using the Poiseuille equation, which describes the laminar flow profile and average flow velocity, we can calculate the flow speed at the height of the nanoparticle.

$$\boldsymbol{v}(\boldsymbol{z}) = v_{mean}\left(-\frac{4}{h^2}\right)(z^2 - hz) \tag{2.21}$$

$$v_{mean} = \frac{3U}{2A} \tag{2.22}$$

where h is the height of microchannel, 30 μm, A is the cross area of the microchannel ($30\ \mu\text{m} \times 200\ \mu\text{m} = 6{,}000\ \mu\text{m}^2$ in this experiment), and U is the flow rate (1, 1.5, 2, 2.5, 3

mL/min). By using these given values, we can then obtain the flow speed at the center of the nanoparticle.

With the flow speed determined above, we can estimate the force that acts on a nanoparticle by using the Stokes law $\mathbf{F} = 6\pi\eta_{\mathrm{eff}}\mathrm{r}\mathbf{v}_{\mathrm{flow}}$. The results of flow forces are shown in Table 2.1.

2.2.4 Image Recording

The experiments in this section were all performed with Olympus IX-81 (Olympus) inverted microscope equipped with a 63×, NA=1.4 oil immersion objective and an electron-multiplying charge-coupled device (EM-CCD) (Quant EM: 512SC; Roper Scientific). The $\mathrm{Y_{0.6}Eu_{0.4}VO_6}$ nanoparticles are excited with a laser diode at 465 nm (Modulight). And the emission of the NPs is collected through 617/8 nm filter (Chroma Technology). The laser power was set to 30 mW and images were acquired at an exposure time of 200 ms and a read out time 1.3 ms. The pixel arrays from EMCCD are then sent from the camera to the computer and viewed as an image by using MetaVue software package.

The image recording starts after NP-DTR8 coupling. Series images at the focal plane are captured during rinsing in 5 min and during the flow force application in 10 min respectively. In this experiment, we recorded three different concentrations (0.1, 0.5, 50 µM) of HB-EGF under the same flow rate (2.5 mL/min), to determine the optimal HB-EGF concentration, and five different flow rates (1.0, 1.5, 2.0, 2.5, 3.0 mL/min) at the same HB-EGF concentration (0.5 µM) to be able to deduce $\tau_{off}(0)$.

2.3 $\mathbf{k_{off}}$ Determination between HB-EGF and NP-DTR

To determine the dissociation rate k_{off} between HB-EGF and NP-DTR, two steps of calculation were performed as described below. We decided to determine the dissociation rate k_{off} between HB-EGF and NP-DTR8 by using our setup described in the sections above, by measuring the dissociation rate of nanoparticle-labeled DTR8 under different flow forces.

2.3.1 Dissociation between HB-EGF and DTR-NP during Force Application

To extract characteristic k_{off} time at particular force, we recorded the number of detached nanoparticles as a function of time during hydrodynamic flow applied. As shown in Fig. 2.12B, there are 34 nanoparticles on the surface at the beginning of the experiment in this field. After 5 min, no more nanoparticle detachments occurred and 20 nanoparticles remained attached in

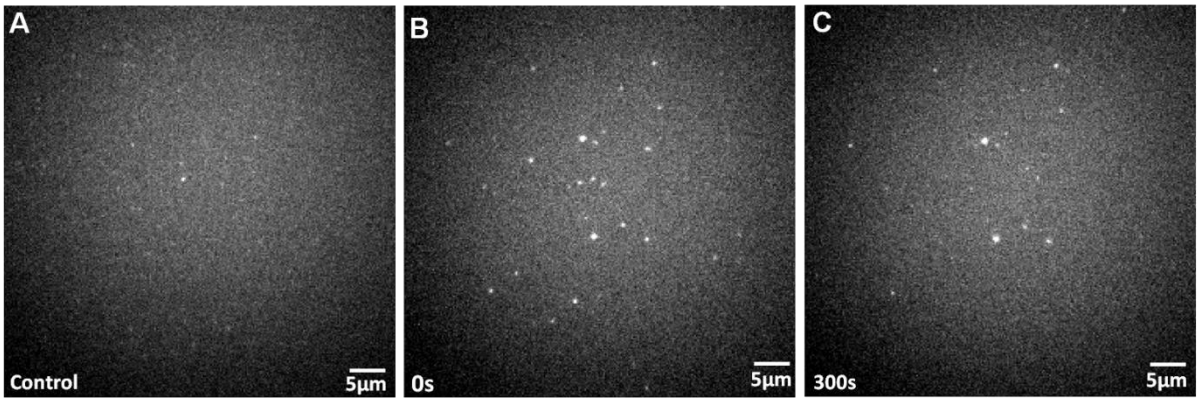

Figure 2.12: The number of nanoparticles on the surface in the microchannel A) Control: 5% BSA instead of HB-EGF, there are few non-specifics binding in the field compare to B), 0.5µM HB-EGF was injected and then incubated with NP-DTR8 during 30 min at 37°. C). The same field after 5 min under a hydrodynamic flow (flow rate: 2 mL/min) applied. Exposure time: 200 ms.

Fig. 2.12C. Additionally, a control experiment without HB-EGF injection was performed. As shown in Fig. 2.12A, there are few nanoparticles visible in the field and the number of nanoparticles is significantly lower than Fig. 2.12B. Therefore, we assume that the florescence signal we observed in the microchannel is due to specific binding between NP-DTR8 and HB-EGF.

Considering there is a relative large number of nanoparticles remaining on the surface after flow force application, and the nanoparticles are a significantly larger (r_{NP}~$25nm$) than the proteins with a high DTR8:NP ratio of 54:1, there may be more than one DTR8-HB-EGF bond per nanoparticle, which may be responsible for an increase of the energy barrier. Alternatively, there may be two subpopulations of DTR8-HB-EGF complexes, one with a fast dissociation time and one with a much longer one, not accessible in our experiments. To reduce this multiple

binding and find a proper concentration of HB-EGF, we recorded nanoparticle detaching for different concentrations of HB-EGF at the same flow rate as shown in Fig 2.13. In order to obtain reliable results, we repeated this experiment multiple times to have a larger number of detached nanoparticles. By plotting the number of remaining attached

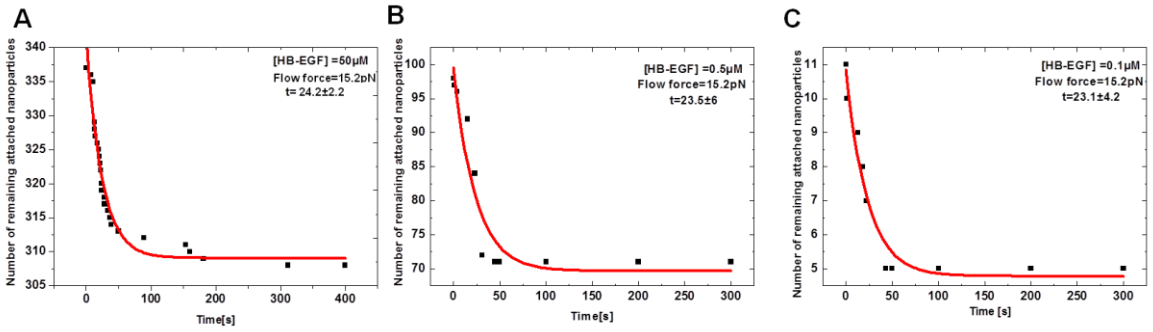

Figure 2.13: Exponential fit of the remaining attached nanoparticles number as a function of time, we extracted the characteristic k_{off} time at particular force 15.2 pN. (A) HB-EGF concentration is 50 µM; the characteristic k_{off} time is 24.1±2.1 s. (B) HB-EGF concentration is 0.5µM; the characteristic k_{off} time is 23.5±6 s. (C) HB-EGF concentration is 0.1 µM; the characteristic k_{off} time is 23.1±4.2 s.

nanoparticles as a function of time and doing an exponential fit according to equation 2.17, we extracted the characteristic k_{off} time. From results shown in Fig. 2.13A, B and C, we can see that the characteristic k_{off} time value is the same even when the HB-EGF concentration is changed from 50 µM to 0.1 µM, which assured that this approach and results are robust. As the HB-EGF concentrations are decreased, the percentages of detaching nanoparticles ($\frac{N_0}{N_0+N_b}$) are increased.

$$N = N_0 \cdot e^{-t/\tau_{off}(F)} + N_b \tag{2.23}$$

Nanoparticles are rarely found for experiments with 0.1 µM HB-EGF (11 nanoparticles in total) leading to low statistics. On the other hand, experiments with 50 µM HB-EGF may have a large amount of multi-valent NP-HB-EGF coupling. Indeed, for experiments with an HB-EGF concentration of 50 µM, 92% nanoparticles remain after flow application compared to 78%

nanoparticles remaining for an HB-EGF concentration of 0.5 µM. This indicates that there is more multi-valent NP-HB-EGF binding for experiments with an HB-EGF concentration of 50 µM. We therefore chose 0.5 µM HB-EGF as a working concentration in the flowing experiments.

2.3.2 k_{off} Determination

We then performed multiple experiments to find the characteristics dissociation time under five specific flow rates, and for each flow rate value we have three times repeats to allow us collecting enough detached DTR-NPs. By applying equation 2.23, we calculate the applied flow force corresponding to each flow rate.

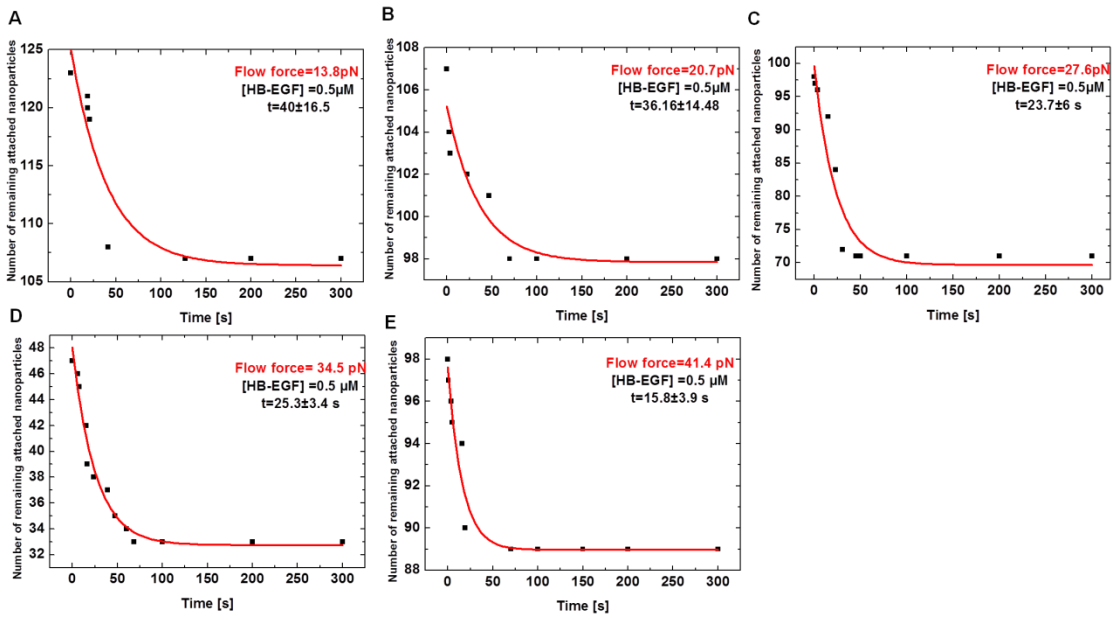

Figure 2.14: The characteristic k_{off} time extracted by exponential fitting of the remaining attached nanoparticles number as a function of time. (A) Flow force is 13.8 pN (B) flow force is 20.7 pN. (C) Flow force is 27.6 pN. (D) Flow force is 34.5 pN. (E) Flow force is 41.4 pN.

As shown in Fig.2.14, nanoparticles detached during the first 100 s, 16 (13%) nanoparticles detached under the flow force of 13.8 pN, and 9 (8%), 26 (27%), 14 (30%), 9 (9%) nanoparticles detached under the flow force of 20.7, 27.6, 34.5, 41.4 pN respectively. We then fit

the remaining attached nanoparticles number as a function of time by using equation 2.23 to extract the characteristic time $\tau_{off}(0)$ at corresponding flow force.

By using equation $\tau_{off}(\boldsymbol{F}) = \tau_{off}(0) \cdot e^{-\boldsymbol{F}\cdot a/k_B\cdot T}$ described in section 2.1.4 as a fit function, we can find $\mathrm{k_{off}}$ at the zero force. The results are shown in Fig. 2.15. We find the value of characteristic dissociation time $\tau_{off} = 62.3 \pm 20.7$ s, and

$$k_{off} = 0.016 \pm 0.005\ s^{-1}$$

We compared this value with the one calculated indirectly from k_{on} and K_D values by Gillet's team (D. Gillet, private communication) for a similar mutant G2. This team determined the association rate k_{on} from surface plasmon measurements. However, the k_{off} rate was too low and could not be measured with the SPR technique. Therefore, the team calculated k_{off} indirectly from $k_{on}$and from the equilibrium constant K_D obtained from a competitive binding assay of DTR8 in the presence of diphtheria toxin where the viability of cell cultures was measured as a function of [DTR8]. They found:

$$k_{off} = 5.94 \cdot 10^{-5} s^{-1}.$$

The k_{off} value in our experiments is three orders of magnitude larger than the value found in D. Gillet's calculation (private communication). This difference cannot be explained by the approximations used to determine the flow force value. Indeed, changing the force values by a typical factor of 2 to 10, which may be expected in the case of an inaccurate force determination, does not affect the extracted $k_{off}(0)$ in these proportions. As shown in Fig. 2.15, in our experiment, the exponential fitting strongly depends on the dissociation rate at low force values. To get more precise and reliable values of the characteristic dissociation time, more values at lower flow forces are required. Furthermore, these results may reveal the existence of two populations of bound complexes between HB-EGF and DTR8, one with a conformation leading to a fast dissociation rate and a second majority population with a slow dissociation rate. This may explain why a large number of complexes do not detach upon flow force application. If

this explanation is correct, prolonging the observation time is required in future experiments to be able to observe this longer dissociation time.

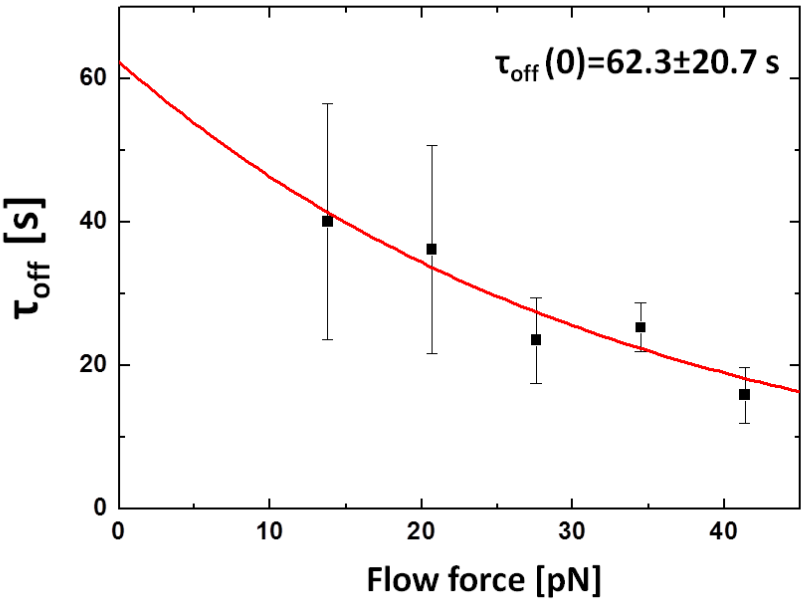

Figure 2.15: Dissociation rate between HB-EGF and NP-DTR8 is extracted by fitting the characteristic dissociation time under different flow rate values versus the flow force.

2.4 Comparision with SPR Results

The aim of this work was to first implement the force generation technique to demonstrate its validity in an optical microscope detecting the nanoparticle luminescence and then transpose it to a Surface Plasmon Resonance apparatus, which does not require the nanoparticles to be luminescent. Preliminary results obtained by Rivo Ramodiharilafy, technical engineer in our team, are encouraging, in agreement with the results obtained by optical microscopy, and are briefly discussed below.

As for the optical microscope experiments, HB-EGF was deposited on the surface and the NP-DTR8 containing solution was added using the fluid manipulation system of the surface plasmon

resonance apparatus at a weak flow rate of 25 µL/min. Note that the force corresponding to this flow rate is, in this case, quite low, much lower than in the microchannels discussed above, because the dimensions of SPR flow chamber are much bigger than those of the microchannels. A Horiba SPRi-Plex II instrument was used which has the following specificity: instead of measuring the full reflectivity curve as a function of the angle, as is usually the case in the standard surface plasmon resonance instruments (for example, by the company Biacore), the reflectivity angle is kept fixed and the intensity variations due to the shift of the surface plasmon resonance peak are measured (see Fig. 2.2). Using a CCD camera instead of a single detector, this approach enables the simultaneous measurement of the reflectivity changes for up to 400 spots with the same or different conditions of molecules bound to the gold-coated prism surface. This SPR variant is designated SPRi for SPR imaging. We used the Horiba SPRi Arrayer with a 500 nm needle to spot two rows of 8 identical HB-EGF spots and two rows of 8 identical hemoglobin (Hb) spots used as a control molecule to correct for refraction index changes which are not due to specific binding of the analyte to the HB-EGF spots. Such refraction index changes may be due to non-specific binding, apparatus drift changing the reflectivity baseline or refractive index changes due to the change of liquid when the NP-DTR8 containing solution starts flowing instead of the buffer solution alone.

Figure 2.16 shows the SPRi data obtained after averaging the 16 HB-EGF-coated interaction spots and the 16 Hb-coated interaction spots followed by a subtraction of the two. The concentration of HB-EGF and Hb solutions spotted on the gold-coated prism was 0.5 µM (this concentration was chosen after optimization) and the NP-DTR8 concentration of the analyte solution was 9 nM. In this case, a new NP-DTR8 conjugate batch was used with a 4:1 DTR8:NP coupling ratio, which, given the size of the nanoparticles (around 30 nm), precludes multiple binding to HB-EGF molecules spotted on the surface. The analyte concentration therefore refers to the nanoparticle concentration.

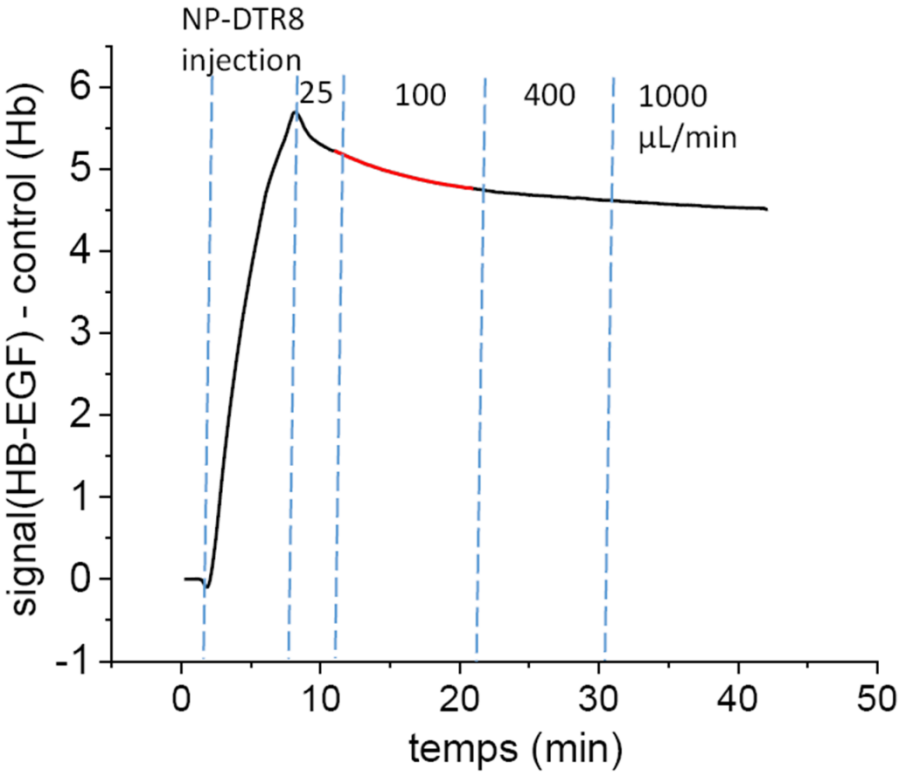

Figure 2.16: Reflectivity changes measured upon addition of NP-DTR8 containing solution (binding step from 1.8 to 7.8 min; the NP-DTR8 injection takes place from t=0 min to t=6 min but the binding step is delayed due to the dead time required for the injected liquid to go through the tubing and reach the flow chamber) and rinsing with a flow rate of 25 µL/min during 4 min, then rinsing with a flow rate of 100 µL/min during 10 min, rinsing with a flow rate of 400 µL/min during 9 min, and a flow rate of 1000 µL/min during 11 min. The red line is an exponential fit to the time range of 12 to 22 min. The blue dashed lines indicate the changes in circulating solution in the prism flow chamber and/or changes of the flow rate. The y-axis corresponds to the % of reflectivity change.

When the NP-DTR8 containing solution arrives inside the flow chamber at the gold surface, its binding to HB-EGF leads to a reflectivity signal increase (Fig. 2.16). After rinsing with buffer without NP-DTR8, the dissociation process can be observed. An exponential fit to the initial decay for a flow rate of 100 µL/min for t=12 to 22 min shows that only a small fraction of NP-DTR8 analytes detach (5.7%), which is similar to what is observed in the fluorescence

microscopy experiments. Moreover, the exponential fit yields a characteristic time of 7.69±0.06 min, i.e. 461±4 s. This value is longer than the one deduced from the microscopy experiments (62±21 s; Fig. 2.15) but confirms that a fraction of the pair population dissociates with a faster characteristic dissociation time.

When higher flow rates are applied (up to 1000 μL/min), we do not observe a significant increase in the characteristic dissociation time. This means that higher forces need to be applied (the maximum flow rate supported by the SPRi instrument is 2000 μL/min) and/or nanoparticles of larger size need to be used.

2.5 Conclusion and Discussion

This chapter introduced a technique for the determination of low dissociation rates of biomolecules using a hydrodynamic force generated in a microfluidic system. By labeling with single luminescent nanoparticles, the forces applied on biomolecular complex are amplified due to the larger radius of the nanoparticle compared to the typical protein size. Therefore, using nanoparticles with a hydrodynamic radius of 50 nm, relatively high forces upto 40 pN can be generated. The advantage of this method is that this external drag force significantly increases the probability of dissociation of the bimolecular complex, decreasing the characteristic time of dissociation. We thus expect to obtain the determination of low dissociation rates which may be too small to be measured in SPR or single-molecule experiments. Furthermore, due to the luminescent properties of the $Y_{0.6}Eu_{0.4}VO_{0.4}$ nanoparticles, i.*e.* very high photo-stability without blinking, these can be observed under the hydrodynamic flow by a fluorescence microscope. The advantage of this approach is that it is inherently multiplexed in contrast to other techniques like optical tweezers. We can then obtain the experimental characteristic time $\tau_{off}(F)$ for different experimental force values by plotting the number of remaining attached nanoparticles N as a function of time. Subsequently, we can extrapolate to obtain the dissociation rate $k_{off}(0)$. We chose to apply this technique for the bimolecular pair of a drug target, HB-EGF, and its inhibitor DTR8 derived from the diphtheria toxin.

For the dissociation between HB-EGF and NP-DTR at zero force, we obtained $k_{off} = 0.016 \pm 0.005\ s^{-1}$. Comparing this value with the one calculated indirectly from k_{on} and K_D values by D. Gillet's team, the k_{off} value in my experiments is three orders of magnitude higher. This discrepancy may be explained by the fact that the exponential fitting and extrapolation to zero force in our approach strongly depends on the dissociation rates at low force values. Therefore, more dissociation time values at lower flow forces may be required to get a more precise and reliable value of the characteristic dissociation time at zero force. Furthermore, at the end of the experiment after hydrodynamic flow application, a large fraction of the initially bound nanoparticles still remains on the glass surface of the microchannel. In addition, control experiments with NP-DTR8 on glass surfaces without HB-EGF coating showed only very few non-

specific binding events in each field-of-view, which implies that the remaining bound nanoparticles at the end of the experiment are not due to non-specific binding. We can then assume that there may exist two kinds of bound states between HB-EGF and DTR8, one smaller fraction with a faster dissociation time and a bigger one with the long dissociation time extracted from the experiments of D. Gillet's team. In this case, it could be that only the faster detaching molecules are observed in my experiment, prolonged observation duration of higher flow forces would be needed in future experiments.

However, our data has demonstrated the principle of this technique. In the future, this technique could also be introduced in a Surface Plasmon Resonance apparatus, where a hydrodynamic flow is already implemented. In this case, the nanoparticles do not need to be luminescent but are just used as amplifiers of the flow force.

Chapter 3
Investigation of the Cell Membrane Organization with Long-Term Single-Particle Tracking

The cell membrane is one of the key structures in cell biology which contains a variety of biological molecules. It is highly organized and primarily consists of a 5- to 10-nm thick phospholipid bilayer with proteins embedded in it (Figure 3.1), which provides not only a

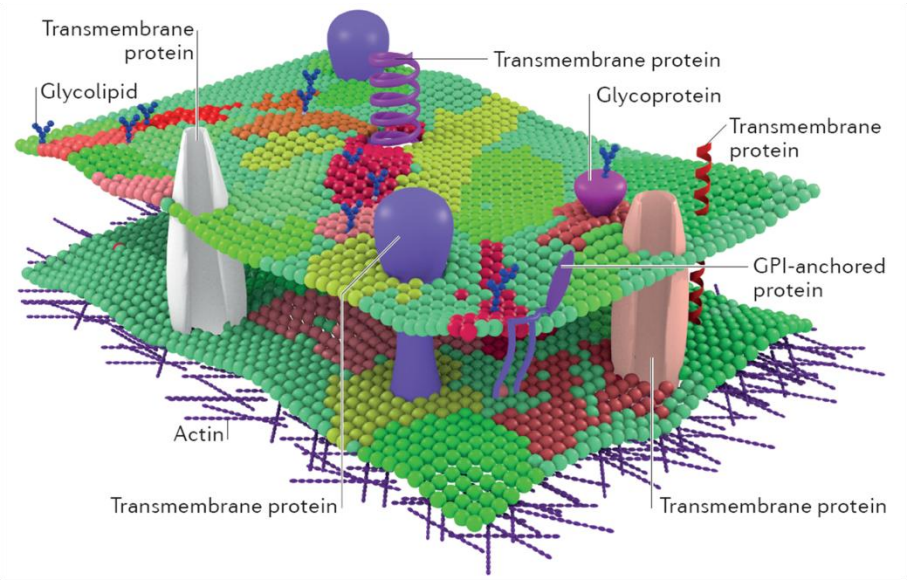

Figure 3.1: A general diagram of the cell membrane [108]**. It contains a variety of biological molecules including (1) a lipid bilayer forming the basis of the cell membrane and (2) proteins such as transmembrane proteins, glycoproteins and glycosylphosphatidylinositol (GPI)-anchored proteins. The cell membrane strongly interacts with an underlying layer of cross-linked actin filaments called the actin cortex which is responsible for the cell shape. Figure extracted from ref.**[108]**.**

boundary of the cell, but also a specific interface where many essential cellular processes occur,

including communication with the extracellular environment, transport of molecules and certain metabolic functions. To distinguish it from the membranes of intracellular compartments, it is often called plasma membrane.

The current knowledge about membranes and cellular processes taking place in it took more than three centuries of research to build [109]. The oligomerization, clustering and nanoscopic localization of membrane proteins can affect protein function and, consequently, the efficiency of cellular processes [110]. Therefore, the investigation of membrane organization is required to understand these mechanisms responsible for cellular processes. Progress is difficult because of the complex component distributions and of numerous active membrane processes. Despite the fact that the majority of the molecular building blocks and most of the organization principles are known, we still lack a quantitative understanding of the molecular interactions between membrane components, of the membrane coupling to the cell cortex, and of how these give rise to the structure and function of the cell membrane [111].

Cell membrane organization is essential for a variety of context-dependent cellular signaling processes, which govern basic activities of cells. For instance, through facilitating the colocalization (and possibly oligomerization) of membrane proteins and their relevant partners at the membrane, the membrane organization can achieve modulation of the protein function in signal transduction through the cell membrane [112].

Understanding these processes, the membrane organization and its functional role is a longstanding riddle that attracts a considerable amount of research using increasingly sophisticated experimental and analysis tools.

3.1 The Cell Membrane Organization

It has been around a century since Gorter and Grendel extracted lipids from red blood cells and precisely measured the surface covered by these lipid monolayers on water, which proved that the cell membrane was constructed by a lipid bilayer made of phospholipids with polar heads and non polar tails [113]. A decade later, Danielli and Davson first proposed the Davson-Danielli

membrane model which suggested that the cell membrane is not only made of lipids but also contains proteins attached to the sides of the lipid bilayer [114]. This model dominated cell membrane studies for the following 30 years. Our current understanding of the cell membrane structure is largely influenced by the fluid mosaic model proposed by Singer and Nicolson in 1972. This model presented their of the cell membrane structure which pictured the membrane as being “a sea” of lipids and membrane proteins integrated into the bilayer and presumably undergoing a random Brownian motion [115]. A year later, Yu et al. showed that the cell membrane can be separated into detergent-resistant and detergent-soluble fractions [116]. In the previous models of cell membrane organization, lipids in the bilayer were thought to function mainly as a structurally passive solvent for membrane proteins. However, based on the concept of heterogeneous distribution of certain lipids (glycerolipids, phosphatidylcholine and sphingolipids) and proteins between apical and basolateral membranes of epithelial cells [117], [118] and, moreover, of small invaginations of cell membrane, caveolae (described below), which contain glycosphigolipids and need cholesterol to function [118], [119], Simons and Ikonen proposed their lipid raft model to explain this lateral membrane inhomogeneity. This model postulated the existence of a kind of membrane domains, detergent-resistant lipid rafts, which are functionally important, relatively ordered membrane domains, rich in cholesterol and saturated sphingolipids, which can recruit other lipids and proteins by specific interactions [118], [120]–[122]. These membrane domains were proposed to contain proteins involved in signaling [112] and thus act as signaling platforms

Besides rafts, other types of detergent-resistant membrane microdomains were identifed, such as caveolae and tetraspannin-enriched microdomain (TEMs). Caveolae are membrane domains with smaller size (60-80 nm), first identified by electron microscopy 60 years ago [123]. They are cholesterol-enriched membrane flask-shaped invaginations which contain of caveolin and cavin proteins. These proteins interact with each other to regulate signal transduction, endocytosis, and transport of free cholesterol [124], [125]. Another type of membrane microdomain, tetraspannin-enriched microdomain (TEM), was identified during the 1990s [126]. Tetraspanins are a family of transmembrane proteins with four transmembrane domains found in the plasma membrane and in intracellular vesicles. They have four transmembrane alpha-

helices and two extracellular domains with a small and a large extracellular loop, and two short cytoplasmic tails [19]. The diameter of a TEM varies among cell types between 100 and 300 nm. The assembly of TEMs is dependent on tetraspanin–tetraspanin interactions and tetraspanin interactions with transmembrane receptors, enzymes, adhesion molecules, and signaling molecules [127]. Specialized membrane domains identification, including rafts, TEMs, and caveolae, represented a major change with respect to the classical fluid mosaic model and has brought a major breakthrough in cell biology [125].

As the microscopy techniques and florescent labeling developed, many experimental observations suggested that membrane proteins having a cytosolic domain can collide non-specifically with the underlying actin skeleton (fences) in the cytoplasm, which provides obstacles and confines the laterally diffusing membrane proteins in compartments formed by the membrane skeleton meshwork [48], [128], [129] and thus leads to a non-purely free Brownian diffusion of proteins in the cell membrane. Moreover, diffusing membrane proteins may collide with transmembrane proteins bound to the cytoskeleton, which act as pickets. This “picket-and-fence” model (see details in section 3.1.2) was proposed by Kusumi [130] and described a free diffusion of membrane protein occurring inside these compartments with intercompartmental transitions, called “hop diffusion” [131], [132].

In this section, we will discuss in more detail two crucial models of membrane organization: the raft model and the picket-and-fence model.

3.1.1 Lipid raft model

Lipid rafts are currently described as a nanoscale, heterogeneous, highly dynamic, sterol- and sphingolipid-enriched domain that compartmentalizes cellular processes. These small rafts may have the potential to be stabilized and to form larger platforms induced by protein-protein and protein-lipid interactions [133]–[135]. This hypothesis was introduced by Simons and Van Meer in 1987, to explain that glycosphingolipids can cluster in the Golgi apparatus, before being sorted to the apical surface of polarized epithelial cells [118]. Ten years later, Simons and Ikonen [11] proposed the lipid raft theory as a principle of membrane subcompartmentalization,

functioning not only in post-Golgi trafficking, but also in endocytosis, signaling, and many other membrane functions [26]. Nowadays, raft domains, as shown in Fig. 3.2, are usually defined as small, highly dynamic and transient plasma membrane entities that are enriched in saturated phospholipids, sphingolipids, glycolipids, cholesterol, lipidated proteins and glycosylphosphatidylinositol (GPI)-anchored proteins. Enrichment of these hydrophobic components endows these lipid domains with distinct physical properties; these include increased lipid packing and order, and decreased fluidity. Unlike the rest of the phospholipid bilayer, raft microdomains are resistant to solubilization by detergents and thought to be dynamic, with the ability to rapidly assemble and disassemble.

There is a longstanding controversy on the size of raft domains, some reports describing >100 nm sizes and others reporting sizes of a few tens of nanometers. Besides nanometric <100 nm lipid domains, larger domains (*i.e.*>200 nm), also named platforms, were observed in supported membrane bilayers [136] or in giant unilamellar vesicles (GUV) [137]–[142]. Moreover, in the past decade, several groups have presented evidence for micrometric domains in a variety of living cells from prokaryotes to yeast and mammalian cells [143]–[147]. Based on double labeling co-localization, the first observation of micrometric domains in the plasma membrane of a living cell was presented in 2003. It showed that arginine/H+ symporter Can1p-rich areas were stable in growing yeast cells with a typical size estimated to be 300 nm [147]. By applying specific lipid probes on living cells at 37°C, human red blood cells were observed to exhibit plasma membrane submicrometric lipid domains 0.5 μm [148]. A similar domain size was also found in Chinese hamster ovary cells [144]. The hypothesis put forward to explain these differences in raft domain size is that raft domains (10-200 nm) have the potential to form microdomains (> 300 nm) by protein-protein and protein-lipid interaction [134]. Furthermore, membrane lipids are asymmetrically distributed in the inner and outer leaflets, which may further affect membrane organization [108].

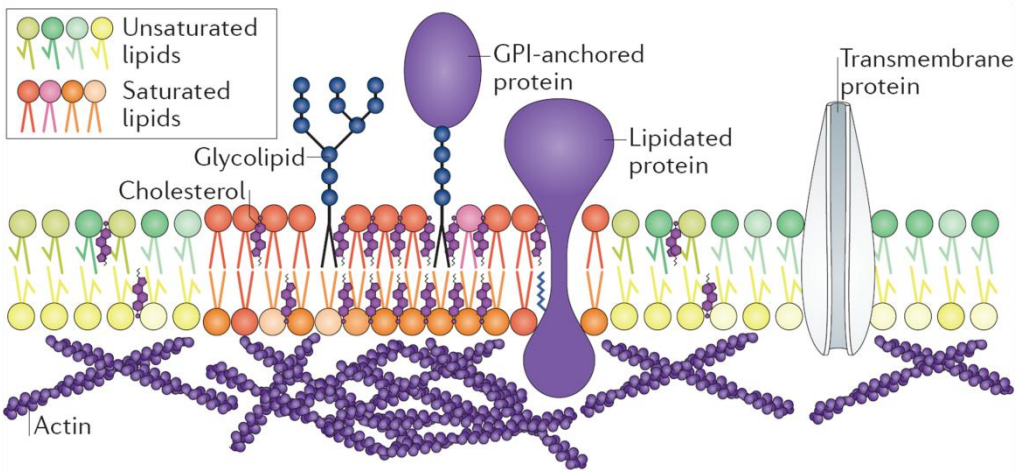

Figure 3.2: Schematic representation of a lipid raft which are enriched in sphingolipids, cholesterol, and GPI-anchored proteins. Figure extracted from ref.[108]

Techniques used to investigate rafts

Over the last few decades, a large number of techniques have been used to study rafts in plasma membranes, all of which have advantages and limitations [149]. These techniques include electron microscopy studies, fluorescence resonance energy transfer (FRET)[150], single-molecule tracking, and super-resolution optical microscopy.

The strongest initial evidence for these non-caveolar microdomains comes from electron microscopy imaging of immunogold-labeled receptors, for example T cell receptors, in fixed cells, where labeled proteins were detected in clusters [151], [152]. Even though the electron microscopy studies can provide nanometric resolution, it lacks specificity and may cause artifacts due to long and invasive sample preparation.

The FRET approach provides a sensitive method to measure molecular proximity by detecting excitation energy transfer between molecules [153]. As described in ref. [146], by applying homo- and hetero-FRET-based experiments, Sharma et al. revealed an unexpected organization in the cell surface of live Chinese Hamster Ovary (CHO) cells where Glycosylphosphatidylinositol-

Anchored Proteins (GPI-APs) are present as monomers and a small fraction (20%-40%) are localized in nanoscale (<5 nm) cholesterol-sensitive clusters.

Single-molecule tracking (SMT) (see details in Section 1.1) techniques refer to a class of techniques that involve direct spatial observation of individual molecules or particles over relatively long time scales (seconds or minutes). By specifically labeling individual molecules in the plasma membrane, this method provides dynamic measurements and a detailed insight into the diffusion properties of membrane receptors, which furthermore make possible to investigate the organization of the plasma membrane. Such studies can reveal confined diffusion of biomolecules in membrane microdomains [7].

Since conventional fluorescence microscopy fails to resolve domains of nanometric sizes, due to the diffraction limit ($\approx 250\ \mathrm{nm}$) (see Section1.1), which is close to the scale of cell membrane microdomains, super-resolution optical microscopy is required to visualize and quantify the organization of molecules inside a membrane microdomain. Super-resolution microscopy techniques based on photophysical properties (photo-activatable, photo-covertible or photo-switchable) of the dyes and single-molecule detection, photo-activated localization microscopy (PALM) and stochastic optical reconstruction microscopy (STORM), were introduced in 2006 [35], [36]. They use stochastic photo-switching fluorophores from an inactive state to an active state. Generally, the photo-activable fluorophores in the field of view are in a dark state. IA specific illumination is then used to bring a few fluorophores in an active (emitting) state' their number being small enough so that the single fluorophores detected are far enough from each other, farther away than the distance determined by the diffraction limit, so that their localization can be determined with high precision (see Chapter 1). By using several cycles of stochastic turning on, imaging and switching off or photobleaching, most of the fluorophores of the sample can be imaged and localized with sub-diffraction accuracy. The obtained positions are then mapped, and the resolution limited only by the localization precision [154].

In the last decade, studies of super-resolution showed the existence of sub-resolution raft domains [16], [155] and raft-associated proteins [156] in the plasma membranes. As described in Ref. [155], using probes with high affinity for the toxin receptors θ-toxin and lysenin receptor

which are located in cholesterol- and sphingomyelin-enriched areas, super-resolution imaging on fixed HeLa cell membranes revealed cholesterol-enriched microdomains with an average radius of 118 nm and sphingomyelin-enriched microdomains with an average radius of 124 nm. The super-resolution techniques provide a powerful tool to visualize the membrane structures and organization of membrane subdomains with a spatial resolution of ≈10 nm in fixed cells [154], [157]. However, PALM/STORM techniques are slow which limits dynamical observations. Moreover, since the current switchable fluorophores are often too dim with a rapid photobleaching, these techniques are still limited for long-term, steady-state structural observations. Real-time single-molecule tracking is therefore required to elucidate the dynamics of membrane microdomains in the live cell.

An extension of single-molecule tracking to high-density labeling has given rise to one branch of super-resolution techniques which includes the initially proposed technique of single-particle tracking PALM (sptPALM). However, in these techniques the trajectories are very short. Therefore, single-molecule tracking at low density with highly photostable labels still has significant advantages and a high potential of contribution to new knowledge in biology and, in particular, in the plasma membrane organization.

3.1.2 Picket-and-fence model

The picket-and-fence model is a concept of cell membrane organization and diffusion proposed by Kusumi and coworkers [48], [128], [130] to explain the movement of unsaturated phosphatidyl-ethanolamine (PE) in rat fibroblasts. This model suggested that the plasma membrane is compartmentalized by underlying actin-based cytoskeleton “fences” giving rise to domains with sizes ranging from 30 nm to 230 nm in cells. They proposed that diffusing membrane proteins may also collide with transmembrane proteins bound to the cytoskeleton which act as “pickets”. This provides an explanation for the much slower macroscopic diffusion of membrane proteins and lipids in the cell membrane compared to the diffusion in artificial, reconstituted membranes. Furthermore, this model also explains the great reduction of the diffusion coefficient or the immobilization upon oligomerization or molecular complex formation [158]. Indeed, it is expected that larger complexes have lower probability of hopping

above the “fences”, which thus hinders their apparent displacement in the membrane. The two

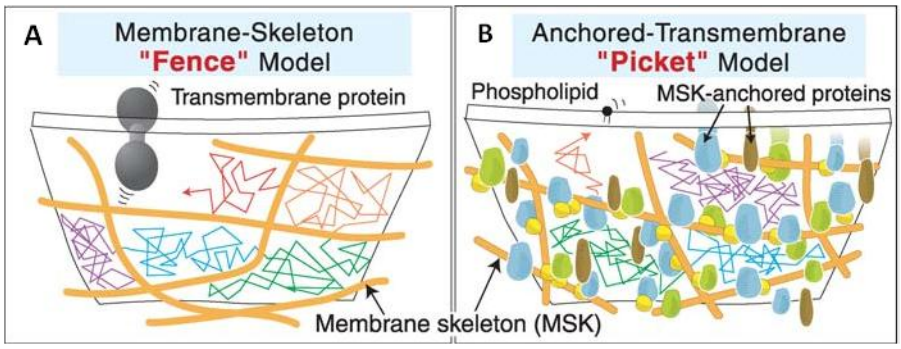

Figure 3.3: Kusumi’s picket-and-fence model. In this model, the actin filament meshwork underlying the membrane creates “fences” for the diffusion of transmembrane proteins (A). Moreover, transmembrane proteins anchored to the membrane skeleton are called “pickets,” as they act as posts along the membrane skeleton fence also hindering the diffusion of both lipid and non-attached transmembrane proteins. Figure extracted from ref [158].

parts of this model, “pickets” and “fences”, are described in more detail below.

The so-called membrane-skeleton “fence” model was proposed after single molecule observations modulating the cytoskeleton or modulating the cytoplasmic domain of transmembrane proteins in cells. In this model, as shown in Fig. 3.3A, the actin-based skeleton meshwork underlying the membrane is directly situated on the cytoplasmic surface of the plasma membrane and compartmentalizes the plasma membrane into many small compartments with regards to the lateral diffusion of membrane proteins. Indeed, transmembrane (TM) proteins with a large cytoplasmic domain can be hindered in their diffusion because they encounter actin filaments giving rise to a corralling effect [158]. TM proteins can hop to adjacent compartments when the distance between the meshwork and the membrane becomes large enough or when this compartment boundary temporarily dissociates

[159]. This so-called “hop diffusion” was confirmed by Monte Carlo simulations which could reproduce the experimental data [160] and by atomic force microscopy observations [129].

However, the cytoskeleton alone cannot confine dynamics of molecules that do not directly interact with it. Fujiwara et al. [131]and Murase et al. [132] found that this hopping diffusion occurred also for phospholipids in the outer membrane leaflet and for membrane proteins possessing only an extracellular domain, whereas the mobility of both these classes of molecules cannot be directly regulated by the actin-based cytoskeleton meshwork. To explain this hop diffusion of outer membrane leaflet phospholipids, an anchored TM-protein “picket” model was proposed [131], [132], [161]. As shown in Fig. 3.3B, in this model, various transmembrane actin-anchored proteins act as rows of pickets posted along the cytoskeleton fence to form effective barriers both for proteins and lipids. Moreover, it was proposed that hydrodynamic-friction-like effects of these immobilized TM protein pickets on the surrounding lipid molecules also play a role against the free diffusion of phospholipids [158]. An important feature of these pickets shows that these transmembrane proteins are not tethered statically to the cytoskeleton but reversibly bind to actin filaments [162] or undergo conformational changes, which may impact their barrier function. Proteins, such as the ezrin/radixin/moesin (ERM) protein family, tethering transmembrane pickets to the underlying cytoskeleton can thus act as a dynamic switch by activating/deactivating the binding of the pickets to the actin filaments [163].

These two models of the plasma membrane can be combined in one, the “picket-and-fence” model. Both membrane proteins and lipids can hop to an adjacent compartment probably when an actin filament temporarily breaks, and/or when membrane proteins have sufficient kinetic energy to cross the compartment boundary [164].

The transferrin receptor (TfR) is a well-known example of a membrane protein confined according to the picket-and-fence model undergoing hop diffusion [161]. We therefore chose it in this work as a protein representative of this type of motion. The transferrin receptor (TfR), is a non-raft protein, solubilized in a more lipid-rich, lower density complex than raft-associated

proteins [165], [166]. As a carrier protein for transferrin, TfR binds to iron-laden transferrin and delivers the iron to cells through clathrin-dependent endocytosis [167], [168].

3.1.3 Other origins of confinement in the membrane

In addition to confinement in raft domains and in picket-and-fence domains, confinement has also been shown to rely on binding of a membrane protein to actin, as in the case of the cystic fibrosis transmembrane conductance regulator (CFTR) Cl- channels [169]. Besides these types of nano/micro-domains, “dynamic protein complex domains” formed by protein-protein interactions have been shown to exist [164]. These include protein nanoclusters like H- or K-Ras clusters [170] with diameters of 3 to 10 nm containing 6-8 molecules or RAS nanoclusters containing approximately 50 Rac1 molecules and may be attached to the actin filaments or not [171]. According to the review [164], caveolae and clathrin-coated pits are also part of these “dynamic protein complex domains”.

3.1.4 Development of model systems

Due to the complexity of membrane organization in real cells, recent works on membrane organization have focused on two novel tools: (i) Multicomponent Giant Unilamelar Vesicles (MGUVs) and (ii) membrane-actin biomimetic constructs. On one hand, MGUV are detached from living cells and can be used to observe a phase separation into a liquid ordered (Lo) and a liquid disordered (Ld) phase as in the simpler few-component GUVs, to determine the transition temperature and other thermodynamic characteristics of these vesicles [173]. The advantage is that the lipid composition of these MGUVs is that of the cell itself and thus contains a large variety of lipids, in contrast to GUVs which typically contain a very limited number of lipids, usually a saturated lipid, an unsaturated one and cholesterol. Nevertheless, these MGUV lack an important element which is thought to help shape the membrane architecture, the interaction with the actin cytoskeleton underlying the membrane [174]. The second tool focuses, on the other hand, on understanding the role of this membrane-cytoskeleton interaction by mimicking it based on biomimetic constructs [175]. Considerable insight into the importance of this

interaction has been gained with such experiments. It has been shown, in particular, that the actin cytoskeleton helps shaping membrane domains [111], [176]. However, this biomimetic tool lacks the variety of lipids and membrane proteins present in real cells. Thus, both these new tools, even though they have provided considerable new insight, offer a partial view of the membrane. In the first case, the system studied lacks the contribution of the actin cortex, whereas the second model system lacks the lipid diversity present in real cells.

Despite the progress in spatial and temporal resolution, as well as in long-term tracking methods, the field of membrane organization remains controversial and quantitative interpretation of direct observations of the dynamic compartmentalization of the membrane is still challenging. In particular, the capacity to extract the confining energy landscape from single-molecule trajectories using Bayesian inference has only been marginally exploited [51], [53].

Moreover, in the present work, we preferred to focus on real cells to promote our understanding of membrane microdomain confining physiologically essential membrane receptors like the EGF receptor in MDCK epithelial cells.

3.2 Receptor Labeling and Tracking

Single particle tracking is a powerful approach to directly investigate the diffusion of proteins in the cell membrane and reveal the complex trajectory of single biomolecular with nanometer precision, while using an optical microscope. In this section we used $Y_{0.6}\,Eu_{0.4}\,VO_4$ nanoparticles to label EGF receptors in the cell membrane and investigate parameters of membrane raft by analyzing trajectories of receptors

3.2.1 EGF Receptor

The epidermal growth factor receptor (EGFR, also known as HER1/ErbB1) is one of the four homologous transmembrane proteins of the HER (ErbB) family of receptor tyrosine kinases. This family also includes HER 2 (ErbB2/Neu), HER 3 (ErbB3), and HER 4 (ErbB4) receptors. These

proteins are cell-surface receptors for the peptide ligand epidermal growth factor (EGF) family and can regulate a multitude of biological processes including cell proliferation, cell motility, and differentiationref. EGFR, in particular, is commonly unregulated in various types of cancer such as breast cancer, head and neck cancer [1], [2] and is therefore a major target for the current and future pharmacological treatment (e.g. Erlotinib, Osimertinib, Rociletinib,…) of these diseases [177], [178].

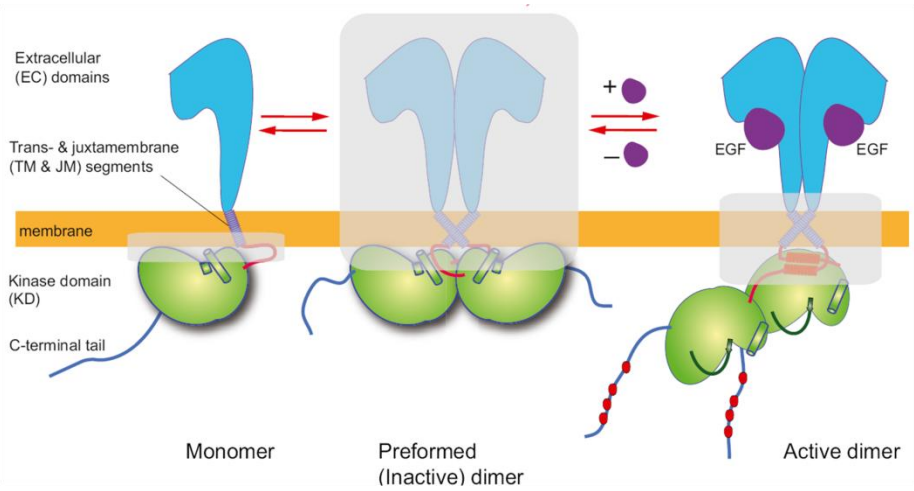

Figure 3.4: Schematic representation of the structure of an EGFR monomer (left), EGFR inactive dimer (middle) and EGFR active dimer (right) on the cell membrane. Figure extracted from ref. [179]**.**

As shown in Fig. 3.4, EGFR is a transmembrane protein containing an extracellular domain, a transmembrane segment, a cytoplasmic tyrosine kinase domain, and a carboxy-(C-)terminal tail. The EGF ligand can bind to the extracellular domain and thus promote receptor dimerization which activates the intracellular tyrosine kinase domain leading to phosphorylation of multiple sites, and then further activates intracellular signaling cascades [180]. After activation by ligand binding, EGFR receptors cluster over clathrin-coated regions on the plasma membrane, to form endocytic vesicles and are either recycled or sorted to late endosomes and lysosomes, before degradation. As determined by biochemical isolation of detergent-resistant domains and immunofluorescence [3], [4] as well as by experiments on live cells [3], EGFR was shown to exist

within raft domains of cell membrane. Moreover, it possesses an actin-binding C-terminal domain which may bind directly with cortical actin meshwork [5], [181].

EGF Receptor Labeling in Living Cells

Experiments presented in this work, used $Y_{0.6}Eu_{0.4}VO_4$ nanoparticles to label receptors by coupling the receptor ligand to the nanoparticles and then incubating the nanoparticle-labaled ligands with the cells. This approach implies that activated receptors are observed. The nanoparticles were prepared as described in reference[44], [104], [182]. Briefly, we coupled aminopropyltriethoxysilane (APTES) coated europium doped nanopartiles to ε-protoxin produced by *C. perfringens* bacteria (CPεT), α-toxin produced by *C. septicum* bacteria (CSαT), or streptavidin, via the amine reactive cross linker Bis (sulfosuccinimidyl) suberatate (BS3). For EGF-NPs and Transferrin-NPs, We incubate the NPs-streptavidin complex with biotinylated EGF (Thermo Fisher) or biotinylated Transferrin (Sigma-Aldrich) at 37°C with a molar ratio of 1:3, which is expected to be large enough to achieve efficient labeling [7], and yet small enough to not cause any cross-linking of receptors. We then remove the free biotinylated ligands by high speed centrifugation of 80 mins at 16,000 rcf.

The cells used in all experiment are Madin Darby Canine Kidney (MDCK) cells. We cultured MDCK cells in Dulbecco's Modified Eagle's medium (DMEM) with 10% fetal bovine serum and 1% penicillin streptomycin at 37°C. Before an experiment, cells were transferred onto glass coverslips and grown overnight. Before the tracking experiment, the medium was replaced by an observation medium (OM) (Hank's Balanced Salt Solution (HBSS) + 10 mM HEPES as a pH buffer) to avoid the autofluorescence of the cell culture medium. Cells on coverslips first were incubated with 0.04 μM NP-labeled CPαT, CSεT, EGF, Trf for 15min at 37°C, and then rinsed three times by observation medium to remove non-bound nanoparticles. With this protocol, the concentration of nanoparticle on cell membrane was kept low to avoid oligomerization and observe single NPs (<10 per cell) as shown in Fig.3.5

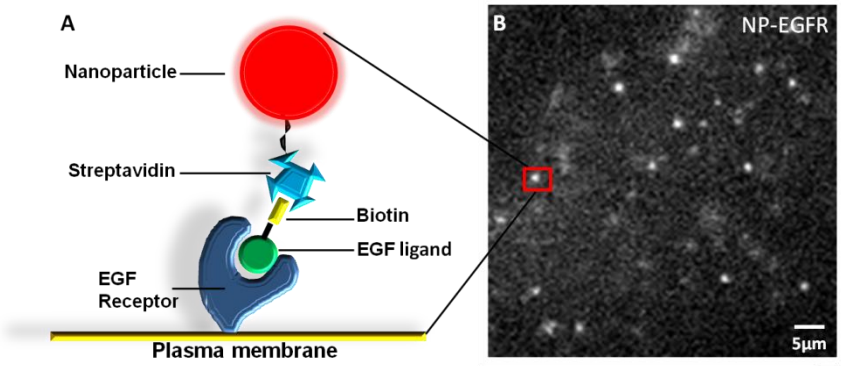

Figure 3.5: Scheme of the conjugate of $Y_{0.6}Eu_{0.4}VO_4$ NP-streptavidin and Biotin-EGF ligand binding to EGFR on the plasma membrane.

Tracking experiment were performed with a wild-field inverted microscope Zeiss AXIOVERT100 (Zeiss Oberkochen, Germany), and an Olympus IX-81 inverted microscope (Olympus Tokyo, Japan) equipped with a 63×, NA=1.4 oil immersion objective and an electron-multiplying charge-coupled device (Quant EM:512SC; Roper Scientific, Trenton, NJ). The $Y_{0.6}Eu_{0.4}VO_4$ nanoparticles are excited with an Ar+ ion laser using 465.8 nm line. The emission of the NPs is then collected through 617/8 filter (Chroma Technology, Bellows Falls, VT). We record series of images at a frame rate rate of 20 Hz (exposure time: 50ms; read out time: 1.3ms) at an excitation intensity of 0.25kW/cm^2 at 37°C. The receptor position in each frame was determined from a Gaussian fit to the diffraction pattern of the nanoparticles with a code written by Silvan Türkcan that uses MATLAB 8.2 (The Math Works, Natick, MA). The localization precision is typically 30 nm.

3.2.2 EGFR and TfR tracking

We thus labeled individual Epidermal Growth Factor Receptors (EGFRs) at the membrane of MDCK cells with a conjugate of $Y_{0.6}Eu_{0.4}VO_4$ nanoparticle-streptavidin (NP-SA) conjugated linked to biotinylated EGF ligand (EGF-BT). This conjugate bound specifically to the EGFR extracellular domain. With this experimental setup, labeling conditions are adjusted so that only 5-10 receptors per cell are effectively tagged. We used white-light transmission imaging to focus on

the cells, then switched to fluorescence imaging and searched upwards for the focal plane where NPs are in focus. The nanoparticle emission signal was only observed at a single focal plane, above the coverslip focal place, which means that NPs labeling EGFR were exclusively present at the apical membrane of the live MDCK cells. We tracked single NP labeled EGFRs and obtained uninterrupted trajectories of up to 240 s (*i.e.* 4600 points with an acquisition time of T_{acq}= 50 ms), due to the absence of blinking. The position of the label in each recorded image of the acquired video was achieved by fitting the processed image without background with a 2D Gaussian, and then a trajectory can be reconstructed (section 1.3). The duration of a typical trajectory is 1 min due to the combination of cell motions and mechanical instabilities of the microscope, which prevent the recording of spatially accurate trajectories for arbitrary long durations. Mechanical drift of the microscope stage during long trajectories gives rise to a linear contribution to the x(t) and y(t) curves, in addition to the confined Brownian motion. This linear contribution was corrected for by subtracting a linear fit of the trajectory data points x(t) and y(t). An example of mechanical drift subtraction in $x(t)$ is shown in Fig. 3.6.

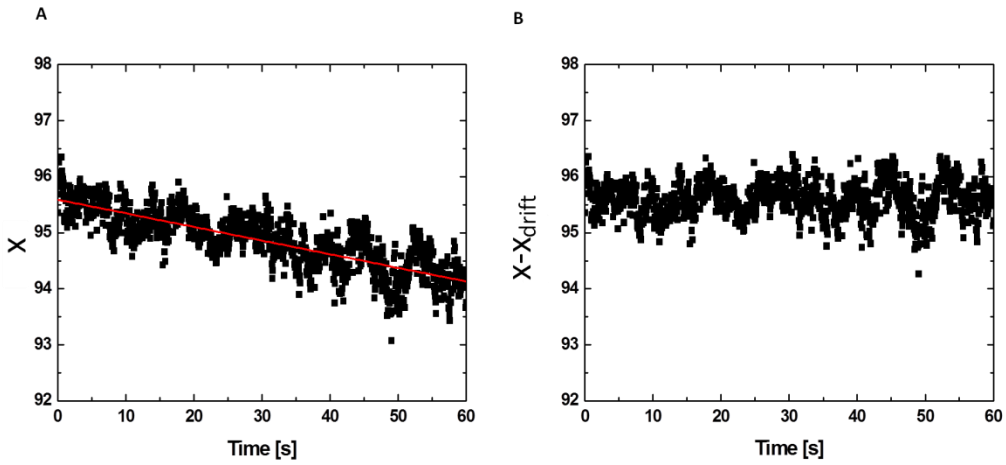

Figure 3.6: A linear fit of the trajectory data points $x_{drift}(t)=at+b$ (A). This drift was then corrected for by subtracting $x_{drift}(t)$ (B).

We only analyzed either trajectory without drift or with eliminated drift as discussed above. A typical single EGF receptor trajectory is shown in Figure 3.7. We observed that all tracked EGFRs

(N=21) experienced Brownian motion confined in a small area with a diameter of a few hundred nanometers.

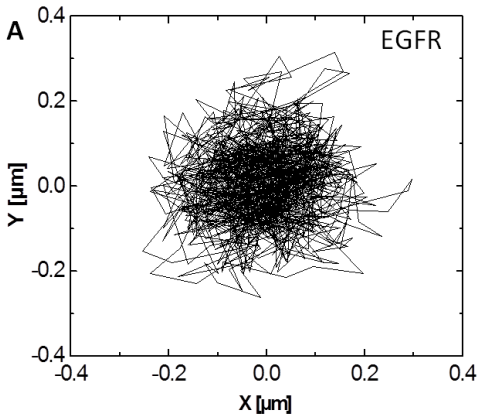

Figure 3.7 Trajectories of a single EGFR at 37 °C was recorded in 1 min. Exposure time: 50ms.

We furthermore labeled Transferrin receptors (TfRs) which are known to be present outside of rafts [128], [183] with NP-SA linked to biotinylated transferrin, and tracked the TfRs in the same way as for EGFRs (see Fig. 3.8).

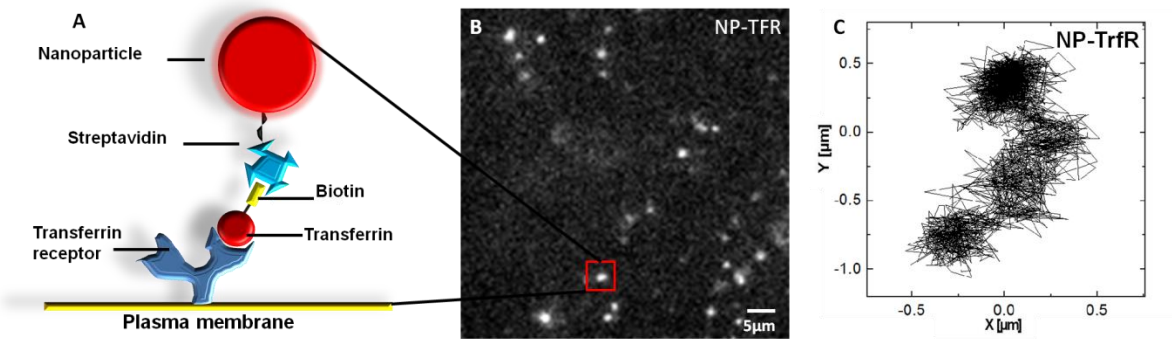

Figure 3.8: (A) Scheme of the conjugate of $Y_{0.6}Eu_{0.4}VO_4$ NP-streptavidin and Biotin-Transferrin ligand binding to TrfR on the plasma membrane. (B) A frame of the image sequence showing NPs probed TrfR on the apical surface of live MDCK cells. (C)

Trajectories of a single TrfR at 37 °C. Exposure time: 50 ms.

A qualitative analysis indicates that the transferrin receptors (TrfRs N= 65) undergo a hop-diffusion as described in [128], [183]. The transferrin trajectories were recorded at 37°C and analyzed by Max Richly [56]. We typically observed confinement in domains of a few hundred nm and 1-5 domain changes generally occurring during an observation time of 3-5 min. This is equivalent to average residence times ranging from approximately 20 to 60 seconds, which suggests that it experiences the type of confinement proposed by the picket-and-fence model [130].

The diffusion behavior of these two types of receptors is quite different even though they both undergo Brownian motion confined in microdomains. In particular, TrfR undergo frequent domain changes which is not the case for EGRF. Bayesian inference analysis has shown that CPεT and CSαT toxin receptors confined in rafts experience a parabolic confinement potential [7]. Based on the literature data, we also expect EGFR to be confined in raft domains [3], [4]. Transferrin receptors on the other hand, are known to be confined according to the picket-and-fence model. Since actin filaments represent well defined barriers for the diffusion properties of TrfR, we expect the confinement potential to be flatter in the domain center and more abrupt at the edge. Bayesian inference analysis of the receptor trajectories is capable of yielding the confinement potential felt by the receptor. However, quantitative tools are necessary to be able to determine if there is a difference between confinement potentials of EGFR and TrfR.

3.2.3 The Diffusion Coefficient and Confining Potential inside the Domain.

To quantitatively characterize trajectories of single EGFR and extract diffusion coefficient and confinement potential controlling the receptor motions, we used the Bayesian Inference method presented by Masson et al. [50] and described in section 1.1, which was initially applied to extract diffusivity and potential fields from confined *Clostridium septicum* α-toxin receptor

(CSαTR) and *Clostridium perfringens* ε-toxin receptor (CPεTR) trajectories in live MDCK cell membranes. This method provides a comprehensive description of the receptor dynamics with the only assumption of a polynomial form for the confinement potential [53].

By applying this method, we first identify the lowest possible order of the polynomial shape of the potential sufficient to account for the experimental data. We started with a fourth-order polynomial, reducing the order and testing if the model still fits the data well. For EGFR, a Kolmogorov-Smirnov (KS) analysis shows that there is no significant difference between fourth- and second-order potentials in the coefficients of the x^2 and y^2 terms Fig. 3.9. Moreover, the linear contributions are negligible compared to the contributions from the quadratic terms.

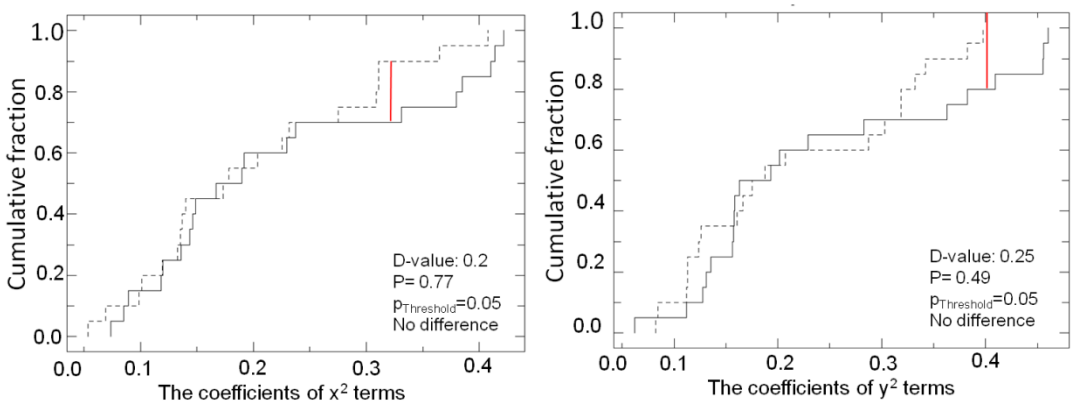

Figure 3.9: Comparison of the inferred potential coefficients of the $x^2$and y^2 terms for EGF receptors in MDCK cells obtained for a fourth- and second-order confinement potential. (The D-value is calculated for the point where he difference between the two cumulative distribution functions is the largest, the P-value is the probability of obtaining a test statistic as the one that was observed, and the red line shows the position of the greatest difference which gives the D-value. If the measured P-value is above the threshold value $P_{Threshold}$, we can confirm that these two distributions are similar.)

We thus described the EGFR confinement by a quadratic potential $U(x,y) = \frac{1}{2}(k_x x^2 + k_y y^2)$, whose stifness is characterized by the radial spring constant k_r, defined as the quadratic

average of the diagonal terms $k_r = (k_x^2 + k_y^2)^{1/2}$. Using Bayesian inference, we determined the diffusion coefficient D_{Inf} and the stiffness of the potential, *i.e.* the coefficients k_x and k_y and the spring constant k_r. The confinement domain surface A was determined as the area of a circular domain containing 95% of the total number of trajectory points.

Concerning the TfR trajectories, they were analyzed using Bayesian inference by Max Richly [56]. In this case, a 4th order potential was considered because we expect the confinement potential due to the encounter of actin filaments to be flatter in the center and more abrupt at the borders. This assumption does not bias the results. If the confinement potential experienced by TfR were quadratic, the Bayesian inference analysis would find negligible 4th order coefficients.

In order to obtain an unambiguous classification, we then used the decision-tree and the clustering approaches discussed in Chapter 1 to classify EGFR and TfR confinement potentials and examine if these techniques are able to detect differences between these two types of confinement potentials.

3.2.3.1 Decision tree analysis

By applying the Bayesian inference decision-tree classification algorithm [55] (Section 1.4), we examined whether the confinement potentials extracted from the experimental EGFR and TfR trajectories can be classified as 2nd or 4th order potentials. We thus performed this computation both for EGFR and TfR (Figure 3.10) and compared the results with previous data obtained by Türkcan et al. [53] on the raft-associated proteins, CPεT and CSαT receptors. We demonstrated that a large majority (81%) of EGFR is confined by a 2nd-order potential, while the hopping domains of transferrin receptors are mostly 4th-order potentials (83%). The obtained classification for EGFR receptors is similar to the raft-associated toxin receptors, which indicates that they may be present in the same domain type.

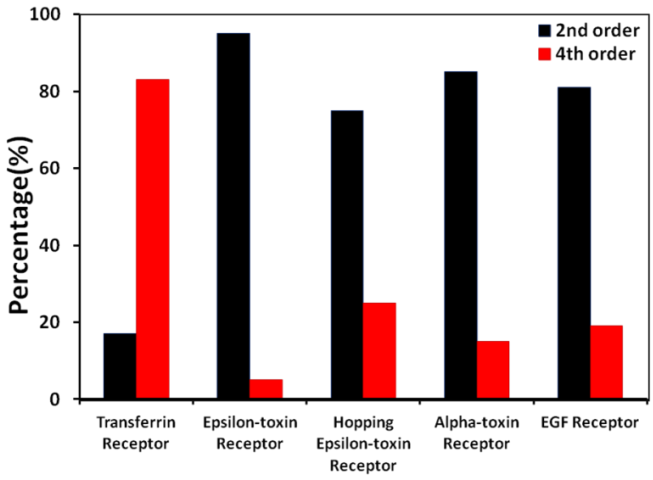

Figure 3.10: Decision tree classified experimental trajectories into 2nd or 4th order. A large majority (81%) of EGFR is confined by a 2nd order potential, similarly, 95% CPεT receptors, 75% hopping CPεT receptors and 83% CSαT receptors are split into 2nd order, while the hopping domains of transferrin receptors are mostly 4th order potentials (83%).

3.2.3.2 Data Clustering analysis

We then used a second approach to classify EGFR and TfR confining potentials based on data clustering. In particular, the aim was to confirm whether EGFR confining potentials cluster together with the raft-associated CPεTR and CSαTR confining potentials, indicating that they may be confined in a same class of microdomains. The previous work done by Max Richly has clearly shown that the data from transferrin receptors are different from the data of CPεT and CSαT receptors: CPεT and CSαT receptors were found in the same cluster whereas TfR were found in a separate cluster [56]. In addition, simulated trajectories either for a confinement by a 2^{nd}-order polynomial potential and or with a potential flat in the center and exponential at the domain border (called "exponential-border potential" in the following text) were respectively clustered with the CPεTR/CSαTR data, or with TfR data. These results thus confirmed those obtained with the decision-tree information criteria approach.

To determine how EGFR data behave in this clustering approach, we combined simulated 2^{nd} and exponential-border potential trajectory data and experimental data for EGFR, CPεTR and

CSαTR, and TfR and plotted all data together by using the t-SNE cluster method only for the confining potential (see section 1.4) as shown in Fig. 3.10. Interestingly, our experimental data can still be clearly separated in two distinct clusters, EGFR data mostly clustering together with CPεTR/CSαTR data and with the simulated 2^{nd} order potential trajectory data (cluster II Fig. 3.11), while TfR data are clustered together with the simulated exponential-border potential trajectory data in a second separate cluster (cluster I). We used a black line added as a guide to the eye to more clearly visualize the two different clusters (Fig. 3.11 and table 3.1). Note that, for the simulated trajectories only 9 2^{nd} order potential data points out of 83 fall outside the cluster II (11%) determined by the black line and only 6 out of 100 fall outside the cluster I (6%) for the case of exponential-border potential data. Concerning the experimental data, of 36 EGFR trajectories, 33 (92%) are found in the same cluster as CPεTR and CSαTR data and the simulated 2^{nd} order potential trajectory data (cluster II). Moreover, 56 out of 65 TfR data (86%) are found in the same cluster as the exponential-border potential data (cluster I).

Table 3.1.Clustering both simulated and experimental data

	Cluster I	Cluster II	Cluster I Percentage	Cluster II Percentage	Total
Simulated trajectories 2^{nd} order potential	9	74	11%	89%	83
Simulated exponential-border potential	94	6	94%	6%	100
CPεTR	10	30	25%	75%	40
CSαTR	2	18	10%	90%	20
EGFR	3	33	8%	92%	36
Transferrin receptor	56	9	86%	14%	65

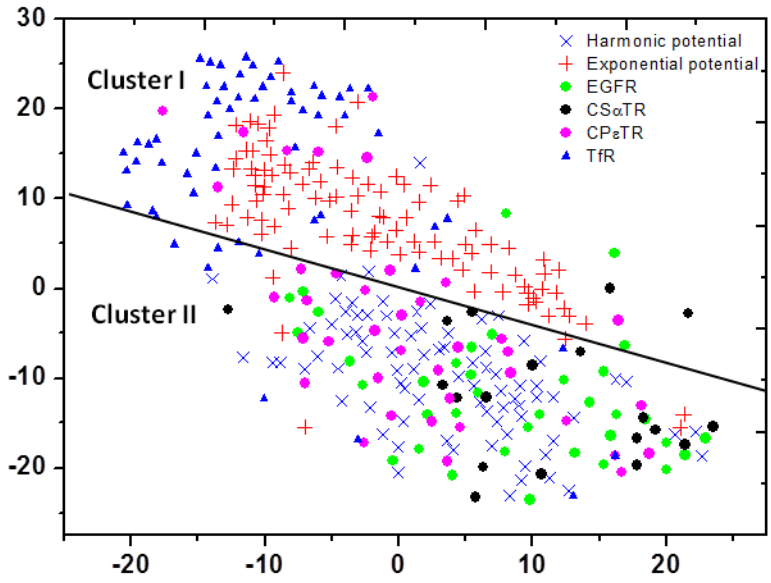

Figure 3.11: t-SNE cluster plot of simulated 2nd-order polynomial and exponential-border potential trajectory data and experimental trajectory data for EGFR, CPεTR and CSαTR, and TfR receptors. EGFR data cluster together with CPεTR and CSαTR data and with simulated 2nd-order polynomial potential data, whereas TfR data cluster together with exponential-border potential trajectory data in a separate cluster. The black line is a guide to the eye to indicate the separation between the two clusters.

Both the decision-tree information criteria approach and the data clustering approach confirm that the potential confining EGFR in its nanodomain is well described by a harmonic potential and that EGFR confinement is of the same type as that of the raft-associated CPεT and CSαT receptors. Moreover, the transferrin receptors experience a distinct type of confinement potential that is better described by a 4th-order polynomial or by an exponential-border potential.

3.3 Confinement of EGF Receptors is Actin-Meshwork and Raft-Dependent

In this section we examine the influence of raft microdomains and of the cytoskeleton on the confinement of EGFR by using pharmacological treatments, cholesterol oxidase to destabilize rafts and latrunculin B to depolymerize actin, respectively. Cells were thus treated with 20 U/ml cholesterol oxidase and 5 µM latrunculin B, respectively to investigate the effect of cholesterol depletion and actin depolymerization on the motion of EGFR.

3.3.1 Raft Destabilization

We first disrupted rafts by incubating MDCK cells at 37°C for 30 min with 20 U/ml cholesterol oxidase (ChOx). Cholesterol oxidase is known to catalyzes the reaction of cholesterol and oxygen to produce hydrogen peroxide and 4-Cholesten-3-one thus destabilizing cholesterol-rich raft domains in the membrane [184]. Previous experiments by Silvan Türkcan determined that this ChOx concentration diminishes the cell cholesterol content by 90%. Note that this measurement does not yield the cholesterol reduction in the membrane but in the whole cell. It is however a good indication that the enzyme induces an effect on cells.

We recorded EGFR trajectories before and after incubation with ChOx at 37°C and analyzed the trajectories with Bayesian inference to infer the diffusion coefficient and the coefficients of a harmonic confining potential. The potential stiffness could then be determined as explained in Section 1.4. When the membrane is cholesterol depleted, we observe a significant reduction of the stiffness of the confinement potential (Fig. 3.12 A and Table 3.2) and an increase of the diffusion coefficient. After 30 min of treatment at 37°C, the average spring constant reduced from $< k_{r-EGFR} >$=0.67±0.08 pN/µm, *N*=21 to $< k_{r-EGFR}^{ChOx} >$=0.12±0.02 pN/µm, *N*=20 (reduced by 83±4%). Correspondingly, the average diffusion coefficient $< D_{inf} >$ increased from 0.065±0.006 µm^2/s to 0.215±0.019 µm^2/s (increased by 70±9%). (Fig. 3.12C and table 3.1). Moreover, we observed a significant increase of the domain area A determined directly from the experimental data (we defined the domain as the area of a circular domain containing 95% of the total number of trajectory points): the average domain area $< A >$ increased from 0.26±0.02 µm^2 to 1.46±0.18 µm^2 (increased by 82±12%). Note that all data before and after treatment were obtained on the same day, on the same coverslip. These results demonstrate

the central role of cholesterol in the origin of the confinement. These results are in agreement with previous reports indicating confinement of EGFR in lipid raft microdomains [3], [4].

We plotted these results in Fig. 3.12 together with CSαTR, CPεTR and TfR data previously obtained by my team (Silvan Türkcan and Max Richly) [7], [12], [56] and also summarize them in table 3.2. In total, 65 transferrin, 40 ε-toxin and 20 α-toxin, and 21 EGF receptor trajectories were analyzed in all conditions. It should be noted that the number of points, N, per trajectory used in this analysis was always above 500 and in most cases above 800, which corresponds to a number of points that is high enough to determine the potential stiffness and classify the trajectories using the decision-tree algorithm with sufficient precision [50], [53].

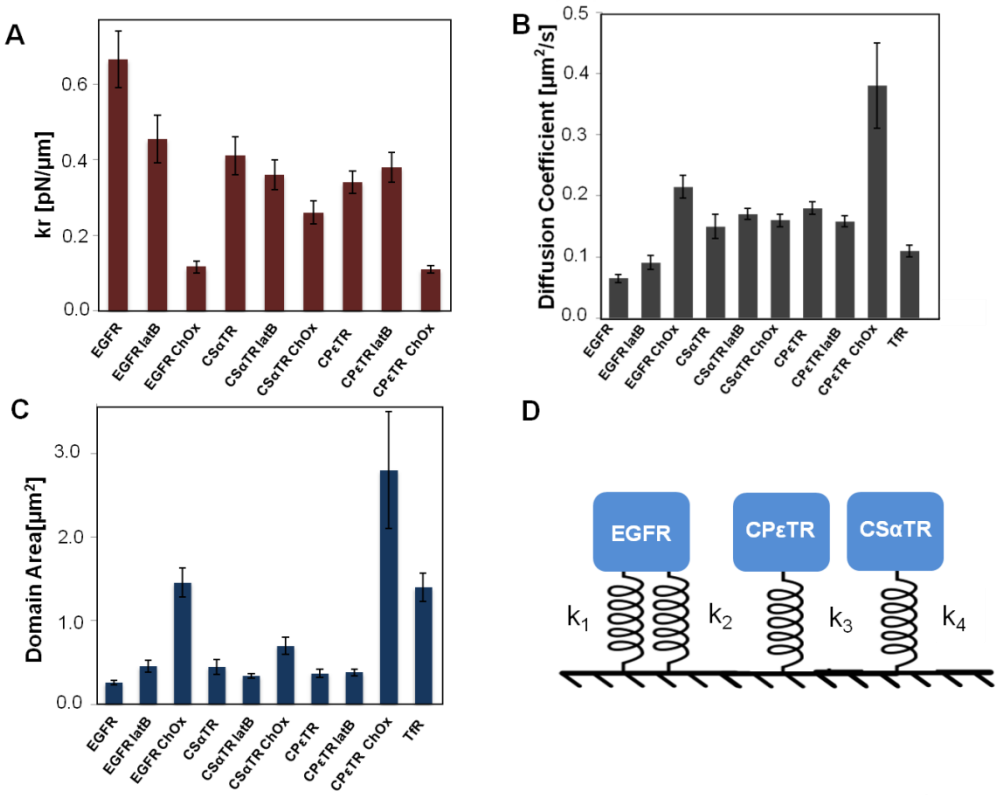

Figure 3.12: Effect of cholesterol depletion and actin depolymerization on the motion of all EGF, CSαT, CPεT and Tf receptors. Cells were treated with 5 µM latrunculin B and 20 U/mL cholesterol oxidase, respectively. Spring constant (*A*), diffusion coefficient (*B*), and domain area (*C*) comparing ChOx and LatB results for all receptors. (*D*) Modeling the EGFR

receptor confinement with a parallel two spring system. The elasticity of the sping confining EGF receptors includes two components k_1 and k_2: k_1 related to the elasticity properties of rafts and k_2 related to the elastic properties of the actin meshwork which is reduced by actin depolymerization. A single spring system with stiffness k_3 and k_4 is sufficient to describe the results for CPεTR and CSαTR, respectively, because the spring constant decreases only upon oxidizing cholesterol, whereas no effect is observed upon actin depolymerization.

The comparison between EGFR and CPεTR and CSαTR data on the effect of ChOx are qualitatively similar: we observe for all three receptors a decrease of the potential stiffness, and an increase of domain area. We also observe an increase of diffusion coefficient for EGFR and CPεTR, the effect being negligible for CSαTR. Quantitatively, EGFR and CPεTR show large changes upon cholesterol depletion both for k_r, D and A, whereas the changes for CSαTR are smaller. For CPεTR, after oxidizing the rafts with cholesterol oxidase, $< k_{r-\mathrm{CP\varepsilon TR}} >$ is similarly decreased from 0.34±0.03 pN/µm (N=42) to 0.11±0.01pN/µm (N=30) (78±1% decrease), the average $< D_{inf} >$ increased from 0.18±0.07 µm^2/s to 0.38±0.07 µm^2/s(increased by 53±23%), and the average $< A >$ increased from 0.37±0.05 µm^2 to 2.8±0.7 µm^2 (increased by 87±7%). These experimental results corroborate those obtained in the previous section with the information criteria and clustering analyses of the confinement potential. Altogether, these results indicate that EGFR and CPεTR and CSαTR are all confined in the same type of membrane microdomains, *i.e.* lipid raft domains.

Table 3.2. Table of latrunculin B and cholesterol oxidase effects on the trajectory and confinement properties of EGFR, CSαTR, CPεTR and TfR in the cell membrane.

		Spring constant [pN/µm]	Domain Area [µm²]	Diffusion Coefficient [µm²/s]	Trajectories
EGFR	Control	0.665±0.075	0.261±0.024	0.065±0.006	n=21
	LatB	0.454±0.063	0.456±0.068	0.091±0.011	n=20
	ChOx	0.116±0.016	1.457±0.176	0.215±0.019	n=20
CSαTR	Control	0.41±0.05	0.45±0.09	0.15±0.02	n=38
	LatB	0.36±0.04	0.34±0.03	0.171±0.009	n=58
	ChOx	0.26±0.03	0.7±0.1	0.16±0.01	n=42
CPεTR	Control	0.34±0.03	0.37±0.05	0.18±0.01	n=42
	LatB	0.38±0.04	0.38±0.04	0.158±0.009	n=65
	ChOx	0.11±0.01	2.8±0.7	0.38±0.07	n=30
TfR	Control	-	1.4±0.17	0.11±0.01	n=65

3.3.2 Disrupting the Actin Skeleton

To determine whether the confinement of the EGF receptors is influenced by the cytoskeleton, we disrupted the actin meshwork by incubating MDCK cells with 500 Nm latrunculin B (Lat B) for 30 min. The latrunculin B sequesters G-actin and prevents F-actin assembly by binding with monomeric actin in 1:1 stoichiometry and thus blocking actin polymerization. In the presence of

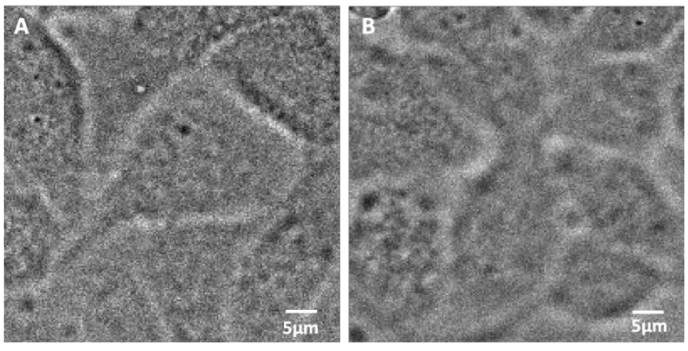

Figure 3.13: MDCK cells before (A) and after (B) treatment with latrunculin B. The cells were incubated for 30 min in 500 nM latrunculin B at 37°C in a medium without serum.

LatB, less actin filaments are present. The depolymerization was observed using a white-light transmission image of the cells (Fig. 3.13). After incubation with LatB, the cells become more round and their 2D surface diminishes. If LatB has no effect on the EGFR motion, this would mean that the confinement is due solely to the raft microdomain environment. If EGF binding to F-actin contributes to the confining potential felt by the receptor, we expect the spring constant to decrease, the diffusion coefficient to increase, and the microdomain area to increase upon actin depolymerization. We recorded EGFR trajectories before and after incubation with LatB and analyzed the trajectories with Bayesian inference to infer the diffusion coefficient and the coefficients of a harmonic confining potential. All the data before and after treatment were obtained on the same day. Figure 3.12 shows the effect of F-actin depolymerization on trajectories of single EGF receptors. After depolymerizing the actin meshwork, the average stiffness of the confining harmonic potential $< k_{r-EGFR} >$ is reduced by 34±11% ($< k_{r-EGFR}^{LatB} >$=0.454±0.063 pN/µm, *N*=20), the average $< D_{inf} >$ increased to 0.091±0.011 µm^2/s, and the average $< A >$ increased to 0.456±0.068 µm^2. This means that EGFR binding to F-actin contributes to the confining potential felt by the receptor. When we incubate with LatB, the actin meshwork becomes less stiff and therefore binding of EGFR to an actin filament leads to a lower stiffness value.

Figure 3.12 and table 3.2 summarize the results and compares them to those obtained for CPεTR and CSαTR. In contrast to EGFR, the depolymerization of the actin meshwork induces no significant change neither for CPεTR nor for CSαTR. This means that, in the case of CPεTR and CSαTR, the confinement results purely from receptor/raft interactions, as mentioned in [53] and that the actin meshwork disruption in EGFR experiments is indeed a specific effect, and not an artifact of any latrunculin induced cell damage.

Combining the information on cholesterol depletion and actin depolymerization, we deduce that both the cholesterol-rich raft environment and the association with F-actin contribute to the EGF receptor confinement. Based on these observations, we can thus model the EGFR confinement with a parallel two springs system as shown in Fig. 3.13D, where the effective elasticity of the confining potential k_r results from the two components k_1 and k_2, describing,

respectively, the interaction with lipids and/or proteins of the raft environment and the interaction with F-actin. In contrast, the confinement of both CPεTR and CSαTR can be described by a single spring model with stiffness k_3 and k_4, respectively, reflecting the interaction between the receptors and the lipid/protein constituents of the raft only.

3.4 Confinement Modeling of EGF, CSαT, CPεT Receptors

The nature of the link between the confinement domain area and the potential is not clear: receptors could either be trapped in a microdomain, in which they experience a spring-like potential or the microdomain could be the observable result of the receptor/lipid-protein and receptor/cytoskeleton interactions creating the potential.

As observed in Fig. 3.7, most of the trajectory areas of raft receptor do not display any preferential direction and the confinement domain is approximately a circle, whose center can be determined by averaging the position of all points. The potentials determined by Bayesian inference are thus isotropic ($k_x \approx k_y$) and the resulting potential is:

$$u(r) = \frac{k_r r^2}{2} \tag{3.1}$$

If we assume that the thermodynamical equilibrium is reached, we can derive the probability density of a position of a receptor as a function of r and of the spring constant k_r:

$$P(r.\theta) = \frac{e^{-\frac{k_r r^2}{2K_B T}}}{Z} \tag{3.2}$$

with Z being defined to ensure that :

$$\int_0^{2\pi} \int_0^{+\infty} P(r) \cdot r dr d\theta = 1 \tag{3.3}$$

In our experiment, we defined the confinement area through the radius of the circle containing 95% of the total trajectory points. We thus expect:

$$\int_0^{2\pi} \int_0^R P(r) \cdot r dr d\theta = 0.95 \tag{3.4}$$

which yields the following scaling law:

$$R \propto \frac{1}{\sqrt{k_r}} \tag{3.5}$$

Consequently, if the confinement results purely from the interactions creating the spring-like potential, we expect that the radius of the confinement domain is inversely proportional to the square root of the spring constant.

The comparison of the experimental values of R and the spring constant value k_r obtained by Bayesian inference for each trajectory presented in Fig. 3.14 for EGFR**,** CSαTR and CPεTR before and after inhibition by ChOx and latrunculin B reveals a good agreement with this prediction (Figure 3.12). This indicates that the confinement is the integrated result of the receptor/lipid-protein interactions: the two parameters k_r and A are thus correlated and describe the same phenomenon.

This implies that the assumption of an equilibrium situation -at least for this feature, the confinement potential experienced by the receptor- is correct. The cell being highly dynamic, this probably means that the motion of the receptor in the average potential over the observation time (typically 1 min) can be described by an effective temperature. This provides an *a priori* confirmation of the equilibrium hypothesis inherent to our Bayesian inference analysis, which uses the fluctuation-dissipation theorem $D(r) = \frac{k_B T}{\gamma(r)}$ [52].

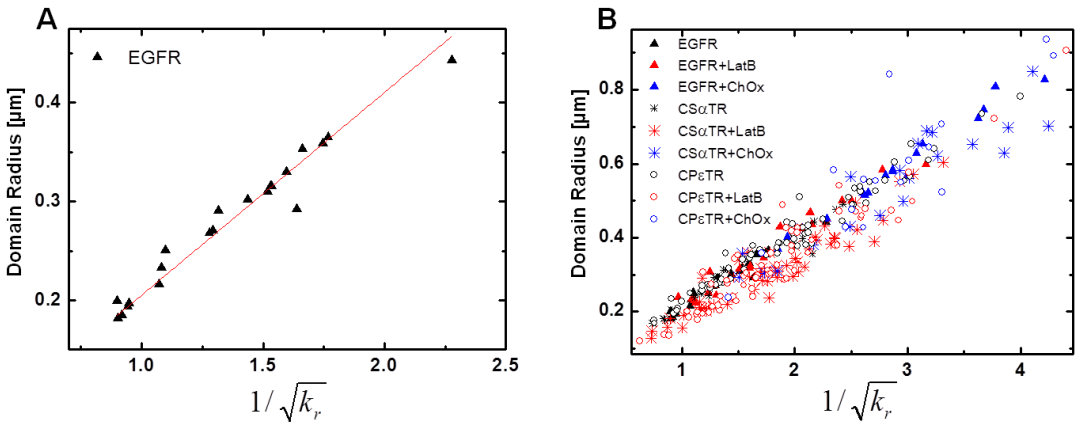

Figure 3.14: The domain radius is proportional to the reciprocal square root of the spring constant describing the confinement potential. (A) EGFR. (B) EGFR, CSαTR and CPεTR data from trajectories in the absence or in the presence of cholesterol oxidase (ChOx) and latrunculin B treatment.

Interestingly, the above description is valid both for the case of raft-associated proteins, like CPεTR and CSαTR, and for membrane proteins that are both raft-confined and attached to the actin cytoskeleton, which indicates a possible generic mechanism for the organization of a large range of receptors at the cell membrane.

3.5 Summary and discussion

In this chapter, we introduced models of membrane organization and investigated the characteristics of membrane rafts by analyzing trajectories of receptors with long-term single-particle tracking in the membrane of living MDCK cells.

In order to label EGF receptors, photostable $Y_{0.6}\,Eu_{0.4}\,VO_4$ nanoparticles were used. After labeling, receptors trajectories were recorded and analyzed by Bayesian inference to determine the properties of confinement. EGF receptors in our experiments performed a confined Brownian motion in the cell membrane and the confinement domain surface (determined as the area of a circular domain containing 95% of the total number of trajectory points) was found to be $A: 0.261 \pm 0.024\ \mu m^2$. Furthermore, by applying Bayesian inference, we determined the diffusion coefficient of EGFR $D_{inf-EGFR}$: $0.065 \pm 0.006\ \mu m^2/s$ and the stiffness of the confining potential k_{r-EGFR}: $0.665 \pm 0.075\ pN/\mu m$.

Both the decision-tree information criteria approach and the data clustering approach results (85% and 92% EGFR trajectories were classified as evolving in a harmonic potential, respectively) confirm that the potential confining EGFR in its microdomain is well described by a harmonic potential. Furthermore, data clustering results showed that EGFR confinement is of the same type as that of the raft-associated CPεT and CSαT receptors. Moreover, the transferrin receptors experience a distinct type of confinement potential that is better described by a 4th-order polynomial or by a flat potential with exponential borders.

We studied the effect of a raft destabilizing enzyme ChOx on the confinement of EGF receptors and observed a clear trend towards higher diffusivity and lower confinement. The average spring constant k_{r-EGFR} is reduced by 83±4%. Correspondingly, the average diffusion coefficient D_{inf} is increased by 70±9%. The average A is increased by 82±12%. The similar results obtained for the effect of ChOx between EGFR, CPεTR and CSαTR data confirmed that EGFR and CPεTR and CSαTR are all confined in the same type of membrane microdomains, raft domains.

We further studied the effect of filament actin depolymerization on EGFR confinement. After depolymerizing the actin meshwork, the average stiffness of the confining harmonic potential is significantly reduced and both diffusion coefficient and domain area are significantly increased. This indicated that EGF binds to F-actin which contributes to the confining potential felt by the receptor. When we depolymerize filament actin, the actin meshwork becomes less stiff and therefore binding of EGFR to an actin filament leads to a lower stiffness value.

We thus model the EGFR confinement with a parallel two spring system where the effective stiffness of the confining potential results from the interaction with lipids and proteins of the raft environment and from the interaction with F-actin. In contrast, the confinement of both CPεTR and CSαTR can be described by a single spring model which reflects the interaction between the receptors and the lipid/protein constituents of the raft.

Furthermore, we could thus show that the experimentally observed domain size i) is intimately related to the stiffness of the confinement potential experienced by the receptor and ii) is an “apparent” domain size determined by the fact that the probability of the receptor being located in an area of high potential energy exceeding several times its thermal kinetic energy is negligible. This implies that the experimentally observed “apparent” domain size is not necessarily a relevant parameter for microdomain physical characterization, whereas the confining potential, in combination with the diffusion coefficient, is sufficient to describe all the features of the motion of the confined receptor, i.e. both the forces it experiences in different areas of the microdomain and the resulting “apparent” domain size.

One striking observation of our work is the very limited number of different organizational behaviors of membrane receptors. Notably, toxin receptors and EGFR, though functionally uncorrelated, are organized with very similar properties, as revealed either by our co-clustering observation or our thermodynamics analysis. This point to the possible existence of a limited number of membrane receptor confinement mechanisms, whose further exploration could lead us to the realization of a comprehensive typology or “atlas” of membrane nano-organization processes.

Chapter 4
Receptor/Microdomain Interactions with the Actin Cytoskeleton Probed by a Hydrodynamic Force

In chapter 3, we have studied and compared the motion type of raft-confined receptors (CPεTR, CSαTR and EGFR) and non-raft-associated receptors (TfR) in the membrane of living cells. By quantitatively determining the shape of the potential to which confined membrane proteins are submitted, we identified a signature of the association in rafts. Different receptors, such as toxin receptors or EGFRs, all associated to rafts encounter indeed the same kind of confinement, leading to the same motion type, *i.e.* diffusion in a quadratic potential. Remarkably, this feature is observed for three different receptors, regardless of their nature: indeed it is also observed for EGFR which, in addition to raft confinement, is bound to the actin cytoskeleton. This may be a general feature of proteins confined in rafts but further experiments are required to confirm this. On the contrary, the motion of non-raft-associated transferrin receptors does not present the same behavior and the confinement potential shape is better described by a fourth-order potential. Indeed, for receptors confined by the steric hindrance of actin filaments, we expect the potential energy to be flat in the domain center and more abrupt in the borders of the domain than a second-order potential.

4.1 External Force Application

It is possible to generate an additional external force on the receptor to gain further insight about the organization of the membrane and, in particular, about the interactions between membrane proteins with an actin-binding domain like EGFR, microdomains and the underlying actin cytoskeleton. As described in Chapter 2, an external hydrodynamic force applied on interacting molecules (molecule A and molecule B) in a microfluidic system is a method to investigate interaction between molecules and measure very low k_{off} values. A luminescent nanoparticle ($Y_{0.6}Eu_{0.4}VO_4$) with a radius R labeling molecule B acts as a kind of kite which

amplifies the amplitude of the force, to which the bond between molecule A and molecule B is submitted (see section 2.2.3, Fig. 2.12). In this chapter, the same concept is used to create a force on membrane receptors in single-molecule tracking experiments.

Living cells were cultured in a microchannel and membrane receptors were specifically labeled by single nanoparticles, as detailed in Chapter 3. A flow of liquid across the cell membrane creates a drag force that scales with the hydrodynamic radius of the nanoparticle, as discussed below. Here, luminescent nanoparticles attached to the biomolecule B can serve both as a force amplifier and as a label to visualize the localization of the biomolecule. Thus, the combination of single-receptor tracking with hydrodynamic force application constitutes a powerful tool to probe membrane nano-organization, notably to identify the nature of the interaction between microdomains and the cytoskeleton.

In this chapter, we highlight this possibility by comparing the behavior of two cell membrane receptors under hydrodynamic force at the single-molecule level: raft-associated receptor EGFR and non-raft-associated receptor TfR. EGFRs are associated to raft microdomains and directly interact with the cytoskeleton, while transferrin receptors diffuse freely in the membrane, only limited sterically by actin barriers, according to the “picket-and-fence” model, over which they are expected to possibly irreversibly hop under force application.

4.1.1 Experiment Setup and Cell Culture in Microchannels

To generate a controlled laminar Poiseuille flow on NPs, we grow MDCK cells in a Y-shaped microfluidic system consisting of polydimethylsiloxane (PDMS) closed by a coverslip glass. (Figure 4.1)

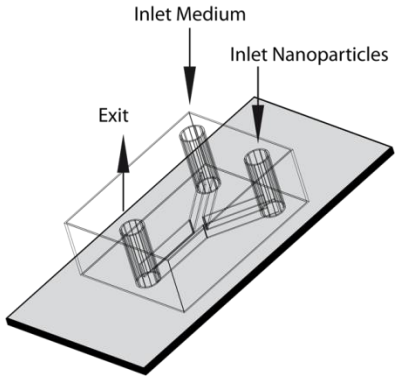

Figure 4.1: Y-shaped microfluidic system for exerting a controlled external force on NPs.

Similarly to what was presented in Chapter 2, the mold for the PDMS channel was prepared by using the dry film photoresist soft-lithography technique [99]. The photosensitive Laminar E8020 Negative Films (Eternal Chemical, Kaohsiung, Taiwan) (32±2 µm thick) were laminated onto a clean glass slide by using the laminator (BIO330D, PEAK) operating at 90°C. The glass slide was then covered with a negative photo mask with the desired channel architecture (Y shape) with a width of 400 µm and exposed in UV light (UV-KUB1, KLOE) to insolate the film on the glass slide through the mask for 30 s to 60 s. The exposed film area is transformed into a solid mold fixed on the glass surface. The uncured photosensitive film was then removed by immersion in a 1% mass concentration carbonate potassium solution.

The PDMS (Dow Corning, Midland, MI) channels were produced by mixing the bulk material and the curing agent with a ratio of 10 to 1. The mixture was centrifuged at 400 g for 3 min to remove bubbles and poured into the previously prepared mold. The mold and the mixture are then placed in the oven for 4 h at 70°C. The baked PDMS channel can be peeled from the mold using a scalpel and plasma cleaned in a vacuum chamber along with a microscope coverslip for 45 s. This treatment in the plasma cleaner leaves free radicals on the surface being cleaned and ensures that they stick together with a weak mechanical pressure (see Fig. 2.10A).

For the tracking experiments under flow force, as described in the previous work of my team [13], we injected cell culture medium into the microchannel 48 hours before cell injection and incubated the microchannels at 37°C to remove gas from the channels. MDCK cells were trypsinated, resuspended and concentrated at a high concentration ca. 10^8 cells/mL, and then carefully injected into the microchannels by using a 1 mL syringe. After 6 hours incubation at 37°C and 5% CO_2, cells adhered to the glass surface. Two connecting tubes (Adtech with 0.56 mm inner diameter) were then inserted into the two inlets of the microchannel, one connected to a Harvard Apparatus pump with a syringe (Analytical Sciences) containing 10 mL observation medium (OM, HBSS + 10 mM HEPES) for rinsing and generating an external flow and one connected to a KD Scientific pump with a syringe containing 500 µL for injecting NPs and inhibitor or enzyme medium (latrunculin B or Arp2/3 or ezrin inhibitor). To avoid bubbles in the microchannel, a liquid droplet was kept on both sides of the tubing while inserting it into the microchannel inlet. Any bubbles passing through the microfluidic system, will indeed tear off the cells by creating a strong surface tension force. Cells are then rinsed with OM at a low flow rate of 5 µL/min. Nanoparticle-ligand conjugates are then injected through the other inlet at a low flow rate of 3 µL/min for 5 min. The nanoparticle conjugates and then incubated with the cells for 30 min at 37°C, as in the tracking experiments of Chapter 3. After incubation, cells are rinsed again with OM to remove free nanoparticles that have not attached to the cell surface.

The microchannel was then mounted on a wide-field inverted microscope Zeiss AXIOVERT100 (Zeiss Oberkochen, Germany) with a 63×, NA=1.4 oil immersion objective, and images were recorded with an electron-multiplying charge-coupled device (EM-CCD) (Quant EM: 512SC; ROPER Scientific, Trenton, NJ). The $Y_{0.6}Eu_{0.4}VO_4$ nanoparticles were excited with an Ar^+ ion laser using the 465.8 nm line, and the emission of the NPs is collected through a 617/8 interference filter (Chroma Technology, Bellows Falls, VT). We recorded series of images at exposure time: 50 ms (read out time: 1.3 ms) and an excitation intensity of 0.25 kW/cm^2. Experiments with cells are performed in a cage incubator at 37°C. The receptor motions were then tracked at the focal plane of NPs located at the upper surface of the cells, under external flow force generated by the Harvard Apparatus pump with OM at 5, 10, 20, and 30 µL/min.

Note that these flow rates create only weak forces on the cells. Indeed, control experiments described in the previous work of my team [13] used labeling of the microtubule skeleton and fluorophore-labeled GM1 receptors which are localized in rafts in the cell membrane. In both control experiments, the microtubules and the raft microdomains moved only slightly due to the liquid flow (on average 0.36±0.06 µm (N=10) and 0.34±0.03 µm (N=20 on 6 cells) respectively) for a flow of 30 µL/min) [13], which established that the flow force only shifts the cells by a negligible distance.

For experiments involving incubation with inhibitors or enzymes, we injected, following incubation with the NPs, OM containing 500 nM latrunculin B (Calbiochem, Millipore, Billerica, MA), or 100 µM of the Arp2/3 inhibitor CK-09935548 (Sigma-Aldrich), respectively, at a low flow rate ca. 3 µL/min and left to incubate for 30 min at 37°C.

4.1.2 Flow Force Determination

When the observation medium is injected with a flow rate Q of 5, 10, 20, or 30 µL/min, the Reynolds number in our rectangular cross-section microchannel is $R = \frac{\rho Q}{4\eta P}$, where ρ and η are respectively the volumic mass and the viscosity of water, and P the cross section parameter, and its value is typically 0.1. In these conditions of a small Reynolds number (R<<1), the flow is laminar and creates a drag force on a spherical nanoparticle that can be described by Stokes's law [185]:

$$\mathbf{F}_{\mathrm{d}} = 6\pi\eta \mathrm{r}\mathbf{v}_{\mathrm{flow}} \tag{4.1}$$

where the drag force $\mathbf{F}_{\mathrm{d}}$ depends on the fluid viscosity η (η_{water}=0.001 Pa·s), the velocity $\mathbf{v}_{\mathrm{flow}}$ of the flow around the NP, and the hydrodynamic radius r of the nanoparticle which can be estimated from the emitted photon number with a precision of 10 % [44] and, in our experiments, has a value ranging from 28 to 58 nm.

In Chapter 2, the flow velocity was determined by using the Poiseuille equation, which describes the laminar flow profile and average flow velocity. We assumed a zero-flow plane on the glass surface and, we then calculated the flow speed at the height of the NP. In this chapter, we

apply a flow force on the receptors in living cells. Because of the presence of the cells in the microchannel, it is difficult to know where the zero-flow plane lies. Therefore, the flow velocity was determined experimentally by using particle velocimetry of unbound particles at the same focal plane as the bound particles, as exposed in Ref. [13]. We measured the distance traveled by several nanoparticles between successive images for a few low flow values, plotted the average speed for four flow values (0.05, 0.1, 0.2, and 0.6 $\frac{m}{s}/\frac{\mu L}{min}$), and used a linear fit of the data to extrapolate to the flow values used in the experiment. The nanoparticle speed for the flow rates used in the experiment is indeed too high to be visualized with our acquisition time. In our experimental conditions, this led to the following conversion parameter:

$$\mathbf{v}_{\text{flow}}/\text{flow rate} = (3.2 \pm 0.8) \times 10^{-4}(\text{m/s})/(\mu\text{L/min}).$$

We thus determine the flow force by experimentally measuring the flow velocity by particle velocimetry and by extracting the particle radius from the collected photon number per unit time. We therefore can control and estimate the force applied through the flow rate in the microchannel.

4.2 Elastic Behavior of CPεT and EGF Receptors under Flow Force

As described in chapter 3, we have studied CPεT toxin receptor and EGF receptor trajectories to investigate the cell membrane organization. The results showed that the confinement of CPεTR is raft-dependent, and confinement of EGFR is both raft- and actin meshwork-dependent. To further reveal the organization of the cell membrane and the interactions between the actin meshwork and rafts or between the actin meshwork and the receptor itself, we generated an external force on receptors using a flow force in a microchannel.

As discussed in section 4.1.1, the flow force acting on the cells is very weak and displaces the cells by 0.36±0.06 μm (N=20 on 6 cells) for a flow of 30 μL/min [13]. The interest of this technique is that, in contrast to the cell itself, the receptor bound to the nanoparticle

experiences a much larger force value due to the amplification related to the nanoparticle radius.

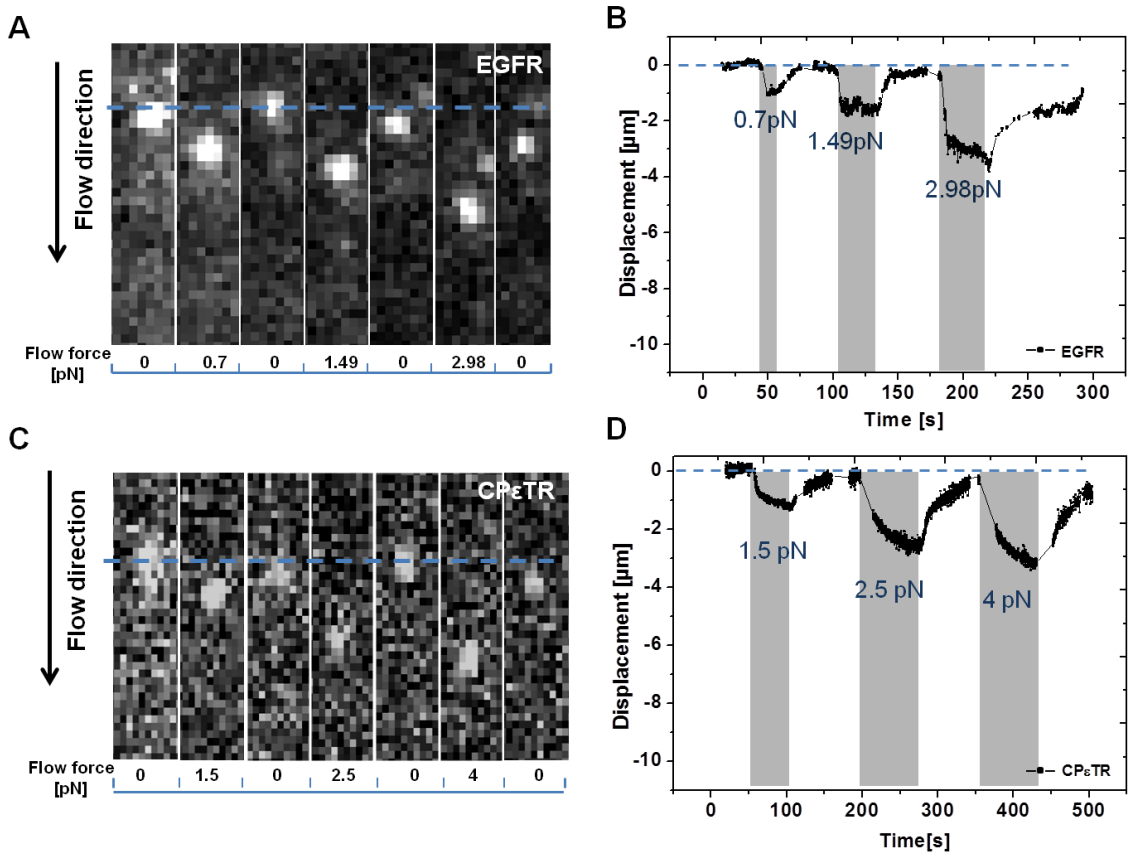

Figure 4.2: Receptor displacements over time for a series of different flow forces. (A) and (B). Elastic behavior of an EGF receptor under a series of flow forces (rates) of 0.7 (5), 1.49 (10), and 2.98 pN (20 µL/min). Note that in each case the force was determined taking into account the radius of each specific nanoparticle. For some time frames the nanoparticle moves too fast to be able to determine its position precisely (see t=200-215 s and t=355-365 s in B)). Excerpts of the recorded movies for the CPεT and the EGF receptor are shown in (A) and (C), respectively. (C) and (D). Displacement of a CPεT receptor for several cycles of hydrodynamic force application. A series of flow forces (rates) of 1.5 (10), 2.5 (15), and 4 pN (30 µL/min) was applied (shaded area). When the flow is stopped, the receptor returns close

to its initial position (blue dashed line). The total displacement for each cycle (see text) rises along with the increase of flow force (B).

We then tracked the motions of CPεT receptors and EGF receptors under the same conditions for a series of flow forces, and reported displacements of the single receptor. As shown in Fig 4.2 A and C, for CPεTR and EGFR, respectively, the hydrodynamic drag force is turned on at t=0 s, the force acting on the NP drags the receptors which start to move inside the membrane and then reach an equilibrium position in approximately 50 s. The shaded areas in Fig. 4.2B and D show the receptor motion during the flow force application. After the flow is turned off (100 s in Fig. 4.2B, 60 s in Fig. 4.2D), the receptor returns close to its initial position (blue dashed line), which is typical of an elastic behavior. Note that in all cases the flow force was calculated from the flow rate for each specific particle size. Therefore, even though the flow rate is the same, the flow force may be different depending on the particle size.

We observe that when nanoparticle-labeled receptors are close to the cell edge, they can only be displaced by the flow force till the cell edge. This shows that the receptors are indeed moving inside the cell membrane and we do not have membrane tubule formation. Moreover, the magnitude of the forces applied in our experiment is at the most 8 pN, which is below the value necessary to create a membrane tubule [13]. In addition, in most cases, we do not see defocusing of the nanoparticle emission during flow force application which would be the case if membrane tubules were formed.

The total displacement is calculated by averaging all recorded positions of the receptor from the frames before the flow started and then subtracting the average position under flow after equilibrium has been reached (Fig. 4.2B and D). We then showed these displacements versus forces curves could be fitted with Hooke's law (Fig. 4.3) and which indicates that the receptor displacement induces an elastic deformation of some kind which pulls the receptor back to its initial position when the flow is stopped. Our Hooke law fits yield the spring constant related to this elastic deformation.

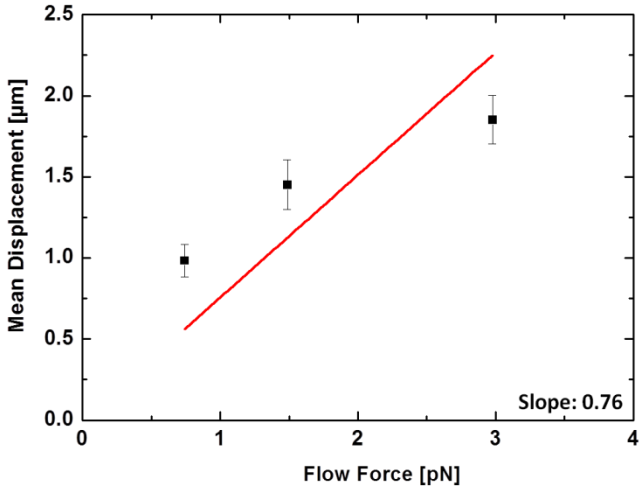

Figure 4.3: The displacement versus flow force for multiple flow cycle curves fitted with Hooke's law. The spring constant can be extracted from the inverse of the slope (spring constant $k = 1.32\ \mathrm{pN}/\mu\mathrm{m}$). The error bars correspond to the standard deviation of the position after equilibrium is reached.

Note that previous work of my team showed that the domain radius and confinement potential of CPεTR extracted using Bayesian inference did not change during the application of the flow [13]. This implies that the receptor does not leave the raft platform it is confined in, and that it is displaced through the membrane along with the confining microdomain. However, during the fast motion of the receptor in the beginning of a flow force application cycle, the localization precision is lower and the receptor may hop from one confining microdomain to an adjacent confining microdomain before it reaches equilibrium. Nonetheless, in the absence of hydrodynamic force, the probability of hopping events is very low [55].

By plotting the mean displacement versus the applied force $F_d = -k\Delta x$, we investigated the mechanical behavior of EGFR/membrane microdomain (MM) complexes (see Figs. 4.2 A,B). The traction of EGFR/MM displays an elastic behavior for forces of 0.7, 1.49 and 2.98 pN, with an average spring constant of k_{EGF} =1.4±0.6 pN/µm (N=15). Note that this spring constant

k should not be confused with the stiffness k_r of the potential energy landscape confining the receptor.

Moreover, we investigated the displacement of CPεT receptors (see Figs. 4.2 C,D) and extracted the average spring constant of the elastic force experienced by the CPεTR/membrane microdomain complexes: $k_{\mathrm{CP\varepsilon T}}$ =3.9±1.6 pN/µm (N=5). This value is in agreement with the value of k =2.5±0.6 pN/µm (N=17) found by Türkcan et al. [13].

This elastic deformation behavior may be related to the actin cytoskeleton. Therefore, the next section presents data to verify this hypothesis.

4.2.1 Role of the actin cytoskeleton

The actin cytoskeleton is a complex network of interlinked filaments composed of linear polymers of G-actin proteins. These thin actin cytoskeleton filaments (F-actin) lie directly underneath the plasma membrane and are organized as a dense cross-linked network containing over a hundred actin-binding proteins (ABPs) [186]. This network has been shown to determine diffusion dynamics of certain molecules in the membrane [161]. A central part of the actin network is composed of G-actin forming the filaments and the actin-related protein (Arp) 2/3 complex (Fig. 4.4A), which is also named actin filament nucleator and consists of actin-related protein (Arp) 2, Arp3, actin-related protein complex (Arpc)1, Arpc2, Arpc3, Arpc4, and Arpc5. It has been shown to play an important role during the branched actin-filament network formation. As shown in Fig.4.4B, the Arp 2/3 complex can bind to the side of a mother filament and initiate the growth of a daughter filament, leading to a branched filament network formation. In particular, Arp2 and Arp3 interact with the pointed end of the daughter filament and Arpc2 and Arpc4 make substantial contacts with the mother filament [187].

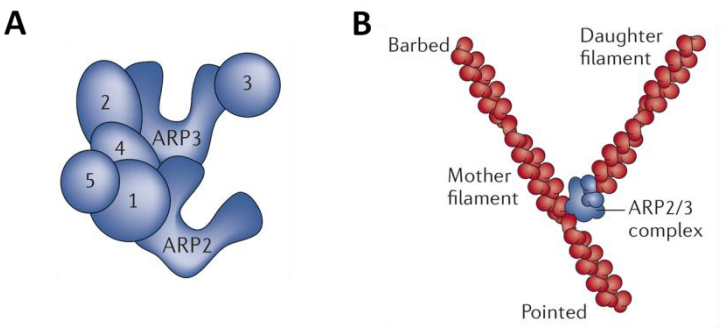

Figure 4.4: Schematic representation of Arp2/3 complex structure. (A) The Arp2/3 complex consists of two actin-related proteins (Arp2 and Arp3) and actin-related protein complex (ARPC)1-5. It can bind to the side of a mother filament and initiate the growth of a daughter filament, leading to the formation of a branched filament network with a regular 70° branch angle (B). Figures are extracted from Ref. [187]**.**

Actin-membrane linkers, including the ezrin-radixin-moesin (ERM) family proteins and myosin-1 motors, are crucial components that tether the actin cytoskeleton to the plasma membrane [188]. The contribution of ERM proteins to actin-membrane linking depends on a conformational change to an active mode in which the C-terminal domain interacts with F-actin and the N-terminal domain interacts with membrane protein ligands [189].

To determine the role of the actin cytoskeleton in the flow force experiments described above, we can therefore use three different approaches by: (i) depolymerizing the actin filaments, (ii) inhibiting the actin filament nucleator (Arp2/3), and (iii) inhibiting actin-membrane linkers like ezrin to probe the role of actin elasticity, of the actin meshwork elasticity, and of the actin-membrane interaction/binding, respectively.

4.2.1.1 Actin filament depolymerization

As described in section 3.3.3, latrunculin B blocks polymerization of F-actin by binding with monomeric actin in 1:1 stoichiometry. It blocks actin polymerization and thus lowers the probability of rafts or receptors binding to an underlying actin filament and moreover decreases the elasticity of the actin meshwork.

Note that less data are available for cells under flow and latrunculin B application because cells adhere less on the glass surface and are more round after cytoskeleton depolymerization (see Fig. 4.6). They are therefore more easily detached by the flow. However, Türkcan et al. have shown that latrunculin B does not modify the cell viability [7], [12].

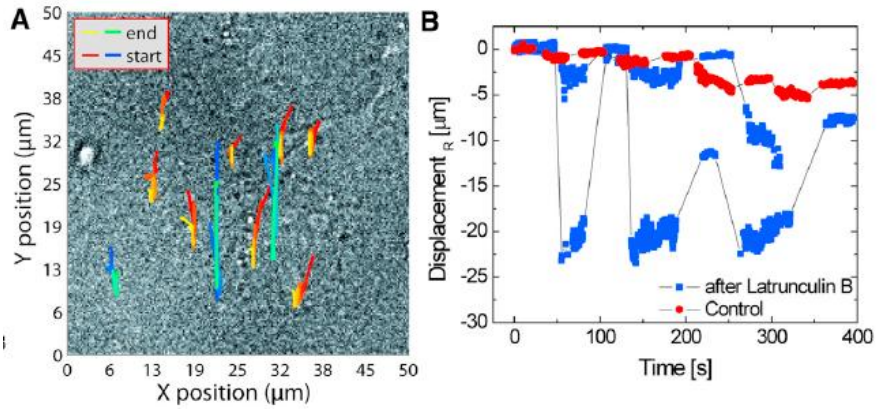

Figure 4.5: (A) Tracking CPεT receptors during flow force application on the same cells before (red-yellow) and after (blue-green) actin depolymerization with Latrunculin B. (B) Trajectories of receptors on the same cells before (red) and after (blue) actin depolymerization. Extracted from [13]**.**

We used latrunculin B to determine its effect on EGF receptor flow force results in a microchannel. As a reminder, the results presented in section 3.3.3 indicated that both the cholesterol-rich raft environment and the association with F-actin contribute to the

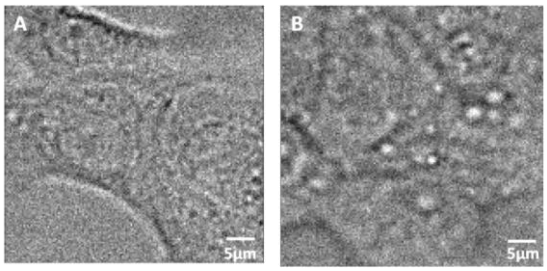

Figure 4.6: MDCK cells before (A) and after (B) treated with latrunculin B. The cells were incubated for 30 min in 500 nM latrunculin B at 37°C in a medium without serum.

confinement of the EGF receptor. The depolymerization was observed using a white-light transmission image of the cells as shown in Fig. 4.6. By disrupting the actin network, MDCK cells were found to undergo a morphological change. After incubation with latrunculin B, the cells

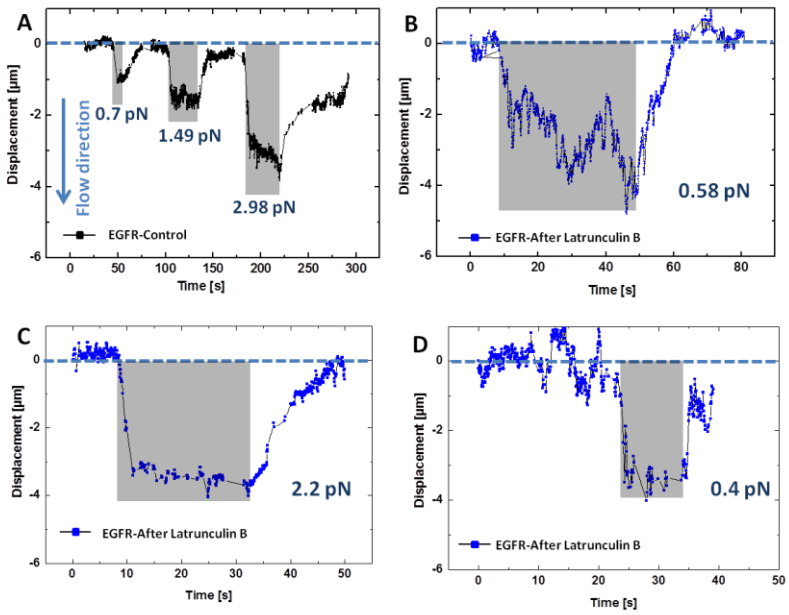

Figure 4.7: Displacement of EGF receptors under flow force before (A) and after (B,C and D) actin depolymerization.

become more round and take up a smaller surface on the glass coverslip.

After incubation with latruculin B and labeling EGF receptors with nanoparticles, the trajectories of EGF receptors are then recorded. As shown in Fig. 4.7B, C and D, by using latrunculin B to depolymerize the actin filament meshwork, EGF receptor trajectories displaced elastically over lager distances compare to the control experiment (Fig. 4.7A) for similar force application. We measured the mean displacement of EGF receptors with and without latrunculin B and, by applying Hooke's law, we observed a significant decrease of the spring constant before (1.4±0.1 pN/µm, N=15) and after depolymerization (0.22±0.04 pN/µm, N=5) for EGFR, *i.e.* 84±16% decrease. This behavior is similar to that observed for CPεTR, as discussed below. These results indicate that the elasticity governing the receptor displacement is indeed actin dependent.

These results are comparable to those obtained for CPεTR by Türkcan et al. [13] (Fig. 4.5). CPεTR were tracked during flow application on the same cells before (red-yellow) and after (blue-green) actin depolymerization (Fig. 4.5A). In the presence of latrunculin B, the CPεTR were displaced over much larger distances and in some cases over the whole cell till the cell border. As for EGFR, this indicated a decrease in the elasticity governing the displacement process. Fitting the displacement versus flow speed curves with Hooke's law yielded an average spring constant of 0.6±0.2 pN/µm (N = 5) compared to a value of 2.5±0.6 pN/µm (N = 17) for control cells (see Fig. 4.5), *i.e.* under the same flow rate and in the absence of latrunculin B [13]. This 80% decrease is similar to what we observed for EGFR.

Based on the results above, the receptor behavior can be interpreted if we consider that, in addition to the drag force due to the flow, there is an additional elastic force equal to the force acting on the NP that is responsible for reaching an equilibrium position. When the force is no longer applied, this elastic force tends to bring the receptor back to its initial position. Moreover, our latB data show that this elasticity is F-actin dependent for EGFR as well as for CPεTR. This means that this additional force is related to a deformation of actin filaments. Either the receptor or its surrounding microdomain is attached to actin filament or the receptor encounters actin filaments and deforms them. We will show below that the second hypothesis can be excluded.

This similar behavior for two different types of receptors (CPεTR are raft-associated and EGFR are both raft-associated and F-actin-bound) speaks for a generic mechanism governing the behavior upon force application.

Incubation with latrunculin B has a strong effect on cells including morphological changes. To confirm the above hypothesis, we next aim at using a molecule that induces an effect only on the elasticity of the actin cytoskeleton. A suitable candidate for this is the Arp2/3 inhibitor, CK548. Since Arp2/3 regulates the branching of the actin meshwork, we expect that the Arp2/3 inhibitor will lead to a less branched, and therefore, less stiff actin network.

4.2.1.2 Inhibition of actin filament nucleator: Arp2/3

Inhibition method

To further confirm the actin-dependent nature of receptor displacement under flow, we used the Arp2/3 inhibitor, CK548 (Sigma-Aldrich)[190], which inhibits the activity of the Arp2/3 complex [187] by inserting itself into the hydrophobic core of Arp3 and altering its conformation. To validate the effect of CK548 inhibition in MDCK cells, we first conducted experiments to determine the optimal CK548 concentration based on immunofluorescence imaging on fixed cells.

Before the labeling process, we prepared formaldehyde (4%) in phosphate buffered saline (PBS), marking solution (0.125% gelatin in PBS), Triton (1%) in marking solution, blocking solution (0.25% gelatin in PBS), DAPI staining solution[191] (Life Technology) for cell nucleus visualization and Rhodamine phalloidin[192] (Life Technology) diluted by 1:200 and 1:40 in PBS, respectively for actin filament visualization. To visualize Arp2/3, we used mouse monoclonal anti-Arp2 antibody [193] (Abcam) and goat anti-mouse secondary antibody conjugated with Alexa Fluor 488 (Life Technology). MDCK cells grown on coverslips were incubated with the formaldehyde solution for 15 min, then with the 1% 100 × Triton solutions for 4 min. The coverslips were rinsed three times with marking solution and incubated with blocking solution for 30-60 min. Then, the coverslips were rinsed again and incubated with anti-ARP2/3 antibody (10 µg/mL in marking solution) at 37°C for 1h (100 µL per coverslip). After rinsing, the coverslips were incubated with marking solution containing the secondary antibody at a concentration of 20 µg/mL and with 1 µg/mL DAPI staining solution at 37°C for 45 min. The coverslips were again rinsed with marking solution before observation. Lastly, a droplet of anti-fading mounting medium (Vectashield) was added on a glass slide and the coverslips were dipped in pure water and placed on the glass slide.

The effect of CK548 inhibition of Arp2/3 in fixed MDCK cells is shown in Fig. 4.8. Arp2/3 (green) In comparison to control cells in Fig. 4.8A, the Arp2/3 fluorescence decreases as the CK548

concentration increases (Fig. 4.8E,I). At a concentration of 50 µM, there is still a large amount of visible Arp2/3 clusters in MDCK cells (Fig. 4.8E). At a concentration of 100 µM (Fig. 4.8I), only few fluorescent clusters of Arp2/3 are observed in the cytoplasm; only a few dots around the cell nuclei are seen in Fig. 4.8L. We attribute the fluorescent Arp2/3 clusters to active complexes which are immobile because they are bound to actin branching points. We expect the inactive Arp2/3 complexes to be unable to bind actin and to therefore diffuse freely in the cytosol. This leads to a decrease of the visible Arp2/3 clusters upon incubation with the Arp2/3 inhibitor. Based on these qualitative results, 100 µM CK548 was chosen as the working concentration in the flow experiments.

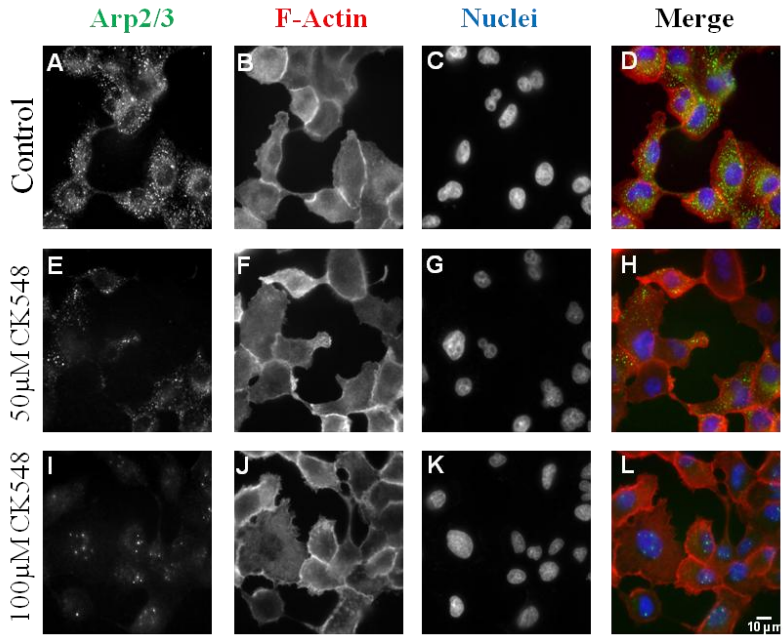

Figure 4.8: Effect of CK548 inhibition on Arp2/3 in fixed MDCK cells. (A-D) Control cells without inhibitor treatment. (E-H) Cells are treated with 50 µM CK548. (I-L) cells are treated with 100 µM CK548. Left column (A,E,I): Arp2/3 fluorescence labeling. Second column (B,F,J): fluorescence labeling of actin filaments. Third column (C,G,K): nuclei staining with DAPI. Right column (D,H,L): Merge of the first three columns. Arp2/3: green. F-actin: red. Nuclei: blue.

Effects of actin elasticity modulation

We then treated cells inside microchannels with 100 µM CK548 to inhibit branching of filament actin and thus reduce the stiffness of the actin meshwork. The comparison of trajectories of the *very same CPεT receptor* before and after Arp2/3 inhibition with CK548 is shown in Fig. 4.9. The displacements after CK548 treatment are significantly larger, which demonstrates that inhibition of Arp2/3 reduces the elasticity responsible for the equilibrium position value under force (*i.e.* the displacement) and for pulling back the receptors close to their initial position after the flow is stopped.

The experiments using latrunculin B and Arp2/3 inhibition both indicate that the elastic force determining the equilibrium position under flow and responsible for pulling back the receptors after the flow stopped is due to deformation of the actin cytoskeleton. This furthermore

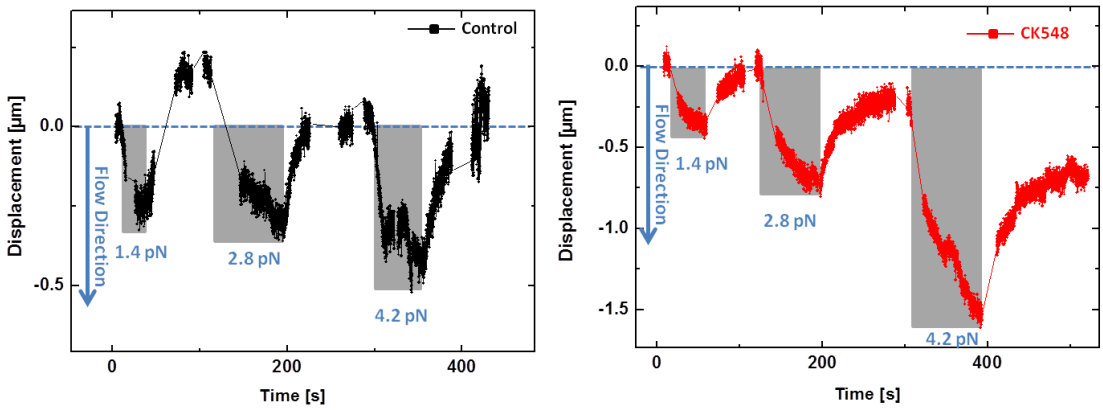

Figure 4.9: Trajectories of the same CPεT receptor before (left, black) and after (right, red) Arp2/3 inhibition. The grey shaded areas indicate the time during which a flow of 10, 20, and 30 µL/min was applied yielding forces of 1.4, 2.8, and 4.2 pN, respectively, for this particular nanoparticle with a radius determined to be 23 nm.

indicates that, by pulling on the CPεT receptors, we probe the rheological properties of the actin meshwork. By fitting the displacement versus flow-induced hydrodynamic force with Hooke's law F=-kΔx, we thus obtain a spring constant, which is related to the elastic modulus of the actin meshwork. In the case of Fig. 4.9, CK548 reduces the spring constant of the actin cytoskeleton

after versus before inhibition from, respectively, 1.6±0.08 pN/µm to 0.9±0.09 pN/µm. We repeated this experiment for N=5 receptors on the same cells before and after Arp2/3 inhibition and found that the inhibitor reduces the actin meshwork stiffness by 50%.

Since the force applied on the receptors leads to deformation of the actin meshwork, we tried to test if the receptor or its confining microdomain is attached to the actin cytoskeleton. We therefore inhibited ezrin, a membrane of the ERM (Ezrin, Radixin, Moesin) protein family, a family which is well known have a membrane-actin cytoskeleton crosslinking function [188].

4.2.1.3 Actin-membrane linkers: Ezrin

Ezrin has been reported to be cross linkers connecting the plasma membrane and the actin cytoskeleton [188]. The ERM family proteins share a highly homologous structure with three domains: a ca.300-residue N-terminal FERM domain, which interacts with plasma membrane proteins through both direct (binding directly to the cytoplasmic tail of certain proteins with single transmembrane domains such as CD43, CD44, CD49, ICAM-1,-2,-3 and syndecan-2) and indirect mechanisms (indirect binding of ERM family members with proteins that contain multiple transmembrane domains, such as the cystic fibrosis transmembrane conductance regulator[194]). The other two domains of ERM family proteins are a ~200 residue central α-helical coiled-coil domain and a ~100 residue C-terminal domain that contains a major F-actin binding site [188].

ERM proteins exist in two states, the dormant state and the active state. In the dormant state, the ERM protein conformation leads to an intermolecular interaction between their FERM and the C-terminal domain, which masks the active site in the FERM domain. In the active state, the conformation opens up by two key steps: N-terminal domain binding to phosphatidylinositol 4, 5-biphosphate and phosphorylation of a conserved threonine 567 (Thr567) at the actin binding site in the C-terminal domain. The phosphorylation of Thr567 reduces the affinity between the C-terminal domain and the FERM domain and the free C-terminal domain can bind to the actin cytoskeleton [195], [196].

In the cases above (incubation with latrunculin B and Arp2/3 inhibitor), we observed elasticity that we attributed to the partial disruption of the actin meshwork. In the following experiments,

instead of disrupting the actin cytoskeleton (LatB) or modifying its elasticity (Arp2/3 inhibitor), we treated cells inside microchannels so as to inhibit the ezrin protein and thus partially prevent the interaction between the plasma membrane and intact actin filaments. The small molecule we used, NSC668394, directly binds to ezrin with low micromolar affinity, inhibits ezrin Thr567 phosphorylation, ezrin-actin interaction and ezrin-mediated motility of cells [195].

We then tracked single ε-toxin CPεT receptors on the cell membrane of MDCK cells in microchannels during the flow force application. The trajectory comparison of a receptor on the same cell before and after the treatment with ezrin inhibitor is shown in figure 4.10A. After treatment with ezrin inhibitor (red curve), under the same flow force, the receptor displacements are much larger than before treatment (black curve), *i.e.* approximately 2 μm before (Fig. 4.10A) and 6 μm after inhibition (Fig. 4.10A), respectively, for a flow rate of 10 μL/min. Other examples of trajectories under a flow rate of 10 μL/min in the presence of the inhibitor yield displacements of 12 μm (Fig. 4.10B), 4 μm (Fig. 4.10C), and 2 μM (Fig. 4.10D). Moreover, the receptor displacements are much faster after ezrin inhibition: in Fig. 4.10B, the receptor reaches an equilibrium position after a displacement of 12 μm after only 0.8 s, whereas, in the control case (Fig. 4.10A black) the equilibrium position is reached after 6 s. Three receptor displacement examples after ezrin inhibition show large and fast displacements already for the lowest flow force, 10 μL/min, (Figs. 4.10A,B,C) and a fourth one (Figs. 4.10D) shows large and fast displacement for the highest flow force, 30 μL/min.

Based on hypothesis (i) discussed above, *i.e.* that the receptor or its surrounding microdomain is attached to actin filaments, and, given the fact that the CPεT receptors are not themselves bound to the cytoskeleton (see section 3.2.2), we can conclude that it must be the raft confining the CPεT receptors that is attached to the actin cytoskeleton. The choice of this hypothesis will be confirmed in section 4.3.

These features indicate a behavior where the raft containing the receptor would have less connection points with the actin cytoskeleton, than in the native conditions. Interestingly, the trajectory in Fig. 4.10C shows almost no displacement back to the initial receptor position after the flow force is stopped, as if the raft-actin meshwork connection were fully disrupted. This

feature is similar to what was observed for freely diffusing transferrin receptors (see section 4.3 below). We here stress that such behavior was never observed neither in the case of LatB actin depolymerization nor in the case of Arp2/3 inhibition.

Moreover, after ezrin inhibition, the receptors are often displaced in a “hopping” manner both during the flow application and during the relaxation process, as explained below. For instance, in Fig. 4.10A, upon application of a flow rate of 10µL/min, the receptor initially reaches an equilibrium position for a displacement of 3.3 µm, and then, after 19 s, is rapidly further displaced to a new equilibrium position corresponding to a displacement of 6 µm. The same “hopping” displacement is observed after the flow is stopped with displacement back to a position 3.3 µm away from the initial position and a subsequent return close to the initial position. A possible explanation may be that the already few connection between the raft microdomain and the actin filaments are transiently detached, which is followed by a free displacement without any restoring force and attachment to other actin filaments.

By applying flow force in this experiment, we demonstrate the effect of ezrin at the single molecule level. These results are still preliminary due to their limited statistics, but they indicate that the receptor displacement depends on the interaction between raft microdomains and the actin cytoskeleton. More experiments are required to interpret more quantitatively this behavior. In particular, it is unclear why, in the examples shown Figs. 4.10A and B, the receptor, after the flow force is stopped, shows a two-step displacement back to a position close to the initial position.

By inhibiting ezrin, we then observed a significantly larger and faster displacement of the ε-toxin receptor under the same flow force, which indicates that ezrin disruption at least partially prevents the raft-cytoskeleton interaction and therefore prevents the deformation of the actin meshwork and the buildup of spring tension. We can deduce that, as a cytoskeletal adhesion protein, ezrin is involved in the connection between rafts and the cytoskeleton. The present experiments indicate that ezrin molecules could be an essential element connecting the CPεTR/membrane microdomain complexes to the cytoskeleton.

To definitively decide which of the two hypotheses proposed above may be correct - *i.e.* (i) is the receptor or its surrounding nanoodomain attached to actin filaments or (ii) does the receptor encounter actin filaments and deform them-, we investigated the behavior of transferrin receptors which are known to be neither confined in lipid-enriched microdomains nor attached to the cytoskeleton.

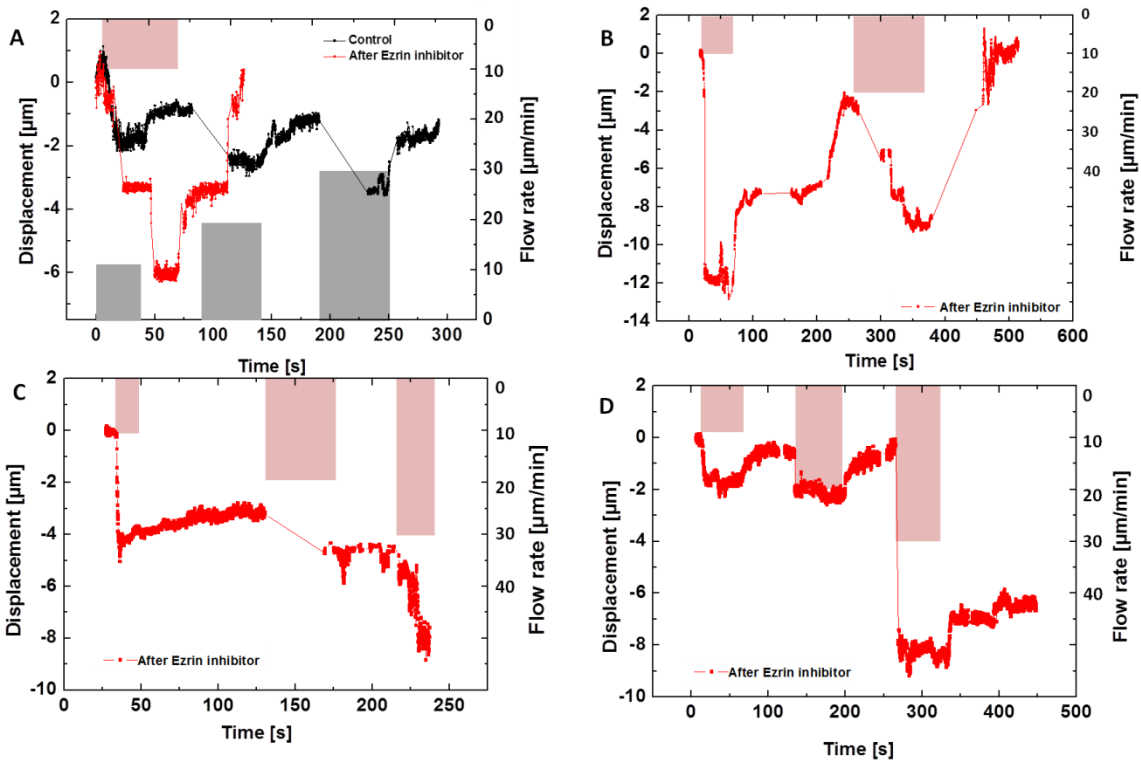

Figure 4.10: The effect of ezrin inhibitor on ε-toxin receptor trajectories under flow force. (A) Receptor displacement before (black) and after (red) ezrin inhibition. (B-D) show three further receptor trajectories obtained after ezrin inhibition. The receptor is displaced over larger distances after ezrin inhibitor application with respect to before incubation with ezrin inhibitor. The flow rates are shown by grey and red shaded areas for the control case and the inhibitor case, respectively. The y-axis on the right of each figure gives the value of the flow rate applied.

4.3 Non-elastic Behavior of Transferrin Receptors under Flow Force

In this chapter, we used luminescent NPs conjugated with transferrin to label single TfR on the cell membrane (as described in section 3.2.2) and investigated the behavior of transferrin receptors under flow force.

The flow experiments with non-raft associated transferrin receptors are shown in Fig. 4.11. When a series of flow forces (0.9, 1.8, and 3.2 pN) is applied, the receptors move until they reach a new equilibrium position. When the flow stopped (F=0), the receptors did not return to the initial position, but stayed close to the equilibrium position. Moreover, the fact that the receptors remain close to their equilibrium position after the flow is turned off reveals a non-elastic behavior. This behavior is drastically different from that of EGF and CPεT receptors and confirms our interpretation that the EGF and CPεT receptor behavior is raft- and actin-mediated.

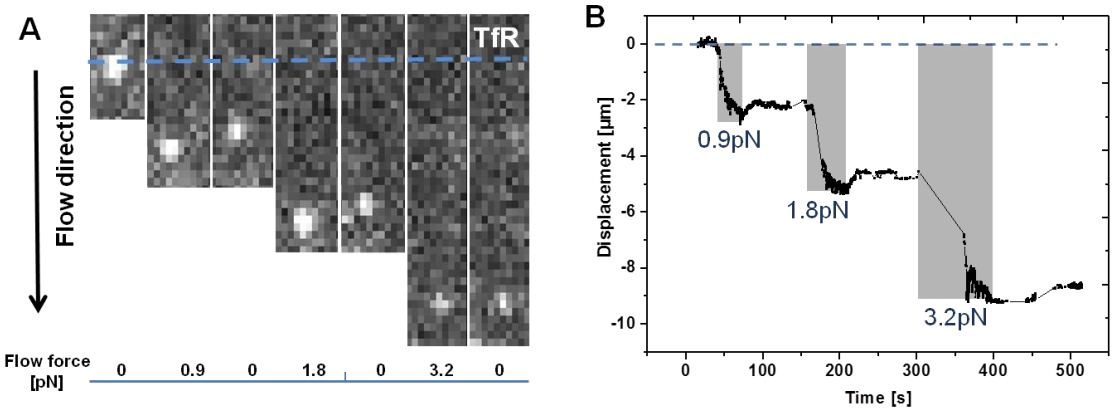

Figure 4.11: Non-elastic behaviors of a non-raft transferrin receptor under a series of flow forces of 0.9, 1.8, 3.2 pN (flow rates are 10, 20, and 30 µL/min, respectively). When the flow stopped, the receptor did not return to the initial position but stayed close to the equilibrium position.

The comparison between transferrin receptor and EGF and CPεT receptor behavior shows that, while the application of a force on single EGFR and CPεTR leads to an elastic deformation of the actin meshwork, the transferrin receptors is first displaced by the force but do not come back to their initial position after force release. This indicates two distinct types of organization that are both cytoskeleton-dependent: EGFR and CPεTR are associated to microdomains submitted to a strong interaction with the cytoskeleton, which cannot be disrupted by forces up to 4 pN (see Fig.4.2), while transferrin receptors diffuse freely in the membrane, only limited by the steric interaction with actin barriers, according to the "picket-and-fence" model [131].

We interpret the behavior of TfR receptors upon flow force as due to irreversible hopping above actin barriers. Indeed, the flow force largely increases the probability of TfR receptors to hop over an actin filament barrier. When the force application stops, this probability goes back to its normal value (see Fig. 3.5) and therefore no hopping is observed for our relatively short observation times.

4.4 Kelvin-Voigt Model of Receptor Displacement

Hooke's law describing elastic behavior can be used to analyze the total displacement as a function of force. Our data, however, show that the receptors need a certain time to reach a new equilibrium position with a force-dependent displacement value, which indicates the presence of viscous effects. We therefore use the standard Kelvin-Voigt model to obtain more information from these viscoelastic trajectories. In this model, the deformation of a visco-elastic material can be represented by an elastic spring and a viscous damper connected in parallel (Fig. 4.12A). In the receptor/raft/cell membrane system we investigated above, the elastic response of our system should mainly be due to the elasticity of the actin meshwork, whereas the viscosity response may be related to both the viscosity of the membrane and the viscoelastic properties of the actin meshwork.

By using the standard visco-elastic Kelvin-Voigt model, when the flow force is applied, the deformation $\varepsilon(t)$ is equal to the ratio of the displacement ΔL to the original length of the spring L_0. The deformation can thus be described by an exponential decay:

$$\varepsilon(t) = \frac{\Delta L}{L_0} = \frac{\sigma}{E}\left(1 - e^{-\lambda t}\right) \tag{4.2}$$

where σ the constant stress, $\sigma = F_d/S$, F_d is the hydrodynamic force applied on the surface S, E is Young's elasticity modulus, and λ is the relaxation rate which is equal to $\lambda = E/\eta$, where η is the system viscosity.

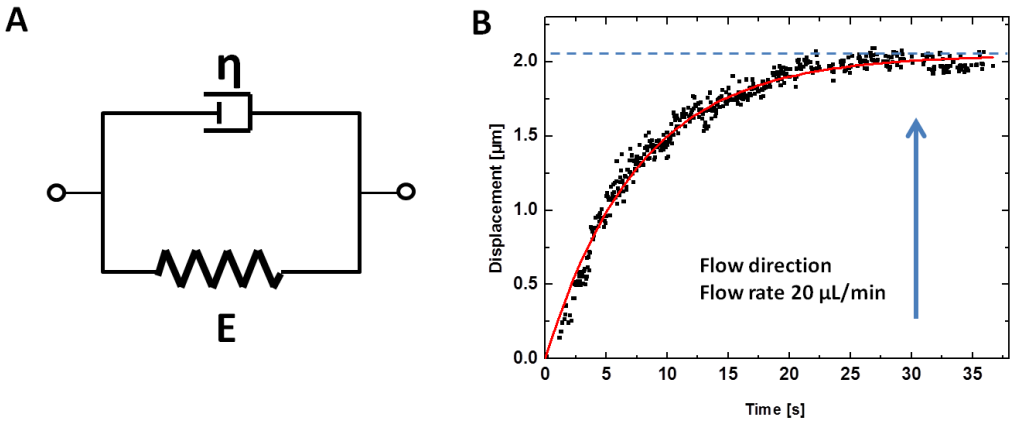

Figure 4.12 (A) **the standard visco-elastic Kelvin-Voigt model** can **be represented by an elastic spring and a viscous damper connected in parallel.** (B) **Displacement of a single CPεT receptor due to a flow rate of 20 µL/min, which starts at 0 s. Note that in this case the flow is applied towards the top; therefore the displacement is positive. The flow force displaces the receptor until it reaches an equilibrium position, where the restoring force of the actin cytoskeleton is equal to the flow force. We fit this displacement evolution with a decaying exponential curve (red line).**

As shown in Fig 4.12, by doing a least-square fit of the deformation evolution curves, we extract the amplitude of the deformation $A = \frac{\sigma}{E} L_0$ and the relaxation rate λ. The amplitude of the displacement A is proportional to the flow rate U. We can then obtain the proportionality coefficient α, which is proportional to 1/E, from $A = \frac{\sigma}{E} L_0 = \alpha \cdot U$. Even though we do not have access to the absolute value of E, we can determine its changes in the different experimental conditions. As shown in Table 4.1, after actin depolymerization by latrunculin B or after

specifically inhibiting Arp2/3 crosslinkers, the extracted changes of α lead to the determination of the elastic modulus changes. E decreases by 65%±38% and 25%±16%, respectively, which is in agreement with the decrease of 76%±30% and 49%±31% of the spring constant k we found above by using Hooke's law. Therefore, the decrease of the system elasticity E due to the disturbance of the actin cytoskeleton is in agreement with our assumption that the measured elasticity is the actin meshwork elasticity and that the spring constant in these experiments is the spring constant of the actin meshwork.

Table 4.1 Cell membrane elasticity and viscosity changes after treatment with latrunculin B and Arp2/3 inhibitor, CK548. Values extracted from CPεT receptor trajectories as shown in Fig. 4.12.

	After Latrunculin B* (N=5)	After CK548 (N=5)
k decrease	**76% ± 30%**	**49% ± 31%**
E decrease	**65% ± 38%**	**25% ± 16%**
η decrease	**50% ± 30 %**	**28% ± 36%**

*Data from Ref. [13]

By determining the changes of the relaxation rate λ, we can extract the changes of η. In the first case (actin depolymerization by latrunculin B), the viscosity coefficient η also decreased by 50%±30%, but was not significantly affected by Arp2/3 inhibition (28%±36%). Assuming that the membrane viscosity does not change in these experiments, we can explain these data, in particular the reduction of η by F-actin depolymerization, by considering that the system viscosity includes two components, the viscosity of the membrane, and the viscoelastic properties of the actin meshwork.

4.5 Discussion and Conclusion

In this chapter, we introduced a powerful method using hydrodynamic force application on a single receptor in the cell membrane. This approach constitutes a valuable tool to probe membrane nano-organization notably to identify the nature of the interaction between microdomains and the cytoskeleton.

The comparison between CPεT, EGF and transferrin receptors shows that the application of a force on single EGFR and CPεTR leads to an elastic deformation of a cell constituent. The receptors are displaced when the flow starts and come back to the initial position when the flow stops. In contrast, the transferrin receptors are first displaced by the force but do not come back to their initial position after the flow force has been stopped.

Depolymerization of the actin cytoskeleton by latrunculin B greatly increased the observed displacements and therefore diminished the elasticity of the deformed cell constituent. Moreover, reduction of the stiffness of the actin meshwork by Arp2/3 inhibitor CK548 also induces a significant decrease of the observed elasticity. We were thus able to determine that the cell constituent that is deformed by the flow force is the actin meshwork.

We previously proposed that EGFR/CPεTR are pulled back to their original position by deformed actin filaments either (i) because they are attached to the actin cytoskeleton or (ii) because of the steric hindrance exerted by actin filaments they encounter. However, hypothesis (i) can be excluded based on previous work [13] which has shown that the actin cytoskeleton depolymerization by latruculin B did not induce a change in inferred diffusion coefficient $\mathrm{D_{Inf}}$ and domain area A for ε-toxin receptor, and the confining potential (*i.e*. the radial spring constant $\mathrm{k_r}$) did not change either.

Based on the qualitatively different results obtained on transferrin receptors under flow, in which the receptors do not move back to the initial position after stopping the flow force, we can also exclude hypothesis (ii). Moreover, as previously documented in [13], the ε-toxin receptors confined in rafts are displaced together with their confining domains during the flow application. We can thus conclude that another component of the raft displaced together with the receptor is responsible for the interaction. When the force is applied on the receptor, the

raft is displaced as a whole, with a strong binding to cytoskeleton through this unknown intermediate, inducing an elastic deformation of the actin meshwork. In this context, the fact that EGFR are probably present in the same type of nanodomains as CPεTR, indicates that EGFR could also be one of the actors mediating the microdomain-cytoskeleton connection.

Therefore, the results above indicate two distinct types of organization that are both cytoskeleton- dependent (Fig. 4.13): EGFR and CPεTR are associated to microdomains submitted to a strong interaction with the cytoskeleton, which cannot be disrupted by a force of up to 4 pN, while transferrin receptors diffuse freely in the membrane, only sterically limited by actin barriers, according to the "picket-and-fence" model [130], barriers which they can irreversibly hop over under force application. Note however, that EGFR can be directly bound to actin filaments through its actin-binding domain, whereas CPεTR are indirectly bound to actin filaments by the intermediate of other raft platform components.

We also showed for the CPεTR-containing microdomains that they are inserted in a visco-elastic environment, satisfyingly described by a Kelvin-Voigt model. One major feature of this visco-elastic behavior is its F-actin polymerization dependence, as revealed by the effect of the latrunculin B treatment. This treatment indeed causes a strong reduction of both Young modulus E and viscosity. Furthermore, the inhibition of Arp2/3, reducing the actin meshwork cross-linking, alters its mechanical elasticity properties, while preserving cell morphology. This treatment induces a significant change of E only: this confirms that the retraction force experienced by the raft microdomain is due to the actin meshwork deformation. In contrast, actin disruption by latrunculin B led to a significant effect both on the elasticity and on the viscosity. These observations indicate that the effective viscosity experienced by the receptors is thus the combination of the viscous contribution of the membrane and of the actin viscosity. All these remarks point to the fact that the force-induced displacement of the receptor is determined by the visco-elastic properties of the F-actin meshwork and of the membrane viscosity.

Altogether, these results both in chapter 3 and chapter 4 present the 3 different modes of membrane organization:

(i) the confinement of CPεTR reflects the interaction between the receptors and the lipid/protein constituents of the raft (Fig. 4.13 left).

(ii) the confining potential of EGFR results from the interaction with lipids and proteins of the raft environment and from the interaction with F-actin (Fig. 4.13 middle).

(iii) transferrin receptors diffuse freely in the membrane, only sterically limited by actin barriers, according to the "picket-and-fence" model (Fig. 4.13 right).

As a conclusion, we demonstrated that our approach using hydrodynamic force is an efficient tool to characterize membrane organization, complementary to single particle tracking (see Chapter 3). Moreover, our approach is a way to probe the local actin rheology and could be used in the future to realize quantitative mechanical mapping of the cell. This could have a strong impact for cell characterization, notably to identify tumoral cells, whose stiffness is known to differ from normal cells [197].

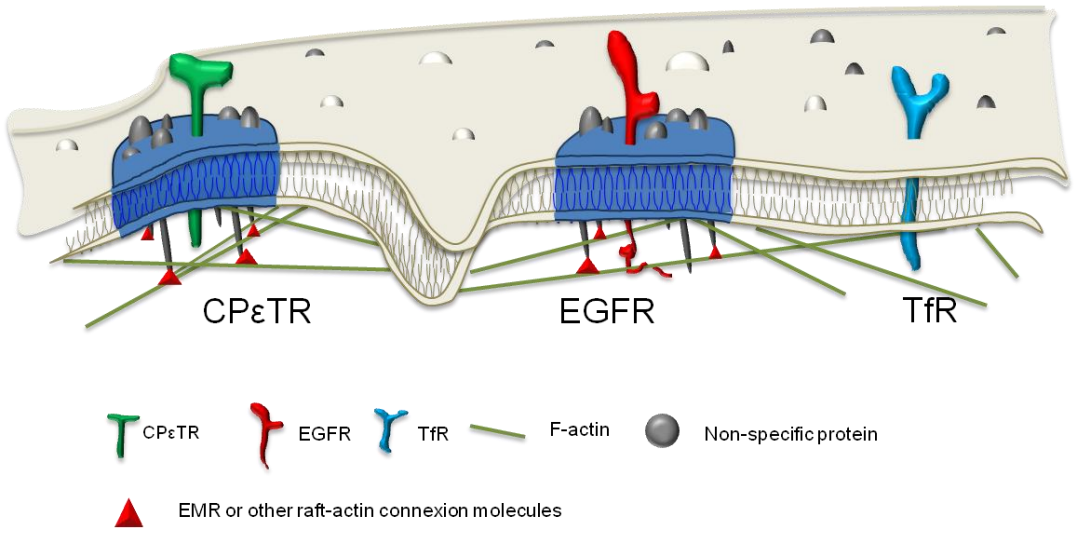

Figure 4.13: **The nano-organization of membrane receptors can result from (i) their confinement due to their direct interaction with membrane lipids (CPεTR, EGFR, left and**

middle part of the figure) or from ii) steric constraints due to actin filaments (TfR, "picket-and-fence" model, right part of the figure). Moreover, some raft-confined proteins can also directly interact with the cytoskeleton (EGFR, middle part of the figure) whereas others are indirectly bound to the actin cytosleteton through molecules like ERM, EGFR, or others mediating binding between raft microdomains and the F-actin meshwork (CPεTR, left part of the figure).

Conclusion and perspectives

In this thesis, we focused on the investigation of the cell membrane organization through long-term single particle tracking and of the receptor/nanoodomain interactions with the actin cytoskeleton probed by a hydrodynamic force. Due to the luminescent properties of the $Y_{0.6}Eu_{0.4}VO_{0.4}$ nanoparticles, i.*e.* high photo-stability without blinking, they can be observed under a hydrodynamic flow by a fluorescence microscope for extended periods of time (> 10 min). EGF, CPεT and transferrin receptors were further tracked both in their local environment in the cell membrane and under a hydrodynamic flow application. At the single-molecule level, $Y_{0.6}Eu_{0.4}VO_{0.4}$-nanoparticle labeling and imaging not only provides a luminescent signal to track receptor motion in the cell membrane, but can also be exploited to amplify the force exerted on a molecule through a liquid flow. This furthermore provides a versatile tool to investigate binding and dissociation kinetics in high affinity receptor-ligand pairs.

Once the data processing of single particles is performed and the trajectories are obtained from the successive label positions in the series of images, a recent analysis approach, Bayesian inference, can then be applied to obtain quantitative information on the receptor motion parameters and, in particular, on the confinement potential experienced by the receptor. Moreover, the shape of the confinement potential provides ways to classify the different motion types of single receptors on the cell membrane. For trajectory classification, the Bayesian inference decision-tree approach is based on a set of information criteria (BIC, AIC and AICc) to distinguish between two different types of confined motion in a 2^{nd}- or in a 4^{th}-order polynomial confinement potential. Another trajectory classification method based on data clustering can classify both confinement potentials and diffusion coefficient maps of simulated and experimental trajectories into two (or more) separate groups. This paves the way to apply systematically this approach to now realize a comprehensive atlas of receptors, based on their organization at the membrane.

We then introduced the existing models of membrane organization and investigated the characteristics of membrane raft domains by analyzing trajectories of receptors, notably EGFR,

with long-term single-particle tracking in the membrane of living MDCK cells (Chapter 3).. After labeling, receptor trajectories were recorded and analyzed by Bayesian inference to determine the properties of the confinement. We demonstrated that EGF receptors performed confined Brownian motion inside a 2^{nd}-order polynomial confinement potential, that we both quantitavely characterized. The decision-tree information criteria approach and the data clustering approach results confirm that the potential confining EGFR in its nanoodomain is well described by a harmonic potential, which is similar to the one observed for uncorrelated toxin receptors. In contrast, transferrin receptors experience a distinct type of confinement potential that is better described by a 4th-order polynomial or by a flat potential with exponential borders: their organization at the membrane is thus controlled through distinct mechanisms

We further investigated the molecular basis for this confinement. The applciation of a raft destabilizing enzyme, cholesterol oxidase (ChOx) or of filament actin depolymerization on the confinement of EGF receptors both induced a clear trend towards higher diffusivity and lower confinement. The average stiffness of the confining harmonic potential is significantly reduced and both diffusion coefficient and domain area are significantly increased. This indicated that EGFR is confined in raft domains and, furthermore, binds to F-actin which contributes to the confining potential felt by the receptor. The confining potential can thus be modeled by a system with two springs in parallel, where the effective stiffness of the confining potential results from the interaction with lipids and proteins of the raft environment and from the interaction with F-actin. In contrast, the confinement of both CPεTR and CSαTR can be described by a single spring model which reflects the interaction between the receptors and the lipid/protein constituents of the raft.

We finally could show that the experimentally observed domain size i) is intimately related to the stiffness of the confinement potential experienced by the receptor and ii) is an “apparent” domain size determined by the fact that the probability of the receptor being located in an area of high potential energy exceeding several times its thermal kinetic energy is negligible. This implies that the experimentally observed apparent domain size is not necessarily a relevant parameter for microdomain physical characterization, whereas the confining potential, in

combination with the diffusion coefficient, is sufficient to describe all the features of the motion of the confined receptor.

Furthermore, we introduced a method using hydrodynamic force application on a single receptor in the cell membrane to probe membrane nano-organization, notably to identify the nature of the interaction between microdomains and the cytoskeleton. The application of a force on single EGFR and CPεTR leads to an elastic deformation of a cell constituent. The receptors are displaced inside the cell membrane when the flow starts and are then pulled back to the initial position when the flow stops. In contrast, the transferrin receptors are first displaced by the force but do not come back to their initial position after the flow force has been stopped. These results can be explained by considering that the raft nanodomains are attached to the actin cytoskeleton and deform it as they are displaced inside the membrane by the hydrodynamic force, whereas transferrin receptors outside rafts are not.

This interpretation is confirmed by the fact that depolymerization of the actin cytoskeleton by latrunculin B greatly increased the observed displacements of EGFR and CPεTR and therefore diminished the elasticity of the deformed cell constituent. Moreover, reduction of the stiffness of the actin meshwork by Arp2/3 inhibitor, CK548, also induces a significant decrease of the observed elasticity. We were thus able to validate that the cell constituent that is deformed by the flow force is the actin meshwork. We thus proposed that EGFR and CPεTR are associated to raft nanodomains submitted to a strong interaction with the cytoskeleton, which cannot be disrupted by a force of up to 4 pN, whereas transferrin receptors diffuse freely in the membrane, only sterically limited by actin barriers, according to the “picket-and-fence” model, barriers which they can irreversibly hop over under force application.

Altogether, these results in Chapter 3 and Chapter 4 describe three different modes of membrane organization and receptor confinement: the confinement of CPεTR is determined by the interaction between the receptors and the lipid/protein constituents of the raft; the confining potential of EGFR results from the interaction with lipids and proteins of the raft environment and from the interaction with F-actin; transferrin receptors diffuse freely in the membrane, only sterically limited by actin barriers, according to the “picket-and-fence” model.

As a conclusion, we demonstrated that our approach using hydrodynamic force is an efficient tool to characterize membrane organization, complementary to single-molecule tracking. Moreover, our approach provides a way to probe the local actin rheology and could be used in the future to realize quantitative mechanical mapping of different cell types. This could have a strong impact for cell characterization, notably to identify tumoral cells, whose stiffness is known to differ from normal cells.

This technique is versatile and can for instance be used to address quantitatively biochemical questions *in vitro*. We thus exploited the hydrodynamic force approach to study biomolecule dissociation between membrane receptors and their pharmaceutical ligands in high affinity receptor-ligand pairs, such as HB-EGF and NP-DTR, where the spontaneous dissociation rate is too small to be measurable (Chapter 2). By labeling with single luminescent nanoparticles with a hydrodynamic radius of 25 nm, we could apply forces on HB-EGF-DTR-NP complexes up to 40 pN. We then demonstrated that we can obtain the experimental characteristic time $\tau_{off}(F)$ for different experimental force values by plotting the number of remaining attached nanoparticles N as a function of time. Subsequently, we can fit the experimental results with Kramer's exponential relation and extrapolate to obtain the dissociation rate$k_{off}(0)$., whose value significantly differs from the one calculated indirectly from k_{on} and K_D values by D. Gillet's team. We thus proposed the existence of multiple bound states between HB-EGF and DTR8, leading to the co-existence of sub-populations with different dissociation time constants. Further investigation, including prolonged observation duration and/or higher flow forces will thus be performed to test this hypothesis.

Our work has nevertheless demonstrated the principle and the efficiency of this technique. In the future, a variation of this technique will be implemented in a Surface Plasmon Resonance (SPR) apparatus, where a hydrodynamic flow is available. In this case, the will act only as amplifiers of the flow force, and a quantitative comparison will be realized between SPR and optical methods. This could lead to the establishment of a new reference method to measure dissociation constants of biomolecule complexes.

Bibliography

[1] A. Citri and Y. Yarden, 'EGF–ERBB signalling: towards the systems level', *Nat Rev Mol Cell Biol*, vol. 7, no. 7, pp. 505–516, Jul. 2006.

[2] Ping Wee and Zhixiang Wang, 'Epidermal Growth Factor Receptor Cell Proliferation Signaling Pathways', *Cancers*, vol. 9, no. 12, p. 52, May 2017.

[3] E. Keating, A. Nohe, and N. O. Petersen, 'Studies of distribution, location and dynamic properties of EGFR on the cell surface measured by image correlation spectroscopy', *European Biophysics Journal*, vol. 37, no. 4, pp. 469–481, Apr. 2008.

[4] M. E. Irwin, K. L. Mueller, N. Bohin, Y. Ge, and J. L. Boerner, 'Lipid raft localization of EGFR alters the response of cancer cells to the EGFR tyrosine kinase inhibitor gefitinib', *J. Cell. Physiol.*, vol. 226, no. 9, pp. 2316–2328, Sep. 2011.

[5] J. C. den Hartigh, 'The EGF receptor is an actin-binding protein', *The Journal of Cell Biology*, vol. 119, no. 2, pp. 349–355, Oct. 1992.

[6] Y. Sako, 'Compartmentalized structure of the plasma membrane for receptor movements as revealed by a nanometer-level motion analysis', *The Journal of Cell Biology*, vol. 125, no. 6, pp. 1251–1264, Jun. 1994.

[7] S. Türkcan *et al.*, 'Observing the Confinement Potential of Bacterial Pore-Forming Toxin Receptors Inside Rafts with Nonblinking Eu3+-Doped Oxide Nanoparticles', *Biophysical Journal*, vol. 102, no. 10, pp. 2299–2308, May 2012.

[8] T. Nagai, K. Ibata, E. S. Park, M. Kubota, K. Mikoshiba, and A. Miyawaki, 'A variant of yellow fluorescent protein with fast and efficient maturation for cell-biological applications', *Nature Biotechnology*, vol. 20, p. 87, Jan. 2002.

[9] F. G. Prendergast and K. G. Mann, 'Chemical and physical properties of aequorin and the green fluorescent protein isolated from Aequorea forskalea', *Biochemistry*, vol. 17, no. 17, pp. 3448–3453, Aug. 1978.

[10] C. Bouzigues, S. Lévi, A. Triller, and M. Dahan, 'Single Quantum Dot Tracking of Membrane Receptors', in *Quantum Dots*, vol. 374, New Jersey: Humana Press, 2006, pp. 81–92.

[11] M. Dahan, 'Diffusion Dynamics of Glycine Receptors Revealed by Single-Quantum Dot Tracking', *Science*, vol. 302, no. 5644, pp. 442–445, Oct. 2003.

[12] S. Türkcan, 'Investigation of the Cell Membrane Architecture by Single-Molecule Tracking of Peptidic Toxins', Ecole Polytechnique, 2011.

[13] S. Türkcan, M. U. Richly, C. I. Bouzigues, J.-M. Allain, and A. Alexandrou, 'Receptor Displacement in the Cell Membrane by Hydrodynamic Force Amplification through Nanoparticles', *Biophysical Journal*, vol. 105, no. 1, pp. 116–126, Jul. 2013.

[14] KiranJ. van der Laan, M. Hasani, T. Zheng, and R. Schirhagl, 'Nanodiamonds for In Vivo Applications', *Small*, vol. 14, no. 19, p. 1703838, May 2018.

[15] S. Ram, E. S. Ward, and R. J. Ober, 'Beyond Rayleigh's criterion: A resolution measure with application to single-molecule microscopy', *Proceedings of the National Academy of Sciences*, vol. 103, no. 12, pp. 4457–4462, Mar. 2006.

[16] A. Small and S. Stahlheber, 'Fluorophore localization algorithms for super-resolution microscopy', *Nature Methods*, vol. 11, no. 3, pp. 267–279, Mar. 2014.

[17] B. Richards and E. Wolf, 'Electromagnetic diffraction in optical systems, II. Structure of the image field in an aplanatic system', *Proceedings of the Royal Society of London. Series A. Mathematical and Physical Sciences*, vol. 253, no. 1274, pp. 358–379, Dec. 1959.

[18] S. F. Gibson and F. Lanni, 'Diffraction by a circular aperture as a model for three-dimensional optical microscopy', *Journal of the Optical Society of America A*, vol. 6, no. 9, p. 1357, Sep. 1989.

[19] N. Hagen and E. L. Dereniak, 'Gaussian profile estimation in two dimensions', *Applied Optics*, vol. 47, no. 36, p. 6842, Dec. 2008.

[20] R. E. Thompson, D. R. Larson, and W. W. Webb, 'Precise Nanometer Localization Analysis for Individual Fluorescent Probes', *Biophysical Journal*, vol. 82, no. 5, pp. 2775–2783, May 2002.

[21] R. J. Ober, S. Ram, and E. S. Ward, 'Localization Accuracy in Single-Molecule Microscopy', *Biophysical Journal*, vol. 86, no. 2, pp. 1185–1200, Feb. 2004.

[22] S. Manley *et al.*, 'High-density mapping of single-molecule trajectories with photoactivated localization microscopy', *Nat Methods*, vol. 5, no. 2, pp. 155–157, Feb. 2008.

[23] R. Tararam, P. S. Garcia, D. K. Deda, J. A. Varela, and F. de Lima Leite, 'Atomic Force Microscopy: A Powerful Tool for Electrical Characterization', in *Nanocharacterization Techniques*, Elsevier, 2017, pp. 37–64.

[24] L. Picas, P.-E. Milhiet, and J. Hernández-Borrell, 'Atomic force microscopy: A versatile tool to probe the physical and chemical properties of supported membranes at the nanoscale', *Chemistry and Physics of Lipids*, vol. 165, no. 8, pp. 845–860, Dec. 2012.

[25] A. Ashkin, 'Acceleration and Trapping of Particles by Radiation Pressure', *Physical Review Letters*, vol. 24, no. 4, pp. 156–159, Jan. 1970.

[26] K. C. Neuman and A. Nagy, 'Single-molecule force spectroscopy: optical tweezers, magnetic tweezers and atomic force microscopy', *Nature Methods*, vol. 5, no. 6, pp. 491–505, Jun. 2008.

[27] G. Binnig, C. F. Quate, and Ch. Gerber, 'Atomic Force Microscope', *Physical Review Letters*, vol. 56, no. 9, pp. 930–933, Mar. 1986.

[28] P. Hinterdorfer, 'High Speed Bio-AFM Reveals Motion of Membrane Proteins Driven by Hydrophobic Mismatch with nm Precision in Label-Free Fashion', *Biophysical Journal*, vol. 99, no. 7, p. 2017, Oct. 2010.

[29] U. Maver, T. Velnar, M. Gaberšček, O. Planinšek, and M. Finšgar, 'Recent progressive use of atomic force microscopy in biomedical applications', *TrAC Trends in Analytical Chemistry*, vol. 80, pp. 96–111, Jun. 2016.

[30] D. J. Müller, J. Helenius, D. Alsteens, and Y. F. Dufrêne, 'Force probing surfaces of living cells to molecular resolution', *Nature Chemical Biology*, vol. 5, no. 6, pp. 383–390, Jun. 2009.

[31] Y. F. Dufrêne, D. Martínez-Martín, I. Medalsy, D. Alsteens, and D. J. Müller, 'Multiparametric imaging of biological systems by force-distance curve–based AFM', *Nature Methods*, vol. 10, no. 9, pp. 847–854, Aug. 2013.

[32] M. Plodinec *et al.*, 'The nanomechanical signature of breast cancer', *Nature Nanotechnology*, vol. 7, no. 11, pp. 757–765, Nov. 2012.

[33] L. M. Rebelo, J. S. de Sousa, J. Mendes Filho, and M. Radmacher, 'Comparison of the viscoelastic properties of cells from different kidney cancer phenotypes measured with atomic force microscopy', *Nanotechnology*, vol. 24, no. 5, p. 055102, Feb. 2013.

[34] A. Touhami, B. Nysten, and Y. F. Dufrêne, 'Nanoscale Mapping of the Elasticity of Microbial Cells by Atomic Force Microscopy', *Langmuir*, vol. 19, no. 11, pp. 4539–4543, May 2003.

[35] J. R. Moffitt, Y. R. Chemla, S. B. Smith, and C. Bustamante, 'Recent Advances in Optical Tweezers', *Annual Review of Biochemistry*, vol. 77, no. 1, pp. 205–228, Jun. 2008.

[36] G. J. Brouhard, H. T. Schek, and A. J. Hunt, 'Advanced optical tweezers for the study of cellular and molecular biomechanics', *IEEE Transactions on Biomedical Engineering*, vol. 50, no. 1, pp. 121–125, Jan. 2003.

[37] J. E. Molloy and M. J. Padgett, 'Lights, action: Optical tweezers', *Contemporary Physics*, vol. 43, no. 4, pp. 241–258, Jul. 2002.

[38] K. Visscher, S. P. Gross, and S. M. Block, 'Construction of multiple-beam optical traps with nanometer-resolution position sensing', *IEEE Journal of Selected Topics in Quantum Electronics*, vol. 2, no. 4, pp. 1066–1076, Dec. 1996.

[39] T. A. Nieminen, N. du Preez-Wilkinson, A. B. Stilgoe, V. L. Y. Loke, A. A. M. Bui, and H. Rubinsztein-Dunlop, 'Optical tweezers: Theory and modelling', *Journal of Quantitative Spectroscopy and Radiative Transfer*, vol. 146, pp. 59–80, Oct. 2014.

[40] A. Ashkin and J. M. Dziedzic, 'Optcal Trapping and Manipulation of Viruses and Bacteria', vol. 235, p. 4.

[41] E. Fällman, S. Schedin, J. Jass, M. Andersson, B. E. Uhlin, and O. Axner, 'Optical tweezers based force measurement system for quantitating binding interactions: system design and application for the study of bacterial adhesion', *Biosensors and Bioelectronics*, vol. 19, no. 11, pp. 1429–1437, Jun. 2004.

[42] M. Andersson *et al.*, 'Using optical tweezers for measuring the interaction forces between human bone cells and implant surfaces: System design and force calibration', *Review of Scientific Instruments*, vol. 78, no. 7, p. 074302, Jul. 2007.

[43] V. Emiliani, D. Sanvitto, M. Zahid, F. Gerbal, and M. Coppey-Moisan, 'Multi force optical tweezers to generate gradients of forces', *Optics Express*, vol. 12, no. 17, p. 3906, 2004.

[44] D. Casanova, D. Giaume, E. Beaurepaire, T. Gacoin, J.-P. Boilot, and A. Alexandrou, 'Optical in situ size determination of single lanthanide-ion doped oxide nanoparticles', *Applied Physics Letters*, vol. 89, no. 25, p. 253103, Dec. 2006.

[45] M. J. Saxton and K. Jacobson, 'SINGLE-PARTICLE TRACKING:Applications to Membrane Dynamics', *Annual Review of Biophysics and Biomolecular Structure*, vol. 26, no. 1, pp. 373–399, Jun. 1997.

[46] R. Metzler, J.-H. Jeon, A. G. Cherstvy, and E. Barkai, 'Anomalous diffusion models and their properties: non-stationarity, non-ergodicity, and ageing at the centenary of single particle tracking', *Phys. Chem. Chem. Phys.*, vol. 16, no. 44, pp. 24128–24164, 2014.

[47] C. Bouzigues and M. Dahan, 'Transient Directed Motions of GABAA Receptors in Growth Cones Detected by a Speed Correlation Index', *Biophysical Journal*, vol. 92, no. 2, pp. 654–660, Jan. 2007.

[48] A. Kusumi, Y. Sako, and M. Yamamoto, 'Confined lateral diffusion of membrane receptors as studied by single particle tracking (nanovid microscopy). Effects of calcium-induced differentiation in cultured epithelial cells', *Biophysical Journal*, vol. 65, no. 5, pp. 2021–2040, Nov. 1993.

[49] J. Fourier, *Analytical theory of heat*. Cambridge, UK,: The university press, 1878.

[50] J.-B. Masson *et al.*, 'Inferring Maps of Forces inside Cell Membrane Microdomains', *Physical Review Letters*, vol. 102, no. 4, Jan. 2009.

[51] M. E. Beheiry, M. Dahan, and J.-B. Masson, 'InferenceMAP: mapping of single-molecule dynamics with Bayesian inference', *Nature Methods*, vol. 12, no. 7, pp. 594–595, Jul. 2015.

[52] H. Risken, *The Fokker-Planck equation: methods of solution and applications*, 2. ed. Berlin: Springer, 1996.

[53] S. Türkcan, A. Alexandrou, and J.-B. Masson, 'A Bayesian Inference Scheme to Extract Diffusivity and Potential Fields from Confined Single-Molecule Trajectories', *Biophysical Journal*, vol. 102, no. 10, pp. 2288–2298, May 2012.

[54] W. H. Press, B. P. Flannery, S. A. Teukolsky, and W. T. Vetterling, *Cambridge - Numerical Recipes in C_ The Art of Scientific Computing, 2nd Ed., Press W.H., Teukols.pdf*, Cambridge University Press,. Cambridge, UK, 1988.

[55] S. Türkcan and J.-B. Masson, 'Bayesian Decision Tree for the Classification of the Mode of Motion in Single-Molecule Trajectories', *PLoS ONE*, vol. 8, no. 12, p. e82799, Dec. 2013.

[56] M. U. Richly, 'Investigation of Toxin-Cell Interactions and Receptor Confinement in the Cell Membrane', Ecole Polytechnique, 2015.

[57] G. Schwarz, 'Estimating the dimension of a model', *The Annals of Statistics*, vol. 6, no. 2, pp. 461–464, 1978.

[58] K. P. Burnham and D. R. Anderson, 'Multimodel Inference: Understanding AIC and BIC in Model Selection', *Sociological Methods & Research*, vol. 33, no. 2, pp. 261–304, Nov. 2004.

[59] A. K. Jain, 'Data clustering: 50 years beyond K-means', *Pattern Recognition Letters*, vol. 31, no. 8, pp. 651–666, Jun. 2010.

[60] V. Estivill-Castro, 'Why so many clustering algorithms-A Position Paper', *ACM SIGKDD Explorations Newsletter*, vol. 4, no. 1, pp. 65–75, Jun. 2002.

[61] A. Coates and A. Y. Ng, 'Learning Feature Representations with K-Means', in *Neural Networks: Tricks of the Trade*, vol. 7700, G. Montavon, G. B. Orr, and K.-R. Müller, Eds. Berlin, Heidelberg: Springer Berlin Heidelberg, 2012, pp. 561–580.

[62] R. Reris and J. P. Brooks, 'Principal Component Analysis and Optimization: A Tutorial', in *Operations Research and Computing: Algorithms and Software for Analytics*, B. Borchers, J. P. Brooks, and L. McLay, Eds. INFORMS, 2015, pp. 212–225.

[63] L. van der Maaten and G. Hinton, 'Visualizing Data using t-SNE', *Journal of Machine Learning Research*, vol. 9, no. 2008, pp. 2579–2605, Nov. 2008.

[64] C. Gil, J. Dorca-Arévalo, and J. Blasi, 'Clostridium Perfringens Epsilon Toxin Binds to Membrane Lipids and Its Cytotoxic Action Depends on Sulfatide', *PLoS ONE*, vol. 10, no. 10, p. e0140321, Oct. 2015.

[65] J. C. Freedman, B. A. McClane, and F. A. Uzal, 'New insights into Clostridium perfringens epsilon toxin activation and action on the brain during enterotoxemia', *Anaerobe*, vol. 41, pp. 27–31, Oct. 2016.

[66] R. J. Falconer, 'Applications of isothermal titration calorimetry - the research and technical developments from 2011 to 2015: Review of Isothermal Titration Calorimetry from 2011 to 2015', *Journal of Molecular Recognition*, vol. 29, no. 10, pp. 504–515, Oct. 2016.

[67] E. Freire, O. L. Mayorga, and M. Straume, 'Isothermal titration calorimetry', *Analytical Chemistry*, vol. 62, no. 18, pp. 950A-959A, 1990.

[68] G. Weber, 'Rotational Brownian Motion and Polarization of the Fluorescence of Solutions', in *Advances in Protein Chemistry*, vol. 8, Elsevier, 1953, pp. 415–459.

[69] J. R. Lakowicz, *Principles of Fluorescence Spectroscopy*, Third edition. USA: Springer, 2006.

[70] L. Lobato, 'Internal dynamics of heme-based sensor proteins studied using advanced time-resolved optical spectroscopy', Ecole Polytechnique, France, 2013.

[71] V. J. LiCata and A. J. Wowor, 'Applications of Fluorescence Anisotropy to the Study of Protein–DNA Interactions', in *Methods in Cell Biology*, vol. 84, Elsevier, 2008, pp. 243–262.

[72] P. Schuck, 'Use of Surface Plasmon Resonance to Probe the Equilibrium and Dynamic Aspects of Interaction Between Biological Macromolecules', *Annual Review of Biophysics and Biomolecular Structure*, vol. 26, no. 1, pp. 541–566, Jun. 1997.

[73] P. Pattnaik, 'Surface Plasmon Resonance: Applications in Understanding Receptor–Ligand Interaction', *Applied Biochemistry and Biotechnology*, vol. 126, no. 2, pp. 079–092, 2005.

[74] B. Brogioni and F. Berti, 'Surface plasmon resonance for the characterization of bacterial polysaccharide antigens: a review', *MedChemComm*, vol. 5, no. 8, p. 1058, Jun. 2014.

[75] E. Stenberg, B. Persson, H. Roos, and C. Urbaniczky, 'Quantitative determination of surface concentration of protein with surface plasmon resonance using radiolabeled proteins', *Journal of Colloid and Interface Science*, vol. 143, no. 2, pp. 513–526, May 1991.

[76] P. A. Van der Merwe, 'Surface Plasmon Resonance', in *Protein-ligand Interactions: Hydrodynamics and Calorimetry, Practical Approach Series*, Oxford University Press, pp. 137–170.

[77] P. Björquistand and S. Boström, 'Determination of the Kinetic Costants of Tissue Factor/Factor VII/Factor VIIA and Antithrombin/Heparin Using Surface Plasmon Resonance', *Thrombosis Research*, vol. 85, no. 3, pp. 225–236, 1997.

[78] R. J. Green, R. A. Frazier, K. M. Shakesheff, M. C. Davies, C. J. Roberts, and S. J. B. Tendler, 'Surface plasmon resonance analysis of dynamic biological interactions with biomaterials', *Biomaterials*, vol. 21, no. 18, pp. 1823–1835, Sep. 2000.

[79] R. Rezgui *et al.*, 'Differential Interaction Kinetics of a Bipolar Structure-Specific Endonuclease with DNA Flaps Revealed by Single-Molecule Imaging', *PLoS ONE*, vol. 9, no. 11, p. e113493, Nov. 2014.

[80] B. Pathare, V. Tambe, and V. Patil, 'A Review on Various Analytical Methods Used in Determination of Dissociation Constant', vol. 6, no. 8, pp. 26–34, Aug. 2014.

[81] T. D. Pollard, 'A Guide to Simple and Informative Binding Assays', *Molecular Biology of the Cell*, vol. 21, no. 23, pp. 4061–4067, Dec. 2010.

[82] H. A. Kramers, 'Brownian motion in a field of force and the diffusion model of chemical reactions', *Physica*, vol. 7, no. 4, pp. 284–304, Apr. 1940.

[83] H.-X. Zhou, 'Rate theories for biologists', *Quarterly Reviews of Biophysics*, vol. 43, no. 02, pp. 219–293, May 2010.

[84] R. Merkel, P. Nassoy, A. Leung, K. Ritchie, and E. Evans, 'Energy landscapes of receptor–ligand bonds explored with dynamic force spectroscopy', *Nature*, vol. 397, no. 6714, pp. 50–53, Jan. 1999.

[85] G. Raab and M. Klagsbrun, 'Heparin-binding EGF-like growth factor', *Biochimica et Biophysica Acta (BBA) - Reviews on Cancer*, vol. 1333, no. 3, pp. F179–F199, Dec. 1997.

[86] S. Higashiyama, J. A. Abraham, J. Miller, J. C. Fiddes, and M. Klagsbrun, 'A heparin-binding growth factor secreted by macrophage-like cells that is related to EGF', *Science*, vol. 251, p. 5, Feb. 1991.

[87] S. A. Thompson *et al.*, 'Characterization of Sequences within Heparin-binding EGF-like Growth Factor Mediate Interaction with Heparin', *The journal of biological chemistry*, vol. 269, no. 4, pp. 2541–2549, 1994.

[88] D. T. Dao, L. Anez-Bustillos, R. M. Adam, M. Puder, and D. R. Bielenberg, 'Heparin-Binding Epidermal Growth Factor–Like Growth Factor as a Critical Mediator of Tissue Repair and Regeneration', *The American Journal of Pathology*, vol. 188, no. 11, pp. 2446–2456, Nov. 2018.

[89] S. Miyamoto *et al.*, 'Heparin-Binding EGF-Like Growth Factor Is a Promising Target for Ovarian Cancer Therapy', *Cancer Research*, vol. 64, no. 16, pp. 5720–5727, Aug. 2004.

[90] P. P. Ongusaha *et al.*, 'HB-EGF is a Potent Inducer of Tumor Growth and Angiogenesis', *Cancer Research*, vol. 64, no. 15, pp. 5283–5290, Aug. 2004.

[91] S. Yun *et al.*, 'Ligand-Independent Epidermal Growth Factor Receptor Overexpression Correlates with Poor Prognosis in Colorectal Cancer', *Cancer Research and Treatment*, vol. 50, no. 4, pp. 1351–1361, Oct. 2018.

[92] G. Bollée *et al.*, 'Epidermal growth factor receptor promotes glomerular injury and renal failure in rapidly progressive crescentic glomerulonephritis', *Nature Medicine*, vol. 17, no. 10, pp. 1242–1250, Oct. 2011.

[93] P. A. Harding, D. R. Brigstock, L. Shen, M. A. Crissman-Combs, and G. E. Besner, 'Characterization of the gene encoding murine heparin-binding epidermal growth factor-like growth factor', *Gene*, vol. 169, no. 2, pp. 291–292, Jan. 1996.

[94] Z. Gechtman, J. L. Alonso, G. Raab, D. E. Ingber, and M. Klagsbrun, 'The Shedding of Membrane-anchored Heparin-binding Epidermal-like Growth Factor Is Regulated by the Raf/Mitogen-activated Protein Kinase Cascade and by Cell Adhesion and Spreading', *Journal of Biological Chemistry*, vol. 274, no. 40, pp. 28828–28835, Oct. 1999.

[95] S. Lindsey and S. A. Langhans, 'Epidermal Growth Factor Signaling in Transformed Cells', in *International Review of Cell and Molecular Biology*, vol. 314, Elsevier, 2015, pp. 1–41.

[96] T. Mitamura, S. Higashiyama, N. Taniguchi, M. Klasbrun, and E. Mekada, 'Diphtheria Toxin Binds to the Epidermal Growth Factor (EGF)-like Domain of Human Heparin-binding EGF-like Growth Factor Diphtheria Toxin Receptor and Inhibits Specifically Its Mitogenic Activity', *The journal of biological chemistry*, vol. 270, no. 3, pp. 1015–1019, Jan. 1995.

[97] D. Gillet, B. Villiers, S. Pichard, B. Maillere, and A. Sanson, 'HB-EGF Inhibitor Derived from the R Domain of Diphtheria Toxin for the Treatment of Diseases Associated with the Activation of the HB-EGF/EGFR Pathway', US9,785,552B2.

[98] M. Flamant, G. Bollee, C. Henique, and P.-L. Tharaux, 'Epidermal growth factor: a new therapeutic target in glomerular disease', *Nephrology Dialysis Transplantation*, vol. 27, no. 4, pp. 1297–1304, Apr. 2012.

[99] D. C. Duffy, J. C. McDonald, O. J. A. Schueller, and G. M. Whitesides, 'Rapid Prototyping of Microfluidic Systems in Poly(dimethylsiloxane)', *Analytical Chemistry*, vol. 70, no. 23, pp. 4974–4984, Dec. 1998.

[100] P. D. Verweij, M. J. Haanepen, J. J. de Ridder, W. L. Driessen, and J. Reedijk, 'Synthesis, characterization and metal-uptake behaviour of pyrazole ligands immobilized on silica', *Recueil des Travaux Chimiques des Pays-Bas*, vol. 111, no. 9, pp. 371–378, Sep. 1992.

[101] A. Huignard, T. Gacoin, and J.-P. Boilot, 'Synthesis and Luminescence Properties of Colloidal YVO 4 :Eu Phosphors', *Chemistry of Materials*, vol. 12, no. 4, pp. 1090–1094, Apr. 2000.

[102] E. Beaurepaire *et al.*, 'Functionalized Fluorescent Oxide Nanoparticles: Artificial Toxins for Sodium Channel Targeting and Imaging at the Single-Molecule Level', *Nano Letters*, vol. 4, no. 11, pp. 2079–2083, Nov. 2004.

[103] D. Casanova *et al.*, 'Counting the Number of Proteins Coupled to Single Nanoparticles', *Journal of the American Chemical Society*, vol. 129, no. 42, pp. 12592–12593, Oct. 2007.

[104] D. Giaume *et al.*, 'Organic Functionalization of Luminescent Oxide Nanoparticles toward Their Application As Biological Probes', *Langmuir*, vol. 24, no. 19, pp. 11018–11026, Oct. 2008.

[105] M. U. Richly *et al.*, 'Calibrating optical tweezers with Bayesian inference', *Optics Express*, vol. 21, no. 25, p. 31578, Dec. 2013.

[106] C. I. Bouzigues, P. Tabeling, and L. Bocquet, 'Nanofluidics in the Debye Layer at Hydrophilic and Hydrophobic Surfaces', *Phys. Rev. Lett.*, vol. 101, no. 11, p. 114503, Sep. 2008.

[107] M. L. Quillin and B. W. Matthews, 'Accurate calculation of the density of proteins', *Acta Crystallographica Section D Biological Crystallography*, vol. 56, no. 7, pp. 791–794, Jul. 2000.

[108] E. Sezgin, I. Levental, S. Mayor, and C. Eggeling, 'The mystery of membrane organization: composition, regulation and roles of lipid rafts', *Nature Reviews Molecular Cell Biology*, vol. 18, no. 6, pp. 361–374, Mar. 2017.

[109] J. Lombard, 'Once upon a time the cell membranes: 175 years of cell boundary research', *Biology Direct*, vol. 9, no. 1, Dec. 2014.

[110] J. Bernardino de la Serna, G. J. Schütz, C. Eggeling, and M. Cebecauer, 'There is No Simple Model of the Plasma Membrane Organization', *Frontiers in Cell and Developmental Biology*, vol. 4, Sep. 2016.

[111] A. Honigmann and A. Pralle, 'Compartmentalization of the Cell Membrane', *Journal of Molecular Biology*, vol. 428, no. 24, pp. 4739–4748, Dec. 2016.

[112] X. Cheng and J. C. Smith, 'Biological Membrane Organization and Cellular Signaling', *Chemical Reviews*, p. acs.chemrev.8b00439, Feb. 2019.

[113] E. Gorter, 'On Biomolecular Layers of Lipoids on the Chromocytes of the Blood', *Journal of Experimental Medicine*, vol. 41, no. 4, pp. 439–443, Mar. 1925.

[114] J. F. Danielli and H. Davson, 'A contribution to the theory of permeability of thin films', *Journal of Cellular and Comparative Physiology*, vol. 5, no. 4, pp. 495–508, Feb. 1935.

[115] S. J. Singer and G. L. Nicolson, 'The fluid mosaic model of the structure of cell membrane', *Science*, vol. 175, no. 4023, pp. 720–731, Feb. 1972.

[116] J. Yu, D. A. Fischman, and T. L. Steck, 'Selective solubilization of proteins and phospholipids from red blood cell membranes by nonionic detergents', *Journal of Supramolecular Structure*, vol. 1, no. 3, pp. 233–248, 1973.

[117] K. Simons and G. Van Meer, 'Lipid sorting in epithelial cells', *Biochemistry*, vol. 27, no. 17, pp. 6197–6202, Aug. 1988.
[118] K. Simons and E. Ikonen, 'Functional rafts in cell membranes', vol. 387, p. 4, 1997.
[119] K. G. Rothberg, 'Cholesterol controls the clustering of the glycophospholipid-anchored membrane receptor for 5-methyltetrahydrofolate', *The Journal of Cell Biology*, vol. 111, no. 6, pp. 2931–2938, Dec. 1990.
[120] D. A. Brown and J. K. Rose, 'Sorting of GPI-anchored proteins to glycolipid-enriched membrane subdomains during transport to the apical cell surface..pdf', *Cell*, vol. 68, pp. 533–544, Feb. 1992.
[121] G. Van Meer, E. H. K. Sterlzer, R. W. Wijnqendts-van-Resandt, and K. Simons, 'Sorting of sphingolipids in epithelial (Madin-Darby Canine Kidney) cells', *The Journal of Cell Biology*, vol. 105, pp. 1623–1635, Oct. 1987.
[122] K. Simons and D. Toomre, 'Lipid rafts and signal transduction', *Nature Reviews Molecular Cell Biology*, vol. 1, no. 1, pp. 31–39, Oct. 2000.
[123] G. E. Palade, 'An Electron Microscope Study of the Mitochondrial Structure', *J Histochem Cytochem.*, vol. 1, no. 4, pp. 188–211, Jul. 1953.
[124] E. Yamada, 'The Fine Sructure of the Gall Bladder Epithelium of the Mouse', *The Journal of Cell Biology*, vol. 1, no. 5, pp. 445–458, Sep. 1955.
[125] M. Zuidscherwoude, C. M. de Winde, A. Cambi, and A. B. van Spriel, 'Microdomains in the membrane landscape shape antigen-presenting cell function', *Journal of Leukocyte Biology*, vol. 95, no. 2, pp. 251–263, Feb. 2014.
[126] E. Rubinstein, F. Le Naour, C. Lagaudrière-Gesbert, M. Billard, H. Conjeaud, and C. Boucheix, 'CD9, CD63, CD81, and CD82 are components of a surface tetraspan network connected to HLA-DR and VLA integrins', *Eur. J. Immunol.*, vol. 26, no. 11, pp. 2657–2665, Nov. 1996.
[127] M. E. Hemler, 'Tetraspanin functions and associated microdomains', *Nature Reviews Molecular Cell Biology*, vol. 6, no. 10, pp. 801–811, Oct. 2005.
[128] Y. Sako and A. Kusumi, 'Compartmentalized structure of the plasma membrane for receptor movements as revealed by a nanometer-level motion analysis', *The Journal of Cell Biology*, vol. 125, no. 6, pp. 1251–1264, Jun. 1994.
[129] M. Tomishige, Y. Sako, and A. Kusumi, 'Regulation Mechanism of the Lateral Diffusion of Band 3 in Erythrocyte Membranes by the Membrane Skeleton', *The Journal of Cell Biology*, vol. 142, no. 4, pp. 989–1000, Aug. 1998.
[130] K. Ritchie, R. Iino, T. Fujiwara, K. Murase, and A. Kusumi, 'The fence and picket structure of the plasma membrane of live cells as revealed by single molecule techniques (Review)', *Molecular Membrane Biology*, vol. 20, no. 1, pp. 13–18, Jan. 2003.
[131] T. Fujiwara, K. Ritchie, H. Murakoshi, K. Jacobson, and A. Kusumi, 'Phospholipids undergo hop diffusion in compartmentalized cell membrane', *The Journal of Cell Biology*, vol. 157, no. 6, pp. 1071–1082, Jun. 2002.
[132] K. Murase *et al.*, 'Ultrafine Membrane Compartments for Molecular Diffusion as Revealed by Single Molecule Techniques', *Biophysical Journal*, vol. 86, no. 6, pp. 4075–4093, Jun. 2004.
[133] K. Simons and J. L. Sampaio, 'Membrane Organization and Lipid Rafts', *Cold Spring Harbor Perspectives in Biology*, vol. 3, no. 10, pp. a004697–a004697, Oct. 2011.
[134] L. J. Pike, 'Rafts defined: a report on the Keystone symposium on lipid rafts and cell function', *Journal of Lipid Research*, vol. 47, no. 7, pp. 1597–1598, Jul. 2006.
[135] D. Lingwood and K. Simons, 'Lipid Rafts As a Membrane-Organizing Principle', *Science*, vol. 327, no. 5961, pp. 46–50, Jan. 2010.
[136] L. K. Tamm and H. M. McConnell, 'Supported phospholipid bilayers', *Biophysical Journal*, vol. 47, no. 1, pp. 105–113, Jan. 1985.

[137] S. L. Veatch and S. L. Keller, ‘Separation of Liquid Phases in Giant Vesicles of Ternary Mixtures of Phospholipids and Cholesterol’, *Biophysical Journal*, vol. 85, no. 5, pp. 3074–3083, Nov. 2003.

[138] D. A. Brown and E. London, ‘Structure and Origin of Ordered Lipid Domains in Biological Membranes’, *The Journal of Membrane Biology*, vol. 164, no. 2, pp. 103–114, Jul. 1998.

[139] J. Korlach, P. Schwille, W. W. Webb, and G. W. Feigenson, ‘Characterization of lipid bilayer phases by confocal microscopy and fluorescence correlation spectroscopy’, *Proceedings of the National Academy of Sciences*, vol. 96, no. 15, pp. 8461–8466, Jul. 1999.

[140] N. Kahya, D. Scherfeld, K. Bacia, B. Poolman, and P. Schwille, ‘Probing Lipid Mobility of Raft-exhibiting Model Membranes by Fluorescence Correlation Spectroscopy’, *Journal of Biological Chemistry*, vol. 278, no. 30, pp. 28109–28115, Jul. 2003.

[141] T. Baumgart *et al.*, ‘Large-scale fluid/fluid phase separation of proteins and lipids in giant plasma membrane vesicles’, *Proceedings of the National Academy of Sciences*, vol. 104, no. 9, pp. 3165–3170, Feb. 2007.

[142] J. Bernardino de la Serna, J. Perez-Gil, A. C. Simonsen, and L. A. Bagatolli, ‘Cholesterol Rules: Direct observation of the coexistence of two fluid phases in native pulmonary surfactant membranes at physiological temperatures’, *Journal of Biological Chemistry*, vol. 279, no. 39, pp. 40715–40722, Sep. 2004.

[143] S. A. Sanchez, M. A. Tricerri, and E. Gratton, ‘Laurdan generalized polarization fluctuations measures membrane packing micro-heterogeneity in vivo’, *Proceedings of the National Academy of Sciences*, vol. 109, no. 19, pp. 7314–7319, May 2012.

[144] D. Tyteca *et al.*, ‘Three unrelated sphingomyelin analogs spontaneously cluster into plasma membrane micrometric domains’, *Biochimica et Biophysica Acta (BBA) - Biomembranes*, vol. 1798, no. 5, pp. 909–927, May 2010.

[145] G. Grossmann, M. Opekarova, J. Malinsky, I. Weig-Meckl, and W. Tanner, ‘Membrane potential governs lateral segregation of plasma membrane proteins and lipids in yeast’, *The EMBO Journal*, vol. 26, no. 1, pp. 1–8, 2007.

[146] P. Sharma *et al.*, ‘Nanoscale Organization of Multiple GPI-Anchored Proteins in Living Cell Membranes’, *Cell*, vol. 116, no. 4, pp. 577–589, Feb. 2004.

[147] K. Malínská, J. Malínský, M. Opekarová, and W. Tanner, ‘Visualization of Protein Compartmentation within the Plasma Membrane of Living Yeast Cells’, *Molecular Biology of the Cell*, vol. 14, no. 11, pp. 4427–4436, Nov. 2003.

[148] M. Carquin *et al.*, ‘Cholesterol segregates into submicrometric domains at the living erythrocyte membrane: evidence and regulation’, *Cellular and Molecular Life Sciences*, vol. 72, no. 23, pp. 4633–4651, Dec. 2015.

[149] E. Klotzsch and G. J. Schutz, ‘A critical survey of methods to detect plasma membrane rafts’, *Philosophical Transactions of the Royal Society B: Biological Sciences*, vol. 368, no. 1611, pp. 20120033–20120033, Dec. 2012.

[150] A. K. Shishina, E. A. Kovrigina, A. R. Galiakhmetov, R. Rathore, and E. L. Kovrigin, ‘Study of Förster Resonance Energy Transfer to Lipid Domain Markers Ascertains Partitioning of Semisynthetic Lipidated N-Ras in Lipid Raft Nanodomains’, *Biochemistry*, vol. 57, no. 5, pp. 872–881, Feb. 2018.

[151] A. E. Schade and A. D. Levine, ‘Lipid Raft Heterogeneity in Human Peripheral Blood T Lymphoblasts: A Mechanism for Regulating the Initiation of TCR Signal Transduction’, *The Journal of Immunology*, vol. 168, no. 5, pp. 2233–2239, Mar. 2002.

[152] R. Parton, ‘Lipid rafts and plasma membrane microorganization: insights from Ras’, *Trends in Cell Biology*, vol. 14, no. 3, pp. 141–147, Mar. 2004.

[153] S. S. Vogel, C. Thaler, and S. V. Koushik, ‘Fanciful FRET’, *Sci. STKE*, vol. 2006, no. 331, p. re2, Apr. 2006.

[154] H. Shroff, C. G. Galbraith, J. A. Galbraith, and E. Betzig, 'Live-cell photoactivated localization microscopy of nanoscale adhesion dynamics', *Nat Methods*, vol. 5, no. 5, pp. 417–423, May 2008.

[155] H. Mizuno *et al.*, 'Fluorescent probes for superresolution imaging of lipid domains on the plasma membrane', *Chem. Sci.*, vol. 2, no. 8, p. 1548, 2011.

[156] P. Sengupta, T. Jovanovic-Talisman, D. Skoko, M. Renz, S. L. Veatch, and J. Lippincott-Schwartz, 'Probing protein heterogeneity in the plasma membrane using PALM and pair correlation analysis', *Nat Methods*, vol. 8, no. 11, pp. 969–975, Nov. 2011.

[157] D. Jin, P. Xi, B. Wang, L. Zhang, J. Enderlein, and A. M. van Oijen, 'Nanoparticles for super-resolution microscopy and single-molecule tracking', *Nat Methods*, vol. 15, no. 6, pp. 415–423, Jun. 2018.

[158] A. Kusumi *et al.*, 'Paradigm Shift of the Plasma Membrane Concept from the Two-Dimensional Continuum Fluid to the Partitioned Fluid: High-Speed Single-Molecule Tracking of Membrane Molecules', *Annu. Rev. Biophys. Biomol. Struct.*, vol. 34, no. 1, pp. 351–378, Jun. 2005.

[159] K. Suzuki, K. Ritchie, E. Kajikawa, T. Fujiwara, and A. Kusumi, 'Rapid Hop Diffusion of a G-Protein-Coupled Receptor in the Plasma Membrane as Revealed by Single-Molecule Techniques', *Biophysical Journal*, vol. 88, no. 5, pp. 3659–3680, May 2005.

[160] M. J. Saxton, 'The membrane skeleton of erythrocytes. A percolation model', *Biophysical Journal*, vol. 57, no. 6, pp. 1167–1177, Jun. 1990.

[161] T. K. Fujiwara *et al.*, 'Confined diffusion of transmembrane proteins and lipids induced by the same actin meshwork lining the plasma membrane', *Molecular Biology of the Cell*, vol. 27, no. 7, pp. 1101–1119, Apr. 2016.

[162] S. A. Freeman *et al.*, 'Transmembrane Pickets Connect Cyto- and Pericellular Skeletons Forming Barriers to Receptor Engagement', *Cell*, vol. 172, no. 1–2, pp. 305-317.e10, Jan. 2018.

[163] S. M. Mylvaganam, S. Grinstein, and S. A. Freeman, 'Picket-fences in the plasma membrane: functions in immune cells and phagocytosis', *Semin Immunopathol*, vol. 40, no. 6, pp. 605–615, Nov. 2018.

[164] A. Kusumi *et al.*, 'Membrane mechanisms for signal transduction: The coupling of the meso-scale raft domains to membrane-skeleton-induced compartments and dynamic protein complexes', *Seminars in Cell & Developmental Biology*, vol. 23, no. 2, pp. 126–144, Apr. 2012.

[165] L. J. Pike, X. Han, and R. W. Gross, 'EGF Receptors Are Localized to Lipid Rafts that Contain a Balance of Inner and Outer Leaflet Lipids: A Shotgun Lipidomics Study', p. 27, 2005.

[166] M. B. Omary and I. S. Trowbridge, 'Covalent Binding of Fatty Acid to the transferrin receptor in culture human cells.pdf', *The journal of biological chemistry*, vol. 256, no. 10, pp. 4715–4718, May 1981.

[167] M. U. Muckenthaler, S. Rivella, M. W. Hentze, and B. Galy, 'A Red Carpet for Iron Metabolism', *Cell*, vol. 168, no. 3, pp. 344–361, Jan. 2017.

[168] E. Gammella, P. Buratti, G. Cairo, and S. Recalcati, 'The Transferrin Receptor : The Cellular Iron Gate', *Metallomics*, 2017.

[169] S. Jin, P. M. Haggie, and A. S. Verkman, 'Single-Particle Tracking of Membrane Protein Diffusion in a Potential: Simulation, Detection, and Application to Confined Diffusion of CFTR Cl− Channels', *Biophysical Journal*, vol. 93, no. 3, pp. 1079–1088, Aug. 2007.

[170] S. J. Plowman, C. Muncke, R. G. Parton, and J. F. Hancock, 'H-ras, K-ras, and inner plasma membrane raft proteins operate in nanoclusters with differential dependence on the actin cytoskeleton', *Proceedings of the National Academy of Sciences*, vol. 102, no. 43, pp. 15500–15505, Oct. 2005.

[171] A. Remorino *et al.*, 'Gradients of Rac1 Nanoclusters Support Spatial Patterns of Rac1 Signaling', *Cell Reports*, vol. 21, no. 7, pp. 1922–1935, Nov. 2017.

[172] P.-F. Lenne *et al.*, 'Dynamic molecular confinement in the plasma membrane by microdomains and the cytoskeleton meshwork', *The EMBO Journal*, vol. 25, no. 14, pp. 3245–3256, Jul. 2006.
[173] I. Levental and S. L. Veatch, 'The Continuing Mystery of Lipid Rafts', *Journal of Molecular Biology*, vol. 428, no. 24, pp. 4749–4764, Dec. 2016.
[174] I. Levental and S. L. Veatch, 'The Continuing Mystery of Lipid Rafts', *Journal of Molecular Biology*, vol. 428, no. 24, pp. 4749–4764, Dec. 2016.
[175] A. Honigmann and A. Pralle, 'Compartmentalization of the Cell Membrane', *Journal of Molecular Biology*, vol. 428, no. 24, pp. 4739–4748, Dec. 2016.
[176] J. Lemière, F. Valentino, C. Campillo, and C. Sykes, 'How cellular membrane properties are affected by the actin cytoskeleton', *Biochimie*, vol. 130, pp. 33–40, Nov. 2016.
[177] S. Wang, S. Cang, and D. Liu, 'Third-generation inhibitors targeting EGFR T790M mutation in advanced non-small cell lung cancer', *J Hematol Oncol*, vol. 9, no. 1, p. 34, Dec. 2016.
[178] P. Seshacharyulu, M. P. Ponnusamy, D. Haridas, M. Jain, A. K. Ganti, and S. K. Batra, 'Targeting the EGFR signaling pathway in cancer therapy', *Expert Opinion on Therapeutic Targets*, vol. 16, no. 1, pp. 15–31, Jan. 2012.
[179] A. Arkhipov *et al.*, 'Architecture and Membrane Interactions of the EGF Receptor', *Cell*, vol. 152, no. 3, pp. 557–569, Jan. 2013.
[180] M. A. Lemmon and J. Schlessinger, 'Cell Signaling by Receptor Tyrosine Kinases', *Cell*, vol. 141, no. 7, pp. 1117–1134, Jun. 2010.
[181] N. Morone *et al.*, 'Three-dimensional reconstruction of the membrane skeleton at the plasma membrane interface by electron tomography', *J Cell Biol*, vol. 174, no. 6, pp. 851–862, Sep. 2006.
[182] E. Beaurepaire *et al.*, 'Functionalized Fluorescent Oxide Nanoparticles: Artificial Toxins for Sodium Channel Targeting and Imaging at the Single-Molecule Level', *Nano Letters*, vol. 4, no. 11, pp. 2079–2083, Nov. 2004.
[183] Y. Sako, 'Barriers for lateral diffusion of transferrin receptor in the plasma membrane as characterized by receptor dragging by laser tweezers: fence versus tether', *The Journal of Cell Biology*, vol. 129, no. 6, pp. 1559–1574, Jun. 1995.
[184] L. Petit, M. Gibert, D. Gillet, C. Laurent-Winter, P. Boquet, and M. R. Popoff, 'Clostridium perfringens epsilon-toxin acts on MDCK cells by forming a large membrane complex.', *J. Bacteriol.*, vol. 179, no. 20, pp. 6480–6487, Oct. 1997.
[185] G. G. Stokes, *On the Effect of the Internal Friction of Fluids on the Motion of Pendulums*, 9 vols. Cambridge: Cambridge University Press, 1850.
[186] P. Chugh *et al.*, 'Actin cortex architecture regulates cell surface tension', *Nature Cell Biology*, vol. 19, no. 6, pp. 689–697, May 2017.
[187] E. D. Goley and M. D. Welch, 'The ARP2/3 complex: an actin nucleator comes of age', *Nature Reviews Molecular Cell Biology*, vol. 7, no. 10, pp. 713–726, Oct. 2006.
[188] A. Bretscher, K. Edwards, and R. G. Fehon, 'ERM proteins and merlin: integrators at the cell cortex', *Nature Reviews Molecular Cell Biology*, vol. 3, no. 8, pp. 586–599, Aug. 2002.
[189] F. C. Morales, Y. Takahashi, E. L. Kreimann, and M.-M. Georgescu, 'Ezrin-radixin-moesin (ERM)-binding phosphoprotein 50 organizes ERM proteins at the apical membrane of polarized epithelia', *Proceedings of the National Academy of Sciences*, vol. 101, no. 51, pp. 17705–17710, Dec. 2004.
[190] B. J. Nolen *et al.*, 'Characterization of two classes of small molecule inhibitors of Arp2/3 complex', *Nature*, vol. 460, no. 7258, pp. 1031–1034, Aug. 2009.
[191] A. W. Coleman, M. J. Maguire, and J. R. Coleman, 'Mithramycin- and 4'-6-diamidino-2-phenylindole (DAPI)-DNA staining for fluorescence microspectrophotometric measurement of DNA in nuclei, plastids, and virus particles.', *Journal of Histochemistry & Cytochemistry*, vol. 29, no. 8, pp. 959–968, Aug. 1981.

[192] B. Chazotte, 'Labeling Cytoskeletal F-Actin with Rhodamine Phalloidin or Fluorescein Phalloidin for Imaging', *Cold Spring Harbor Protocols*, vol. 2010, no. 5, p. pdb.prot4947-pdb.prot4947, May 2010.
[193] A. Aggarwal *et al.*, 'Mobilization of HIV Spread by Diaphanous 2 Dependent Filopodia in Infected Dendritic Cells', *PLoS Pathogens*, vol. 8, no. 6, p. e1002762, Jun. 2012.
[194] D. B. Short *et al.*, 'An Apical PDZ Protein Anchors the Cystic Fibrosis Transmembrane Conductance Regulator to the Cytoskeleton', *J. Biol. Chem.*, vol. 273, no. 31, pp. 19797–19801, Jul. 1998.
[195] G. Bulut *et al.*, 'Small molecule inhibitors of ezrin inhibit the invasive phenotype of osteosarcoma cells', *Oncogene*, vol. 31, no. 3, pp. 269–281, Jan. 2012.
[196] B. Fiévet, D. Louvard, and M. Arpin, 'ERM proteins in epithelial cell organization and functions', *Biochimica et Biophysica Acta (BBA) - Molecular Cell Research*, vol. 1773, no. 5, pp. 653–660, May 2007.
[197] S. Byun *et al.*, 'Characterizing deformability and surface friction of cancer cells', *Proceedings of the National Academy of Sciences*, vol. 110, no. 19, pp. 7580–7585, May 2013.

Titre : Etude quantitative de la nano-organisation membranaire par imagerie de nanoparticules individuelles

Mots clés : Suivi de molécules uniques (SMT), force hydrodynamique, Nanodomaine membranaire, Récepteurs membranaires, taux de dissociation ultra-faible

Résumé:

La nano-organisation de la membrane cellulaire est essentielle à la régulation de certaines fonctions cellulaires, notamment par le biais de processus de signalisation impliquant des interactions membranaires, des interactions de biomolécules dans la membrane cellulaire. Les propriétés biophysiques et la dynamique des nanodomaines membranaires dans les cellules vivantes peuvent donc fournir des informations cruciales pour comprendre le rôle de l'organisation membranaire dans de nombreuses activités cellulaires.

Dans cette thèse, nous nous sommes intéressés à l'organisation de la membrane cellulaire et aux interactions entre récepteur, nanodomaines lipidiques et cytosquelette d'actine par l'imagerie de récepteurs individuels et par l'application de forces hydrodynamiques contrôlées Grâce aux propriétés de luminescentce des nanoparticules $Y_{0.6}Eu_{0.4}VO_{0.4}$, les récepteurs EGF, CPεT et les récepteurs de la transferrine ont ainsiété suivis dans l dans la membrane de cellules vivantes pour de longues durées, avec, avec ou sans application de force par un système microfluidique. Nous avons alors appliqué des techniquesd'inférence bayésienne, d'arbre de décision et d de clustering de données extraire des informations quantitatives sur les paramètres caractéristiques du mouvement des récepteurs, notamment la forme de leur confinement dans des microdomaines.

Nous avons ainsi caractérisé quantitativement les mouvements des récepteurs de l'EGF (EGFR) et appliqué des techniquesd'inférence bayésienne, d'arbre de décision et de clustering de données extraire des informations quantitatives sur les paramètres caractéristiques du mouvement des récepteurs, notamment la forme de leur confinement dans des microdomaines.: ceux-ci suivent un mouvement brownien confiné à l'intérieur d'un potentiel de confinement quadratique, similaire à celui observé pour les récepteurs de toxine CPεT et CPαT. En revanche, les récepteurs de la transferrine présentent un type de potentiel de confinement distinct, mieux décrit par un polynôme du 4ème ordre. Nous avons ensuite étudié la base moléculaire de ce confinement. L'application d'une enzyme de déstabilisation des radeaux lipidique ou d'une dépolymérisation d'actine de filament sur le confinement des récepteurs de l'EGF a induit une nette tendance à une plus grande diffusivité et à un confinement plus faible. Ceci indique que l'EGFR est à la fois confiné dans des

microdomaines lipidiques et par son interaction directe avec les filaments d'actine : le potentiel de confinement peut donc être modélisé par un système à deux ressorts en parallèle, sa rigidité effective résultant à la fois des interactions des récepteurs avec les lipides et les protéines de l'environnement du radeau et des t. interactions avec la F-actine. Le confinement des récepteurs CPεTR et de CSαTR peut être décrit par contraste par un modèle à ressort unique qui reflète l'interaction entre les récepteurs et les constituants lipidiques / protéiques du radeau.

Nous avons alors montré que la taille du domaine observé expérimentalement résulte uniquement de la rigidité du potentiel de confinement auquel le récepteur est soumis. La taille de domaine "apparente" est alors déterminée par la la probabilité d'exploration brownienne du potentiel par le récepteur, à l'équilibre thermodynamique. .

A l'aide d'un dispositif microfluidique, nous avons appliqué une force amplifiée par les nanoparticules sur des récepteurs individuels de la membrane cellulaire pour sonder les interactions entre les récepteurs, les microdomaines lipidiques et le cytosquelette. L'application d'une force sur des EGFR et CPεTR individuels entraîne la déformation élastique d'un constituant de la cellule. En revanche, les récepteurs de la transferrine sont d'abord déplacés par la force, mais ne reviennent pas à leur position initiale une fois que la flux a été arrêtée. La dépolymérisation du cytosquelette d'actine par la latrunculine B et la réduction de la rigidité du réseau d'actine par l'inhibiteur Arp2/3, CK548, induisent une augmentation des déplacements observés de EGFR et de CPεTR : et donc une diminution de la rigidité du constituant cellulaire déformé. Ceci indique que la déformation élastique induite parla force générée par l'écoulement est celle du réseau d'actine. L'ensemble de ces résultats nous ont mené a identifié différents types d'organisation, spécifiques de chaque récepteur. Le confinement de CPεTR est déterminé par l'interaction entre les récepteurs et les constituants lipidiques / protéiques du radeau, celui-ci interagissant avec le réseau d'actine; le potentiel de confinement de l'EGFR résulte de l'interaction avec les lipides et les protéines de l'environnement du radeau et de l'interaction directe avec la F-actine; les récepteurs de la transferrine diffusent librement dans la membrane, leurs mouvement étant seulement limités stériquement par des barrières d'actine, selon le modèle dit « picket-and-fence ».

Nous avons alors étendu l'utilisation de nanoparticules comme amplificateur de force hydrodynamique pour l'étude *in vitro* de la dissociation de biomolécules entre des récepteurs membranaires et leurs ligands pharmaceutiques de haute affinité, telles que HB-EGF et DTR. L'affinité de ces complexes est une donnée essentielle pour les caractériser en vue d'application thérapeutiques, mais reste difficile à mesurer, à cause de très longs temps de

dissociation τ_{off}. En marquant le ligand avec des nanoparticules luminescentes d'un rayon hydrodynamique typique de 25 nm, nous avons appliqué sur les complexes HB-EGF-DTR-NP des forces allant jusqu'à 40 pN, ce permet de réduire significativement τ_{off}. Nous avons ensuite utilisé l'imagerie de nanoparticules individuelles pour obtenir le temps caractéristique expérimental τ_{off} (F) pour différentes valeurs de force, simplement en mesurant le nombre de nanoparticules N attachées restantes en fonction du temps. L'utilisation de la loi de Kramers permet alors l'extrapoleation pour obtenir le taux de dissocaition k_{off} (0).

Ce travail présente donc à la fois un aperçu quantitatif du récepteur membranaire, des mécanismes d'organisation à l'échelle nanométrique, et établit un cadre méthodologique avec lequel différents types de propriétés membranaires peuvent être étudiés.

université PARIS-SACLAY

ÉCOLE DOCTORALE
INTERFACES
Approches Interdisciplinaires : Fondements, Applications et Innovation

Titre : Etude quantitative de la nano-organisation membranaire par imagerie de nanoparticules individuelles

Mots clés : Suivi de molécules uniques (SMT), force hydrodynamique, Nanodomaine membranaire, Récepteurs membranaires, taux de dissociation ultra-faible

Résumé : La nano-organisation de la membrane cellulaire est essentielle à la régulation de certaines fonctions cellulaires.
Dans cette thèse, les récepteurs EGF, CPεT et de la transferrine ont été marqués avec des nanoparticules luminescentes et ont été suivis à la fois dans leur environnement local dans la membrane cellulaire vivantes pour de longues durées et sous un flux hydrodynamique. Nous avons alors appliqué des techniquesd'inférence bayésienne, d'arbre de décision et de clustering de données extraire des informations quantitatives sur les paramètres caractéristiques du mouvement des récepteurs, notamment la forme de leur confinement dans des microdomaines. L'application d'une force hydrodynamique sur les nanoparticules nous a alors permis de sonder les interactions auxquelles ces récepteurs sont soumis. Nous avons appliqué cette approche *in vitro* pour favoriser et mesurer la dissociation *in vitro* de paires récepteur / ligand à haute affinité entre des récepteurs membranaires et leurs ligands pharmaceutiques, telles que HB-EGF et DTR et l'avons ensuite appliqué à l'étude d'interactions à la membrane cellulaire.
Nous avons ainsi mis en évidence trois modes différents d'organisation de la membrane et de confinement des récepteurs: le confinement de CPεTR est déterminé par l'interaction entre les récepteurs et les constituants lipidiques / protéiques des microdomaines, le potentiel de confinement de l'EGFR résulte de l'interaction avec les lipides et les protéines de l'environnement du radeau et de l'interaction avec la F-actine; les récepteurs de la transferrine diffusent librement dans la membrane, uniquement limités stériquement par des barrières d'actine, selon le modèle 'picket-and-fence'. Nous avons de plus montré que les nanodomaines de type radeau sont rattachés au cytoskelette d'actine.
Ce travail présente donc à la fois un aperçu quantitatif du récepteur membranaire, des mécanismes d'organisation à l'échelle nanométrique, et établit un cadre méthodologique avec lequel différents types de propriétés membranaires peuvent être étudiés.

Title : Quantitative Study of Membrane Nano-organization by Single Nanoparticle Imaging

Keywords : Single Molecule Tracking (SMT), Cell Membrane Nanodomains, Membrane Receptors, Hydrodynamic Force Application, Ultra-low Dissociation Rate

Abstract: In this thesis, EGF, CPεT and transferrin receptors were labeled with luminescent nanoparticles, $Y_{0.6}Eu_{0.4}VO_{0.4}$, and were tracked both in their local environment in the cell membrane and under a hydrodynamic flow. Bayesian inference, Bayesian decision tree, and data clustering techniques can then be applied to obtain quantitative information on the receptor motion parameters. Furthermore, we introduced hydrodynamic force application *in vitro* to study biomolecule dissociation between membrane receptors and their pharmaceutical ligands in high affinity receptor-ligand pairs, such as HB-EGF and DTR.
Finally, three different modes of membrane organization and receptor confinement were revealed: the confinement of CPεTR is determined by the interaction between the receptors and the lipid/protein constituents of the raft; the confining potential of EGFR results from the interaction with lipids and proteins of the raft environment and from the interaction with F-actin; transferrin receptors diffuse freely in the membrane, only sterically limited by actin barriers, according to the "picket-and-fence" model. We moreover showed that all raft nanodomains are attached to the actin cytoskeleton.